Gaute Gruben

Ductile Fracture in Dual-Phase Steel

Theoretical, Experimental and Numerical Study

Thesis for the degree of Philosophiae Doctor

Trondheim, September 2012

Norwegian University of Science and Technology
Faculty of Engineering Science and Technology
Department of Structural Engineering

NTNU – Trondheim
Norwegian University of
Science and Technology

NTNU
Norwegian University of Science and Technology

Thesis for the degree of Philosophiae Doctor

Faculty of Engineering Science and Technology
Department of Structural Engineering

ISBN 978-82-471-3822-9 (printed ver.)
ISBN 978-82-471-3823-6 (electronic ver.)
ISSN 1503-8181

Doctoral theses at NTNU, 2012:257

Printed by NTNU-trykk

Preface

This thesis is submitted in fulfilment of the degree *philosophiae doctor* at the Norwegian University of Science and Technology. The work has been carried out at the Department of Structural Engineering under the supervision of Professor Odd Sture Hopperstad and Professor Tore Børvik. The thesis consists of four articles accepted or submitted to international scientific journals. The articles are referred to as parts, as they represent different parts of the thesis. The content of the parts is bound together by a synopsis. The first author has been responsible for the experimental and numerical work in the different parts as well as processing the data and writing the manuscripts. Exceptions from this are the mechanical formability tests in Part II, which were carried out under main supervision of Mr Dmitry Vysochinskiy, and the optical measurements in Part I and Part II, which, respectively, were conducted by Dr Egil Fagerholt and Dr Tèrence Coudert.

Gaute Gruben

Trondheim, 3 July 2012

Abstract

The thesis is focused on quasi-static ductile fracture in the low range of stress triaxiality of the dual-phase steel Docol 600DL. The study includes mechanical testing, theoretical aspects of ductile fracture and numerical simulations. Ductile fracture in the low range of stress triaxiality is an interesting topic since experimental data from various studies suggests that the ductility of the material is not only governed by the hydrostatic stress-state, but is also influenced by the deviatoric stress-state.

The thesis consists of four journal articles bound together by a synopsis, where the introduction gives the motivation for the work and a state-of-the-art of the topics examined in this study. After the introduction, the objectives for the study are given followed by a summary of the work, conclusions and suggestions for further work. Finally the four articles are given. The articles are referred to as parts as they give detailed information of the different parts of the study.

In Part I and Part II the experimental side of the study is described. These parts give detailed information regarding the material, test set-ups, specimen geometries and optical measurement procedures. The results from the experiments in form of the minor versus major principal strain as well as the stress triaxiality, the Lode parameter, and the equivalent strain at fracture are presented and used to describe the material's fracture characteristics. Macroscopically the material displayed typical ductile behaviour with large strains before fracture. This was confirmed by scanning electron microscopy of selected specimens since all showed ductile dimples. Further, the material displayed a significant drop in ductility when exposed to plane-strain loading; an observation that suggests that the material's fracture properties are Lode dependent.

In Part III several uncoupled criteria for ductile fracture which explicitly take into account the effect of the Lode dependence were assessed. One of the criteria, the modified Mohr-Coulomb criterion, was taken from literature, while two of the criteria, the extended Cockcroft-Latham criterion and the extended Rice-Tracey criterion are augmented versions of existing criteria. The data given in Part I and II were used in evaluating the various criteria and it was found that the proposed extended Cockcroft-Latham criterion managed to give accurate predictions on the equivalent strain at

fracture, while a somewhat larger spread was observed for the modified Mohr-Coulomb criterion and the extended Rice-Tracey criterion.

Part IV focuses on numerical modelling of ductile crack propagation. Here the experimental tests from Part I were used in assessing the extended Cockcroft-Latham and modified Mohr-Coulomb criteria on crack propagation. Additionally the effects of using a high-exponent yield surface and material softening were investigated. It was found that the different fracture criteria as well as a change of yield function had little effect on the crack propagation. By including material softening through damage coupling, slant shear fracture as observed in some of the experiments was captured, but this did not alter the global response in form of the force-displacement curves.

Acknowledgements

My supervisors during the PhD project have been Professor Odd Sture Hopperstad and Professor Tore Børvik at the Department of Structural Engineering, Norwegian University of Science and Technology. I am very grateful for their encouragement, guidance and support throughout this work.

The involvement of Mr Trond Auestad in conducting the mechanical tests is highly appreciated. I would also like to thank Dr Ida Westermann for providing the fractographs. The valuable support from Dr Torodd Berstad in the numerical part of the work is highly acknowledged.

I also wish to thank my colleagues and friends at the Department of Structural Engineering, and especially at the Structural Impact Laboratory, for providing a good and stimulating work environment.

The work has been financially supported by the Structural Impact Laboratory, Centre for Research-based Innovation, at the Department of Structural Engineering, Norwegian University of Science and Technology.

Finally I would like to express my gratitude to my family and in particular my supportive girlfriend Ida.

Table of Contents

Journal articles:

Part I	Gruben G, Fagerholt E, Hopperstad OS and Børvik T *Fracture characteristics of a cold-rolled dual-phase steel* European Journal of Mechanics – A/Solids, 2011(30), p.204-218
Part II	Gruben G, Vysochinskiy D, Coudert T, Reyes A and Lademo O-G *Determination of ductile fracture parameters of a dual-phase steel by optical measurements* Submitted for possible journal publication, 2012
Part III	Gruben G, Hopperstad OS and Børvik T *Evaluation of uncoupled ductile fracture criteria for the dual-phase steel Docol 600DL* International Journal of Mechanical Sciences, 2012(62), p.133-146
Part IV	Gruben G, Hopperstad OS and Børvik T *Simulation of ductile crack propagation in dual-phase steel* Submitted for possible journal publication, 2012

Synopsis

1 Introduction

1.1 Background and motivation

The need for accurate numerical models is present in e.g. offshore, metal forming and automotive industry. The constant development of computational power makes it possible to run increasingly more sophisticated numerical models within a reasonable computational time. Fracture has usually not been included in full scale numerical models of e.g. car crash, due to computational costs and coarse spatial discretization. Driven by the economical needs of industry and the increase of computational power, robust and sufficiently accurate criteria for fracture are needed as well as robust numerical techniques for simulation of fracture propagation. A profound understanding of ductile fractural behaviour, physically, mechanically and numerically, is needed to be able to make good predictions of fracture propagation.

Weight reduction is an important course in order to reduce CO_2 emissions in cars. It is estimated that by reducing the weight of a car by 1 kg, the CO_2 emissions are lowered by 20 kg after 170 000 km driving [1]. By using advanced high-strength steels (AHSS), it is possible to make structural and energy-absorbing parts with thinner walls, thus reducing the total weight of the car. Another important issue is car safety. In 1997 the European New Car Assessment Program (Euro NCAP) was launched, forcing car producers to increase their attention on car safety [2]. By use of AHSS, the deformation of the cars during a crash has been decreased significantly, thus providing better protection for the passengers [3]. Fig. 1 illustrates typical automotive applications of AHSS, including bumper reinforcements, crash boxes and door impact beams [4]. The material used in this study, Docol 600DL, is an example of an AHSS that may be used in chassis components in cars. The material, which is delivered by Swedish Steel AB, is a dual-phase steel consisting of ferrite and martensite, where the ferrite gives good formability features and the martensite produces high strength [5]. The material is delivered as sheets, and can be ordered with thickness dimensions in the range from 0.5 mm to 2.1 mm. The material is meant for cold forming, and the producer reports that the steel has good formability features in bending, rollforming and pressing. The weldability of the material is very good due to its low contents of alloying elements in relation to its high strength.

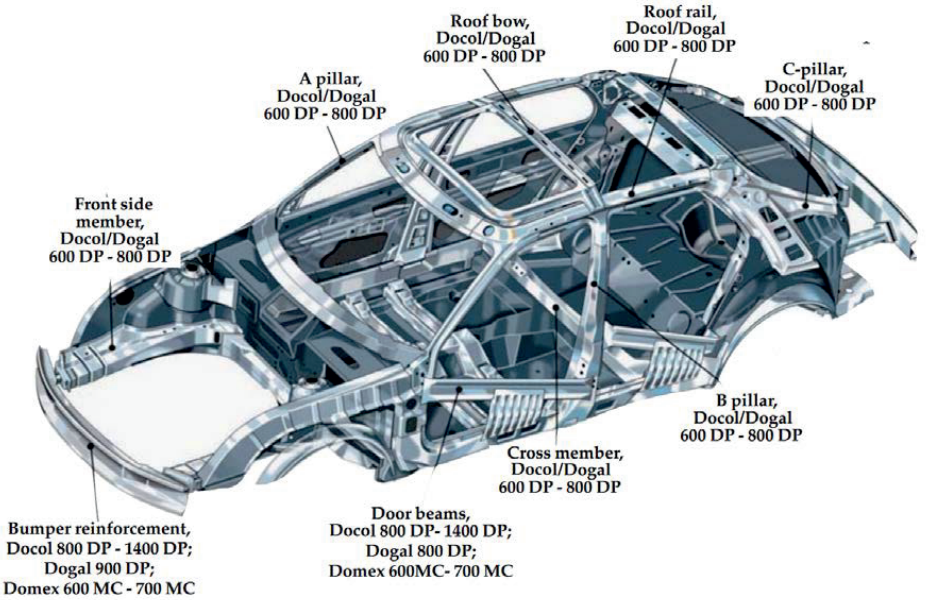

Fig. 1 Body-in-white showing examples of energy absorbing parts where different types of AHSS may be utilized [4].

Since the energy absorbing parts in cars usually are made of thin walled structures, the parts are in a near plane-stress condition during deformation, i.e. the shear and normal stresses in the thickness direction are small compared to the in-plane stresses. The plane-stress condition restricts the stress triaxiality, σ^*, in the material to the low and negative range, i.e. $-\frac{2}{3} \leq \sigma^* \leq \frac{2}{3}$. The stress triaxiality parameter gives information about the hydrostatic stress state of the material and is defined as the ratio of the hydrostatic stress, σ_h, and the von Mises equivalent stress, $\bar{\sigma}_{VM}$, viz.

$$\sigma^* = \frac{\sigma_h}{\bar{\sigma}_{VM}} \qquad (1)$$

The hydrostatic (or mean) stress, σ_h, and the equivalent von Mises stress, $\bar{\sigma}_{VM}$, are in turn given by

$$\sigma_h = \tfrac{1}{3}(\sigma_I + \sigma_{II} + \sigma_{III}) \tag{2}$$

$$\bar{\sigma} = \sqrt{\tfrac{1}{2}\left[(\sigma_I - \sigma_{II})^2 + (\sigma_{II} - \sigma_{III})^2 + (\sigma_{III} - \sigma_I)^2\right]} \tag{3}$$

In Equations (2) and (3), σ_i, $i = I, II, III$, are the principal stresses ordered so that $\sigma_I \geq \sigma_{II} \geq \sigma_{III}$. Ductile fracture is governed by nucleation, growth and coalescence of microvoids during plastic deformation [6-7]. The microvoids as well as the accumulation of strains in the neighbourhood of defects in the material or the breaking of bonds can be summed up in a damage variable following continuum damage mechanics [8-9]. The damage of the material is hard to determine experimentally, but several approaches can be utilized e.g. by measuring the change in Young's modulus [8], measuring the void volume fraction through scanning electron microscopy [10] or by measuring the change in volume of the material through optical measurements [11]. For negative values of stress triaxiality $(\sigma^* < 0)$ the growth of voids is restrained due to the hydrostatic overpressure, and so the damage that accumulates in the material is through breaking of bonds i.e. void nucleation. On the other hand, in the high stress triaxiality range $(\sigma^* > 1)$ increased stress triaxiality gives decreased ductility of the material due to increased rate in the growth of microvoids, which in this case is the governing damage mechanism. Macroscopically the ductility of a material can be measured as the equivalent plastic strain at fracture or fracture strain, defined as

$$\bar{\varepsilon}_f = \int_0^{t_f} \sqrt{\frac{2}{3}\mathbf{D}^p : \mathbf{D}^p}\, dt, \tag{4}$$

where $\mathbf{D}^p$ is the plastic part of the rate-of-deformation tensor and t_f is the time at fracture. Clausing [12] found that plane-strain specimens displayed a significantly lower ductility than uniaxial tension specimens for seven different types of steel. More recent studies [13-16] carried out on ductile materials with axisymmetric as well as thin-walled specimens in the low range of stress triaxiality $(0 < \sigma^* < 1)$ also indicate that the ductility does not decrease monotonically with increased stress triaxiality. Although voids do not grow in pure shear, it has been argued that the effect of void deformation and reorientation in shear contribute to the softening of the material [17-19]. Thus, the deviatoric stress state should also be taken into account when modelling ductile fracture in the low range of stress triaxiality (which is the case for thin-walled structures as noted above). The deviatoric stress state of the material can be expressed by several parameters, e.g. normalized third deviatoric stress invariant [20], the Lode angle [17, 21] or the normalized Lode angle [22-23]. In this study, the Lode parameter, μ, [24] which is related to the third deviatoric stress invariant is chosen. The Lode parameter has the range $-1 \leq \mu \leq 1$, and is defined as

$$\mu = \frac{2\sigma_{II} - \sigma_I - \sigma_{III}}{\sigma_I - \sigma_{III}} \tag{5}$$

In plane stress there is a one-to-one relation between the stress triaxiality and the Lode parameter, viz.

$$\begin{aligned}
\sigma_I &= 0 \quad \Rightarrow \quad -\frac{2}{3} \leq \sigma^* = \frac{\mu - 3}{3\sqrt{3+\mu^2}} \leq -\frac{1}{3} \\
\sigma_{II} &= 0 \quad \Rightarrow \quad -\frac{1}{3} \leq \sigma^* = \frac{-2\mu}{3\sqrt{3+\mu^2}} \leq +\frac{1}{3} \\
\sigma_{III} &= 0 \quad \Rightarrow \quad +\frac{1}{3} \leq \sigma^* = \frac{\mu + 3}{3\sqrt{3+\mu^2}} \leq +\frac{2}{3}
\end{aligned} \tag{6}$$

Fig. 2 displays the $\sigma^* - \mu$ locus under plane stress as well as the position of the plane-stress states, pure shear, uniaxial tension/compression, plane-strain tension/compression and biaxial tension/compression. Additionally, Fig. 2 displays the loci representing the special stress-states [14]

Generalized shear $\quad 2\sigma_{II} = \sigma_I + \sigma_{III} \Leftrightarrow \mu = 0 \quad$ (7)

Generalized tension $\quad \sigma_I \geq \sigma_{II} = \sigma_{III} \Leftrightarrow \mu = -1 \quad$ (8)

Generalized compression $\quad \sigma_I = \sigma_{II} \geq \sigma_{III} \Leftrightarrow \mu = +1 \quad$ (9)

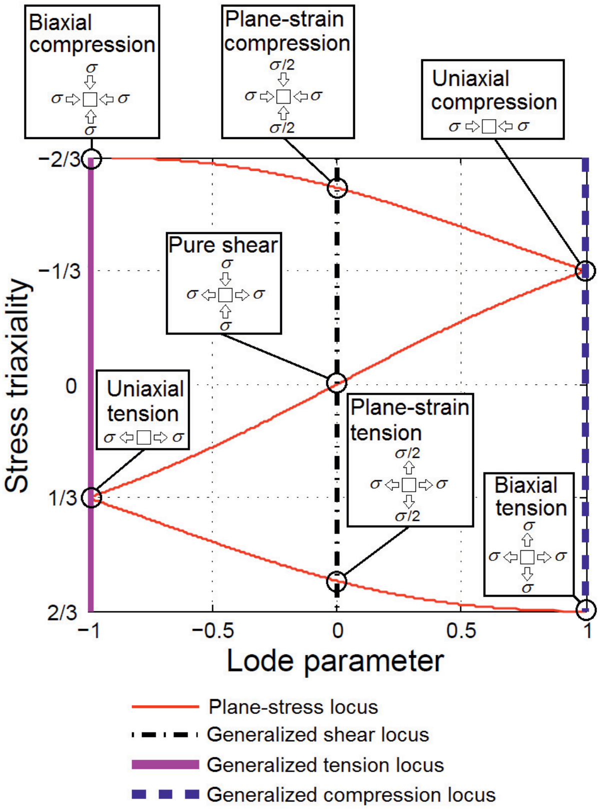

Fig. 2 Relation between stress triaxiality and Lode parameter in plane stress, generalized shear, generalized tension and generalized compression. Additionally, the positions of specific stress-states are marked.

1.2 *Previous work*

Several criteria have been proposed in the literature over the years to describe ductile fracture. Most of these criteria can be expressed as a damage variable that accumulates with plastic straining. These accumulative fracture criteria can be divided into two main groups; criteria using a coupled approach and criteria using an uncoupled approach. For the criteria with a coupled approach, influence of damage is included in the constitutive equations. This can be modelled by porous plasticity, e.g. Shima [25], Gurson [26] and Rousselier [27], or by continuum damage mechanics, e.g. Lemaitre [8] and Lemaitre and Chaboche [9]. In the criteria with the uncoupled approach, the yield criterion, plastic flow and strain hardening are unaffected by the damage. Some of these criteria are empirical e.g. Freudenthal [28], Cockcroft-Latham [29], Wilkins [30], Johnson-Cook [31] and Xue-Wierzbicki [20], while the Rice-Tracey [7] criterion, on the other hand, is based on porous plasticity. Although these criteria initially were presented as uncoupled with the constitutive equations, they can be coupled by following e.g. [32-34]. A different method to predict material failure, which is much used in metal forming industry, is the Keeler-Goodwin approach [35-36]. In this method, the principal strains at plastic instability are plotted in a forming limit diagram. This approach relies on a proportional loading assumption which is often not the case for crashworthiness problems. Stoughton [37] argued how a stress-based forming limit diagram is less affected by non-proportional loading paths, and can so be used for more complex load situations. The stress-based forming limit curve can be expressed by a stress-based instability criterion, e.g. the Bressan-Williams-Hill criterion [38] or by stress-based fracture criteria, e.g. the maximum shear stress criterion [39] and the maximum stress norm criterion [40]. These criteria do not explicitly take into account the accumulative deterioration of the material, but do account for this in an implicit way when used with an isotropic yield surface that expands with accumulative plastic strain.

In a finite element model where fracture is to be included, the deformation of the material needs to be given a sufficiently good description if the fracture initiation and propagation is to be well captured. The choice of fracture criterion depends on the problem to be modelled. For analysis of large structures (e.g. cars or ships), a number of simplifications are typically done in the numerical model to reduce the computational time. Shell elements are often used, which again simplify the geometry, and the constitutive relation is often given a relatively simple description. Effects like stochastic variations in the material or geometrical imperfections are usually not modelled, but can have a significant influence of local or global buckling as well as fracture, and can be readily included at a low computational cost [41-43]. In problems involving large structures the use of an uncoupled damage accumulation criterion, see Refs. [44-45], or a stress based criterion, see Ref. [45], may be sufficient. On the other hand, if local phenomena like localized necking or shear-band instability are to be captured, more sophisticated models are required. Localized necking can be captured by shell elements if a non-local approach is used, cf. [46]. However, the use of 3D solid elements is preferred if a detailed description of the deformation is needed. If the material displays anisotropic behaviour in terms of work hardening or plastic flow, advanced models of the constitutive relation are needed, e.g., Hill [47] or Cazacu and Barlat [48]. The fracture criterion for this type of problem should express the deterioration of the material as an accumulative variable in order to capture the physical process with microvoid nucleation growth and coalescence as well as breaking of bonds. In case of modelling slant shear fracture the effect of damage should be coupled with the constitutive relation [49-50].

As for the modelling of the crack propagation, several techniques exist, such as node splitting [51-52], cohesive elements [53-55], remeshing adaptivity [56-57] and the extended finite element method [58-59]. A method that is relatively simple, robust and has proven to work well in problems involving large deformations is the element erosion technique [60-62]. In this technique, the load-carrying capacity of the element is set to zero when the fracture criterion is met at one or more integration points. The technique is readily used for problems involving coarse spatial discretizations with shell elements [44-45] as well as in detailed modelling of local material instabilities with 3D solid elements e.g. [60, 63-64]. When using element erosion, it is preferable with small time increments due to the non-linear behaviour emerging when one element is deleted. Generally both implicit and explicit time integration can be used, but for quasi-static problems the normal advantage of implicit time integration is not as substantial, since small increments are needed to ensure a stable solution. In analysis with explicit time integration, the mass is lumped to the nodes and so mass is conserved even if one element is deleted. If all elements connected to a node are deleted, the node's mass still contributes to the total kinetic energy, and the node can still be used in contact constraints. In case of an implicit solver this situation is problematic as there is no stiffness contribution to the node, and the system of equations becomes singular. In the explicit non-linear finite element code LS-DYNA [65], the integration points belonging to a deleted element are simply skipped in the material subroutine. When the first element is deleted in an explicit analysis, the elastic energy stored in the neighbouring elements is released and induces stress waves. In problems where fracture is not preceded by strain localization, the history variables in the neighbouring elements are nearly the same as in the first deleted element. In these cases the stress waves might cause that many elements are eroded in this region within the next few time increments. Damage softening reduces this effect, and another aspect is that ductile fracture is usually preceded by strain localization. Aside from being numerically robust in explicit analyses, one of the main strengths of the element erosion technique is that the prediction of crack propagation is straight forward. The fracture criterion is evaluated in each integration point of the element, and the element is deleted when the criterion is fulfilled in one or more of the integration points (typically one for solids and several for shells). In this perspective the crack propagation can be viewed upon as a sequence of fracture initiations in the eroded elements.

In this study the fracture characteristics in terms of the stress triaxiality, the Lode parameter and the equivalent strain at fracture of the 2 mm thick Docol 600DL steel sheet is determined by quasi-static mechanical experiments with optical field measurements and numerical simulations. The crack surface of selected specimens has been studied in a scanning electron microscope and it was found that the fracture mechanism was nucleation, growth and coalescence of microvoids. Various uncoupled ductile fracture criteria have been calibrated to the material and assessed with respect to fracture initiation and damage evolution. The main criteria investigated were the modified Mohr-Coulomb criterion [23] found in literature and novel extensions of the Cockcroft-Latham and Rice-Tracey criteria. The modified Mohr-Coulomb and extended Cockcroft-Latham criteria were further implemented in a user-defined material model in LS-DYNA and used in explicit finite element simulations of ductile crack propagation of the dual-phase steel sheet. The sheet was discretized using tri-linear solid elements and the element erosion technique was used to model the crack propagation.

2 Objectives and scope

The objectives of this work are to gain knowledge of instabilities, ductile fracture mechanisms, and modelling of ductile fracture and crack propagation in a high-strength steel sheet. The main objectives can be summarized as the following:

- Investigate the potential of the digital image correlation technique for collecting information of the ductile fracture characteristics of sheet materials
- Propose a ductile fracture criterion that explicitly accounts for the Lode dependence, and assess the criterion for fracture initiation
- Evaluate the criterion as well as modelling techniques for crack propagation within the framework of the finite element method

Some limitations are apparent in this study. The material was chosen due to its macroscopically isotropic behaviour, which should make the constitutive modelling reasonable to handle. For anisotropic ductile materials more considerations need to be taken. Further, the study is limited to quasi-static loading rates and behaviour at room temperature, so the effects of high strain rates and elevated temperatures are not considered. As for the crack propagation modelling, only preliminary studies on other techniques than the element erosion technique were preformed (these were the extended finite element method and the node-splitting method). Since the results obtained in the preliminary studies were not encouraging, it was chosen to focus on the element erosion technique.

3 Summary of work

The work in this PhD thesis is presented as four independent journal articles which are published or submitted for possible publication in international scientific journals. In the following the articles are referred to as Part I-IV, as they represent four different parts of the thesis. In Part I and II the experimental work is presented, while Part III addresses various ductile fracture criteria calibrated to the experimental data from Parts I and II. In Part IV, numerical models of the tests from Part I are used in assessing selected fracture criteria from Part III with respect to crack propagation. The titles of the journal articles are presented in Table 1, followed by a short summary of each part.

Table 1 Journal articles included in the thesis.

Part	Journal articles
I	Gruben G, Fagerholt E, Hopperstad OS and Børvik T *Fracture characteristics of a cold-rolled dual-phase steel* European Journal of Mechanics – A/Solids, 2011(30), p.204-218
II	Gruben G, Vysochinskiy D, Coudert T, Reyes A and Lademo O-G *Determination of ductile fracture parameters of a dual-phase steel by optical measurements* Submitted for possible journal publication, 2012
III	Gruben G, Hopperstad OS and Børvik T *Evaluation of uncoupled ductile fracture criteria for the dual-phase steel Docol 600DL* International Journal of Mechanical Sciences, 2012(62), p.133-146
IV	Gruben G, Hopperstad OS and Børvik T *Simulation of ductile crack propagation in dual-phase steel* Submitted for possible journal publication, 2012

Part I

In Part I, mechanical tests using five different test set-ups were carried out. The specimens (uniaxial tension, plane-strain tension, in-plane shear and 45 and 90 degree modified Arcan) were cut from 2 mm thick sheets of the dual-phase steel Docol 600DL. The force and displacement were measured by the hydraulic test machine, and optical field measurements of the tests were conducted using the Digital Image Correlation (DIC) technique. Finite element (FE) simulations of the tests were run to gain information of the stress and strain state during deformation. From the FE simulations, the stress triaxiality, the Lode parameter and the equivalent strain histories at the point of fracture initiation were collected and used to describe the fracture characteristics of the material. Additionally, a novel method for determination of the stress triaxiality, the Lode parameter and the equivalent strain from the optical measurements was presented and applied on the tests. The method gave average values of the stress triaxiality and Lode parameter as well as fracture strain values that were in good agreement with the results from the FE simulations. Only moderate variations in the ductility were found in these tests, see Fig. 3 below. In general it was found that fracture is most likely to initiate in the through-thickness centre of the specimens where the stress triaxiality and the equivalent strain is higher. In the shear test it was not possible to determine whether fracture initiated on the surface where the strains are larger or in the centre where the triaxiality is larger.

Part II

In this study Marciniak-Kuczynski and Nakajima formability tests conducted on material from the same batch as used in Part I were presented. The DIC based method for experimental determination of the stress triaxiality, the Lode parameter and the equivalent strain presented in Part I was utilized on the formability tests. The main finding was that the material displays a significant drop in ductility in plane-strain tension stress-state compared to shear, uniaxial and biaxial tension, cf. Fig. 3. High magnification fractographs of selected formability tests revealed that fracture occurred due to void growth and coalescence, and that this mechanism was mainly present in localized areas controlled by shear-band instability. A verification of the experimental method in collecting the fracture parameters was also carried out, utilizing the FE models from Part I.

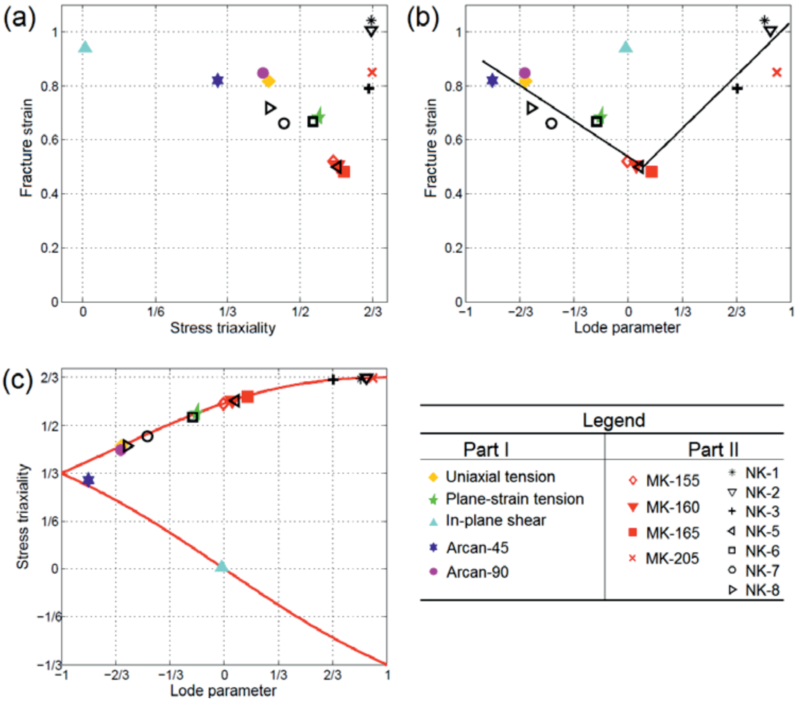

Fig. 3 Results derived from optical measurements in Part I and Part II. (a) Gives fracture strain as function of stress triaxiality, (b) shows fracture strain as function of Lode parameter and (c) displays the position of the various experiments in the stress triaxiality – Lode parameter space together with the plane stress locus.

Part III

In Part III, three uncoupled criteria for ductile fracture were applied on data from the tests presented in Part I. The criteria were the Modified Mohr-Coulomb (MMC) criterion found in the literature and novel extensions of the Rice-Tracey (ERT) criterion and the Cockcroft-Latham (ECL) criterion, as well as sub-versions of the latter two criteria. The stress and strain histories taken at the through-thickness centre in the FE models were used in assessing the criteria. Additionally, the data from the surface of the specimens in Part I and Part II collected by the DIC based method was applied in evaluating the ability of the fracture criteria to predict fracture initiation. The predicted fracture strain as function of stress-state for each criterion was evaluated. It was found that the three criteria possessed a similar topology in the triaxiality-Lode-fracture strain space, although some variation in the range of predicted fracture strain was apparent due to the different basis of the three criteria, see Fig. 4. The damage accumulation as function of equivalent strain for the three criteria was presented. In the case of the MMC and ECL criteria the damage is almost linear with the equivalent plastic strain, while it is exponential with the equivalent plastic strain for the ERT criterion. The shape of the exponential damage evolution is similar to the evolution of void area fraction in a comparable steel material. For each criterion, the predicted and experimental equivalent strains at fracture initiation were compared on the two datasets. Due to its flexibility, the ECL criterion proved to give a good fit to both datasets, while a somewhat larger spread was observed using the ERT and in particular the MMC criteria.

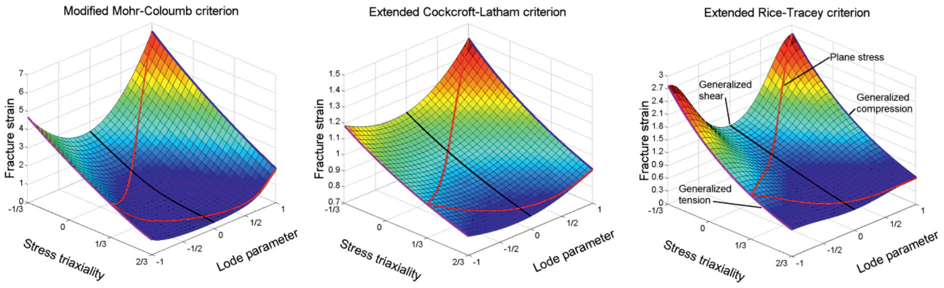

Fig. 4 Predicted fracture strain as function of stress triaxiality and Lode parameter for MMC, ECL and ERT criteria. The loci comprising generalized shear, generalized tension, generalized compression and plane stress are marked. Note that the range in fracture strain differs significantly in the different plots.

Part IV

Part IV focused on crack-path prediction in FE simulations with the modified Mohr-Coulomb and the extended Cockcroft-Latham fracture criteria, as well as the sub-versions of the ECL criterion; the Cockcroft-Latham criterion and the integral-based Tresca criterion. Additionally the effect of different shapes of the yield surface is assessed. The test specimens presented in Part I were discretized with solid elements and crack propagation was simulated by means of the element erosion technique in the explicit finite element code LS-DYNA version 971 [65]. The main conclusion is that the predicted force-displacement curves and crack paths were only to a small degree influenced by the fracture criterion and it is hard to select one fracture criterion that outperforms the others, see Fig. 5. It was further found that only small changes in the predicted force-displacement curves and crack paths were obtained when changing from the von Mises to the Hershey yield criterion with a high exponent. Slant fracture as observed in some of the experimental tests was captured in the numerical simulations if material softening was accounted for and a sufficiently fine mesh was used. The prediction of slant fracture did, however, not have any significant effect on the global response as represented by the force-displacement curves.

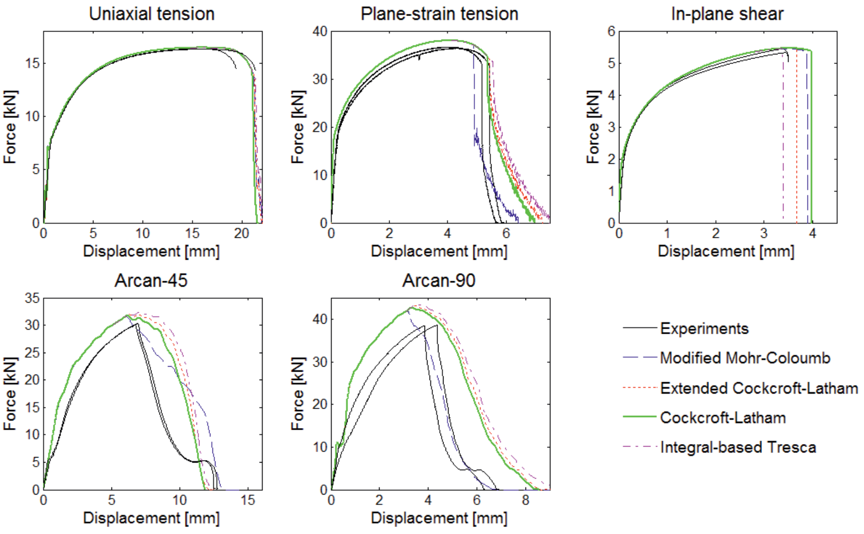

Fig. 5 Force-displacement curves from the tests performed in Part I, and simulations with different fracture criteria and J_2 plasticity from Part IV.

4 Concluding remarks

The fracture properties of the 2 mm thick dual-phase steel-sheet Docol 600DL have been investigated by means of quasi-static mechanical experiments, numerical models and high-magnification fractography. First a series consisting of uniaxial tension, plane-strain tension, in-plane shear and modified Arcan tests were carried out, and later a test series of Marciniak-Kuczynski and Nakajima formability tests were conducted. The test specimens were in a near plane-stress state during testing and covered a range from pure shear to biaxial tension (i.e. $0 \leq \sigma^* \leq \frac{2}{3}$). The material displays macroscopically a ductile behaviour with large values of equivalent strain at fracture. A significant drop in ductility was observed in plane-strain tension compared to pure shear, uniaxial tension and biaxial tension. Microscopically the material displayed ductile dimples that indicate that the mechanism governing fracture is nucleation, growth and coalescence of microvoids in the stress range investigated. It is further clear that fracture was preceded by shear-band instability.

Three uncoupled ductile fracture criteria that accounts for stress triaxiality and Lode dependence have been calibrated to the Docol 600DL material. These where the modified Mohr-Coulomb (MMC) criterion found in literature, and novel extensions of the Rice-Tracey (ERT) and the Cockcroft-Latham (ECL) criteria. The predicted fracture strain as function of stress triaxiality and Lode parameter had a similar topology in the three criteria. However the range in fracture strain predicted by the MMC criterion was larger than in ERT and ECL criteria. The MMC and ECL criteria displayed a near linear evolution of damage as function of equivalent stain, while the ERT criterion displayed an exponential damage evolution that may have a better shape compared to the damage evolution in the material. The ECL criterion predicted well the equivalent strain at fracture on two different datasets from respectively the through-thickness centre of the test specimens of the first test series and from the surface of the test specimens from both test series. On the other hand the ERT criterion and in particular the MMC criterion displayed a larger spread in the prediction of the fracture strain on the two datasets.

The MMC and ECL criterion were implemented as a user-defined material model in the non-linear finite element software LS-DYNA [65] and utilized in numerical simulations of the specimens from the first test series. Despite these two criteria gave a significantly different response in the fracture initiation investigation, the crack-paths predicted by these criteria as well as the resulting force-displacement curves were quite similar. The effect of changing from the von Mises to the Hershey yield criterion with a high exponent was investigated and it was found that this gave only small changes in the predicted force-displacement curves and crack paths. Slant fracture as observed in the experimental uniaxial tension and plane-strain tension tests was captured in the numerical simulations if material softening was accounted for and for a sufficiently fine mesh. The prediction of slant fracture did, however, not have any significant effect on the global response as represented by the force-displacement curves.

5 Suggestions for further work

Based on the work in this thesis, the following suggestions may give interesting information about high-strength steel-sheet materials or aspects concerning numerical modelling of such materials.

Experimental:

- A closer study on the material by use of SEM analyses with emphasis on the void nucleation and growth in the material during deformation could be carried out. Here the mechanisms that control void nucleation could be quantified. In other words quantify the percentage of voids that initiate due to debonding between the ferrite/martensite interface compared to the amount of voids that initiate at inclusions or due to cracking of martensite particles. Further, an investigation could be carried out on how the voids that initiate by the different mechanisms expand during plastic deformation, and a quantification of the void volume fraction could be carried out. The methods proposed by Avramovic-Cingara et al. [10] could be applied on the uniaxial tensile specimens carried out in Part I.
- New experiments in the negative regime of stress triaxiality e.g. plane-strain compression from rolling of plates, as well as tests with non-radial loading e.g. plane-strain compression followed by uniaxial tension could be conducted. By applying SEM analysis on such experiments, information about the different void initiation mechanisms under negative triaxiality and how they affect the ductility under both negative and positive stress triaxiality could be achieved.
- Experiments could be carried out to investigate the effect of higher strain rates on the ductility for the material, and compare this with the fracture criteria presented in Part III.

Numerical:

- Finite element models with eight-node solid elements could be made of the Marciniak-Kuczynski and Nakajima formability tests in order to investigate the stress and strain state in the through thickness centre of the specimens during deformation.
- The fracture criteria, yield functions and damage softening applied in Part IV could be tested on the numerical models of the formability tests.
- The prediction of fracture initiation and propagation of the coupled, shear-modified extended Gurson model [19] could be tested.
- FE models of the modified Arcan tests could be run with very dense meshes and damage coupling in order to see whether this would give a more accurate description of the drop in force level as well as the in-plane crack-path and the through-thickness slant fracture.

6 References

[1] Polmear I, Light Alloys; From Traditional Alloys to Nanocrystals, Fourth ed., Butterworth-Heinemann, 2006.

[2] Euro NCAP. http://www.euroncap.com/history.aspx (Accessed: 24.05.2012)

[3] Fifth gear. Channel 5. http://www.youtube.com/watch?v=qBDyeWofcLY (Accessed: 24.05.2012)

[4] Olsson K, Gladh M, Hedin J-E, Larsson J. Microalloyed High-Strength Steels. Advanced Materials & Processes magazine August 2006.

[5] SSAB (2009) Docol DP/DL Cold reduced dual phase steels. Swedish Steel AB. http://www.ssab.com/Global/DOCOL/datasheets_docol/en/201_Docol%20DP%20DL.pdf (Accessed: 27.04.2012)

[6] McClintock FA. Criterion for ductile fracture by growth of holes. J Appl Mech 1968;35:363-371.

[7] Rice JR, Tracey DM. On the ductile enlargement of voids in triaxial stress fields. J Mech Phys Sol 1969;17:201-217.

[8] Lemaitre J, A course on Damage Mechanics, Springer-Verlag, 1992.

[9] Lemaitre J, Chaboche J-L, Mechanics of solid materials, Cambridge University Press, 1990.

[10] Avramovic-Cingara G, Saleh CAR, Jain MK, Wilkinson DS. Void Nucleation and Growth in Dual-Phase Steel 600 during Uniaxial Tensile Testing. Metallurg Mat Trans: A 2009;40(13):3117-3127.

[11] Wu T, Coret M, Combescure A. Strain Localisation and Damage Measurement by Full 3D Digital Image Correlation: Application to 15-5PH Stainless Steel. Strain 2011;47(1):49-61.

[12] Clausing DP. Effect of plastic strain state on ductility and toughness. Int J Fract 1970;6(1):71-85.

[13] Bao Y, Wierzbicki T. On fracture locus in the equivalent strain and stress triaxiality space. Int J Mech Sci 2004;46:81-98.

[14] Barsoum I, Faleskog J. Rupture mechanisms in combined tension and shear—Experiments. Int J Solids Struct 2007;44(6):1768-1786.

[15] Mohr D, Ebnoether F. Plasticity and fracture of martensitic boron steel under plane stress conditions. Int J Solids Struct 2009;46(20):3535-3547.

[16] Dunand M, Mohr D. Hybrid experimental-numerical analysis of basic ductile fracture experiments for sheet metals. Int J Solids Struct 2010;47(9):1130-1143.

[17] Gao X, Kim J. Modeling of ductile fracture : Significance of void coalescence. Int J Solids Struct 2006;43:17.

[18] Barsoum I, Faleskog J. Rupture mechanisms in combined tension and shear—Micromechanics. Int J Solids Struct 2007;44(17):5481-5498.

[19] Nahshon K, Hutchinson JW. Modification of the Gurson Model for shear failure. Eur J Mech - A/Solids 2007;27(1):1-17.

[20] Wierzbicki T, Bao Y, Lee Y-W, Bai Y. Calibration and evaluation of seven fracture models. Int J Mech Sci 2005;47(4-5):719-743.

[21] Kim J, Zhang G, Gao X. Modeling of ductile fracture: Application of the mechanism-based concepts. Int J Solids Struct 2007;44(6):1844-1862.

[22] Bai Y, Wierzbicki T. A new model of metal plasticity and fracture with pressure and Lode dependence. Int J Plasticity 2008;24(6):1071-1096.

[23] Bai Y, Wierzbicki T. Application of extended Mohr–Coulomb criterion to ductile fracture. Int J Fract 2010;161(1):1-20.

[24] Lode W. Versuche fiber den Einfluß der mittleren Hauptspannung auf das Fließen der Metalle Eisen, Kupfer und Nickel. Zeitschrift für Physik: A 1926;36:913-939.

[25] Shima S, Oyane M. Plasticity theory for porous metals. Int J Mech Sci 1976;18(6):285-291.

[26] Gurson AL. Continuum theory of ductile rupture by void nucleation and growth, 1. Yield criteria and flow rules for porous ductile media. J Eng Mat Tech 1977:2-15.

[27] Rousselier G. Ductile fracture models and their potential in local approach of fracture. Nucl Eng Design 1987;105(1):97-111.

[28] Freudenthal AM, The Inelastic Behaviour of Solids, Wiley, New York, 1950.

[29] Cockcroft MG, Latham DJ. Ductility and the workability of metals. J Inst Met 1968;96:33-39.

[30] Wilkins ML, Streit RD, Reaugh JE. Cumulative-strain-damage model of ductile fracture: simulation and prediction of engineering fracture tests. Technical Report UCRL-53058, 1980.

[31] Johnson GR, Cook WH. Fracture characteristics of three metals subjected to various strains, strain rates, temperatures and pressures. Eng Fract Mech 1985;21(1):31-48.

[32] Børvik T, Hopperstad OS, Berstad T, Langseth M. A computational model of viscoplasticity and ductile damage for impact and penetration. Eur J Mech - A/Solids 2001;20(5):685-712.

[33] de Borst R, Damage, Material Instabilities, and Failure. Encyclopedia of Computational Mechanics, Wiley, 2004.

[34] Xue L, Ductile Fracture Modeling - Theory, Experimental Investigation and Numerical Verification, Massachusetts Institute of Technology, Department of Mechanical Engineering, 2007

[35] Keeler SP, Backhofen WA. Plastic instability and fracture in sheet streched over rigid punches. ASM Transactions Quarterly 1964;56:25-48.

[36] Goodwin GM. Application of strain ananlysis to sheet metal forming in the press shop. SAE paper, No. 680093, 1968.

[37] Stoughton TB. A general forming limit criterion for sheet metal forming. Int J Mech Sci 2000;42(1):1-27.

[38] Alsos HS, Hopperstad OS, Törnqvist R, Amdahl J. Analytical and numerical analysis of sheet metal instability using a stress based criterion. Int J Solids Struct 2008;45(7–8):2042-2055.

[39] Stoughton TB, Yoon JW. A new approach for failure criterion for sheet metals. Int J Plasticity 2011;27(3):440-459.

[40] Khan AS, Liu H. A new approach for ductile fracture prediction on Al 2024-T351 alloy. Int J Plasticity 2012;35(0):1-12.

[41] Fyllingen Ø, Hopperstad OS, Langseth M. Stochastic simulations of square aluminium tubes subjected to axial loading. International Journal of Impact Engineering 2007;34(10):1619-1636.

[42] Dørum C, Hopperstad OS, Berstad T, Dispinar D. Numerical modelling of magnesium die-castings using stochastic fracture parameters. Eng Fract Mech 2009;76(14):2232-2248.

[43] Lönn D, Fyllingen Ø, Nilssona L. An approach to robust optimization of impact problems using random samples and meta-modelling. International Journal of Impact Engineering 2010;37(6):723-734.

[44] Simonsen BC, Törnqvist R. Experimental and numerical modelling of ductile crack propagation in large-scale shell structures. Marine Structures 2004;17(1):1-27.

[45] Alsos HS, Amdahl J, Hopperstad OS. On the resistance to penetration of stiffened plates, Part II: Numerical analysis. International Journal of Impact Engineering 2009;36(7):875-887.

[46] Wang T, Hopperstad OS, Lademo OG, Larsen PK. Finite element modelling of welded aluminium members subjected to four-point bending. Thin-Walled Structures 2007;45(3):307-320.

[47] Hill R. Constitutive modelling of orthotropic plasticity in sheet metals. J Mech Phys Sol 1990;38(3):405-417.

[48] Cazacu O, Barlat F. A criterion for description of anisotropy and yield differential effects in pressure-insensitive metals. Int J Plasticity 2004;20(11):2027-2045.

[49] Belytschko T, Black T. Elastic crack growth in finite elements with minimal remeshing. Int J Num Meth Eng 1999;45(5):601-620.

[50] Li Y, Luo M, Gerlach J, Wierzbicki T. Prediction of shear-induced fracture in sheet metal forming. J Mat Proc Tech 2010;210(14):1858-1869.

[51] Kazutake K. Simulation of chevron crack formation and evolution in drawing. International Journal of Mechanical Sciences 1999;41(12):1499-1513.

[52] Komori K. Ductile fracture criteria for simulating shear by node separation method. Theor Appl Fract Mech 2005;43(1):101-114.

[53] Needleman A. An analysis of decohesion along an imperfect interface. Int J Fract 1990;42(1):21-40.

[54] Tvergaard V. Crack growth predictions by cohesive zone model for ductile fracture. J Mech Phys Sol 2001;49(9):2191-2207.

[55] Tvergaard V, Hutchinson JW. Effect of strain-dependent cohesive zone model on predictions of crack growth resistance. Int J Solids Struct 1996;33(20-22):3297-3308.

[56] Bouchard PO, Bay F, Chastel Y, Tovena I. Crack propagation modelling using an advanced remeshing technique. Comp Met Appl Mech Eng 2000;189(3):723-742.

[57] Mediavilla J, Peerlings RHJ, Geers MGD. A robust and consistent remeshing-transfer operator for ductile fracture simulations. Comp Struct 2006;84(8-9):604-623.

[58] Fagerström M, Larsson R. Theory and numerics for finite deformation fracture modelling using strong discontinuities. Int J Num Meth Eng 2006;66(6):911-948.

[59] Areias PM. Analysis of Finite Strain Anisotropic Elastoplastic Fracture in Thin Plates and Shells. J Aerosp Eng 2006;19(4):259.

[60] Xue L, Wierzbicki T. Ductile fracture initiation and propagation modeling using damage plasticity theory. Eng Fract Mech 2008;75(11):3276-3293.

[61] Fagerholt E, Dørum C, Børvik T, Laukli HI, Hopperstad OS. Experimental and numerical investigation of fracture in a cast aluminium alloy. Int J Solids Struct 2010;47(24):3352-3365.

[62] Kane A, Børvik T, Berstad T, Benallal A, Hopperstad OS. Failure criteria with unilateral conditions for simulation of plate perforation. Eur J Mech - A/Solids 2011;30(4):468-476.

[63] Li Y, Wierzbicki T, Sutton M, Yan J, Deng X. Mixed mode stable tearing of thin sheet AI 6061-T6 specimens: experimental measurements and finite element simulations using a modified Mohr-Coulomb fracture criterion. Int J Fract 2011;168(1):53-71.

[64] Nielsen KL, Hutchinson JW. Cohesive traction–separation laws for tearing of ductile metal plates. International Journal of Impact Engineering 2012;48:15-23.

[65] LSTC, LS-DYNA keyword user's manual, version 971, Livermore Software Technology Corporation, 2007.

Part I

G. Gruben, E. Fagerholt, O.S. Hopperstad, T. Børvik

Fracture characteristics of a cold-rolled dual-phase steel

European Journal of Mechanics A/Solids 30 (2011) 204-218

European Journal of Mechanics A/Solids 30 (2011) 204–218

Contents lists available at ScienceDirect

European Journal of Mechanics A/Solids

journal homepage: www.elsevier.com/locate/ejmsol

Fracture characteristics of a cold-rolled dual-phase steel

G. Gruben [a,*], E. Fagerholt [a], O.S. Hopperstad [a], T. Børvik [a,b]

[a] Structural Impact Laboratory (SIMLab), Centre for Research-based Innovation (CRI), Department of Structural Engineering, Norwegian University of Science and Technology, Rich. Birkelands vei 1A, NO-7491 Trondheim, Norway

[b] Norwegian Defence Estates Agency, Research & Development Department, PB 405, Sentrum, NO-0103 Oslo, Norway

ARTICLE INFO

Article history:
Received 15 June 2010
Accepted 21 January 2011
Available online 1 February 2011

Keywords:
Fracture initiation
Docol 600DL
Digital image correlation

ABSTRACT

In this study, the fracture characteristics of a cold-rolled, low-strength, high-hardening steel sheet (Docol 600DL) under quasi-static loading conditions are established using five different test set-ups. In all the tests, the sheet material is initially in plane-stress states. Optical field measurements with digital image correlation were used to determine the strain fields to fracture, to calibrate the material model for the sheet material and to validate the finite element models of the tests. Based on the field measurements, a novel method for experimental determination of the stress triaxiality and the Lode parameter is presented for isotropic materials and plane-stress states. These parameters were also obtained from finite element simulations. Comparisons show that the two methods give approximately the same average values of the stress triaxiality and the Lode parameter up to fracture. The sheet material displays only moderate variation in ductility as a function of the stress triaxiality and the Lode parameter within the investigated range of these parameters. The most critical through-thickness position in the specimens was found to be in the centre where the strains and the stress triaxiality are highest.

1. Introduction

The equivalent strain at fracture, $\bar{\varepsilon}_f$, is a convenient measure of a metal's ductility. Knowing the history of the equivalent strain, $\bar{\varepsilon}$, (neglecting the elastic component) and how its fracture value, $\bar{\varepsilon}_f$, is affected by the stress state, makes it possible to predict fracture in a specific material. Bridgman (1952) found through his experiments that the ductility is strongly increasing with decreasing hydrostatic stress, σ_h. This phenomenon was later explained by McClintock (1968) and Rice and Tracey (1969) to be due to the restraining of the void growth inside the grains of the metal. In the modelling of void nucleation, growth and coalescence, the stress triaxiality, σ^*, is commonly used as a parameter representing the hydrostatic stress state (McClintock, 1968; Rice and Tracey, 1969; Hancock and Mackenzie, 1976). More recent studies on an aluminium alloy conducted by Bao and Wierzbicki (2004a,b) have indicated that the equivalent strain at fracture has a local maximum in the lower region of stress triaxiality (≈ 0.4). A similar observation was reported by Barsoum and Faleskog (2007) who conducted plane-strain experiments on mid-strength and high-strength steels. However, in that study the local maximum was observed at a higher triaxiality (≈ 0.9). Based on the observations from Bao and Wierzbicki (2004a,b) and other experiments, Wierzbicki et al. (2005), Bai and Wierzbicki (2008) and Bai et al. (2009) argued that the fracture strain is also depending on the deviatoric stress state of the material. This conclusion was supported by Gao and Kim (2006) and Kim et al. (2007) who studied the effect of the stress state on $\bar{\varepsilon}_f$, based on numerical modelling of microvoids in a representative material volume. The deviatoric stress state can conveniently be represented by the Lode parameter, μ (Lode, 1926).

Bridgman (1952) used analytical expressions based on continuum mechanics in finding the stress and strain values in the neck of the material test specimens. He experimentally proved that the assumption of constant strain over the neck in an axisymmetric specimen was proper, and found an expression for the stress distribution over the neck, based on the specimen geometry, boundary conditions, the equations of equilibrium and the von Mises yield function. This type of analysis made it possible to calculate stress and strain parameters with reasonable accuracy for a large range of material test specimens. The global stress and strain field values in the specimen are however not captured by this type of analysis. With the development of computers and computational mechanics, it became possible to calculate the field values as well as more accurate values in the neck of the specimens. Wilkins et al. (1980) described in detail how a numerical model can be adapted to the experiment and give information about the stress and strain history. The use of numerical models has been the main method in collecting stress and

---

[*] Corresponding author. Tel.: +47 73 59 46 87; fax: +47 73 59 47 01.
E-mail address: gaute.gruben@ntnu.no (G. Gruben).

0997-7538/$ – see front matter © 2011 Elsevier Masson SAS. All rights reserved.
doi:10.1016/j.euromechsol.2011.01.004

strain values since their introduction (Wilkins et al., 1980; Hancock and Brown, 1983; Johnson and Cook, 1985; Børvik et al. 2003; Bao and Wierzbicki, 2004b; El-Magd and Abouridouane, 2006). Mohr and Oswald (2008) presented a new experimental technique for calculating the strain and stress fields during loading in butterfly-shaped plane-stress specimens under various stress states. The fields were found using a combination of optical measurements, the measured force and the geometric relations of the test specimen. Mohr and Ebnoether (2009) used this methodology in deriving the equivalent strain and the stress triaxiality history for a martensitic boron steel.

In this paper, the fracture characteristics of a low-strength, high-hardening, cold-rolled steel of type Docol 600DL are determined, using mechanical tests, full-field measurements and finite element analysis. The experiments are performed on specimens cut from a 2 mm thick sheet. Five different specimen geometries are used to vary the stress state. The equivalent strain at fracture, $\bar{\varepsilon}_f$, is obtained as a function of the stress state as represented by the stress triaxiality, σ^*, and the Lode parameter, μ. A novel method for experimental determination of σ^* and μ is presented for isotropic materials and plane-stress states. The method is based on accurate measurements of the displacement field using Digital Image Correlation (DIC) and assumes a Levy-Mises material, i.e. von Mises yield function, associated flow rule and neglectable elastic strains, see e.g. Hill (1950).

The paper is organized as follows. Section 2 describes the material and the various experimental set-ups. In Section 3, the procedures for mechanical testing with DIC are presented, along with the method used to calculate the strain fields from the displacement fields derived with the DIC method. The experimental results in form of force-displacement curves and strain values from the different tests are presented in Section 4. A method for describing the stress state in terms of σ^* and μ from the strain values is given in Section 5. In Section 6, a description of the Finite Element (FE) models of the various material tests is given, while the material's fracture characteristics derived from the field measurements and the FE analyses are presented in Section 7.

2. Experimental tests and set-ups

2.1. Material

The material is a low-strength, high-hardening, cold-rolled steel of type Docol 600DL supplied by Swedish Steel Ltd. (SSAB). It was delivered as a 2 mm sheet. The steel is subjected to a heat treatment which produces a two-phase structure of ferrite and martensite, where the ferrite gives the formability features and the strength is dependent on the martensite proportion. Table 1 gives the nominal chemical composition of the material (SSAB, 2009). The nominal yield strength is reported from the manufacturer to be in the range from 280 MPa to 360 MPa, while the nominal tensile strength is reported to be between 600 MPa and 700 MPa.

2.2. Mechanical testing

Experiments were carried out using 5 different test set-ups. All the experiments were conducted at room temperature with strain rates of about 10^{-3} s^{-1}. The specimens were cut from the 2 mm thick sheet with the longitudinal axis along the rolling direction. An exception from this is the tension tests, which in addition had specimens cut with longitudinal axis 45° and 90° to the rolling direction. Two successful tests from each set-up are presented, again with the tension tests as an exception with three tests presented in each direction.

Table 1
Chemical composition of Docol 600DL (in wt%).

C	Si	Mn	P	S	Al_{tot} %
0.10	0.40	1.50	0.010	0.002	0.040

2.2.1. Uniaxial tension tests

The uniaxial tension tests were carried out using 200 mm long tensile specimens with a gauge length of 70 mm, see Fig. 1(a). The tensile specimens were numbered UT-*XX*-*Y* where *XX* marks the angle (0°,45°,90°) between the rolling direction of the plate and the longitudinal axis of the specimen, and *Y* is the specimen number (1,2,3) for each angle. The cross-head velocity of the actuator was 2 mm/min, which corresponds to an average strain rate of approximately 0.5×10^{-3} s^{-1} before necking. The force, F, and the displacement, u, were measured by the hydraulic test machine at 10 Hz for all the tests, and the displacement field was measured using DIC for all the tests except for UT-00-1 and UT-45-1. In addition, an extensometer with gauge length of 40 mm was used to measure displacement for tests UT-00-1, UT-45-1 and UT-90-1.

The initial cross-section area was measured at three locations, at the centre of the gauge length and 30 mm from the centre in both longitudinal directions. It was found that the average initial cross-section area varied from 24.6 mm^2 to 25.2 mm^2. From the tension tests the engineering stress was calculated as $\tilde{s} = F/A_0$, where F is the measured force and A_0 is the initial cross-section area. DIC measurements were used to calculate the engineering strain, $\tilde{e} = (l - l_0)/l_0$, where l and l_0 are the current and initial gauge lengths (in pixels), respectively. The curves were plotted with $\tilde{e}$ as the abscissa and $\tilde{s}$ as the ordinate and corrected for the abscissa offset. Precautions were taken so that the engineering stress and the engineering strain are coherent in time. The corrected values, e and s, were used to calculate the Cauchy stress $\sigma = s(1+e)$, and the logarithmic strain, $\varepsilon = \ln(1+e)$. The logarithmic plastic strain was calculated from $\varepsilon^p = \varepsilon - \sigma/\bar{E}$ where $\bar{E} = 178$ GPa is the calculated modulus of elasticity from the elastic part of the $\sigma - \varepsilon$ curve. Note that the calculated value of the modulus of elasticity is not necessarily representing the real value, as more detailed experiments are needed to establish this property.

The Cauchy stress tensor in the gauge area before necking is theoretically expressed as $\boldsymbol{\sigma} = \sigma_{XX}\mathbf{e}_X \otimes \mathbf{e}_X$, where $\mathbf{e}_X$ is a unit vector in the longitudinal direction of the specimen, see Fig. 1. This gives a theoretical initial stress triaxiality $\sigma_0^* = 1/3$ and an initial Lode parameter $\mu_0 = -1$, see Equations (21) and (23).

2.2.2. Plane-strain tension tests

The plane-strain tension test specimens have a gauge length of 15 mm, which is smaller than the gauge width of 26 mm, see Fig. 1 (b). This geometry exerts a nearly plane-strain condition due to the confinement of the deformation over the relatively short length. This precludes the contraction over the width to a greater extent than what is the case for an ordinary uniaxial tension test.

Two tests were conducted with a velocity of 0.56 mm/min. Assuming that the deformation is mainly distributed over a length of 15 mm, this gives an average strain rate of approximately 0.6×10^{-3} s^{-1} before necking. During the experiments the specimens were clamped 24.5 mm from the longitudinal edges. The initial cross-section area at the centre of the specimens was measured respectively to 50.73 mm^2 and 50.95 mm^2. The force and the displacement were measured by the servo-hydraulic testing machine at 10 Hz.

Assuming plane strain in the in-plane transverse to the longitudinal direction at the centre of the specimen, the theoretical Cauchy stress tensor is expressed as $\boldsymbol{\sigma} = \sigma_{XX}\mathbf{e}_X \otimes \mathbf{e}_X + 1/2\sigma_{XX}\mathbf{e}_Y \otimes \mathbf{e}_Y$, where $\mathbf{e}_Y$ is the in-plane normal to $\mathbf{e}_X$ following the right hand rule, see Fig. 1. Here, the von Mises yield criterion and the associated flow

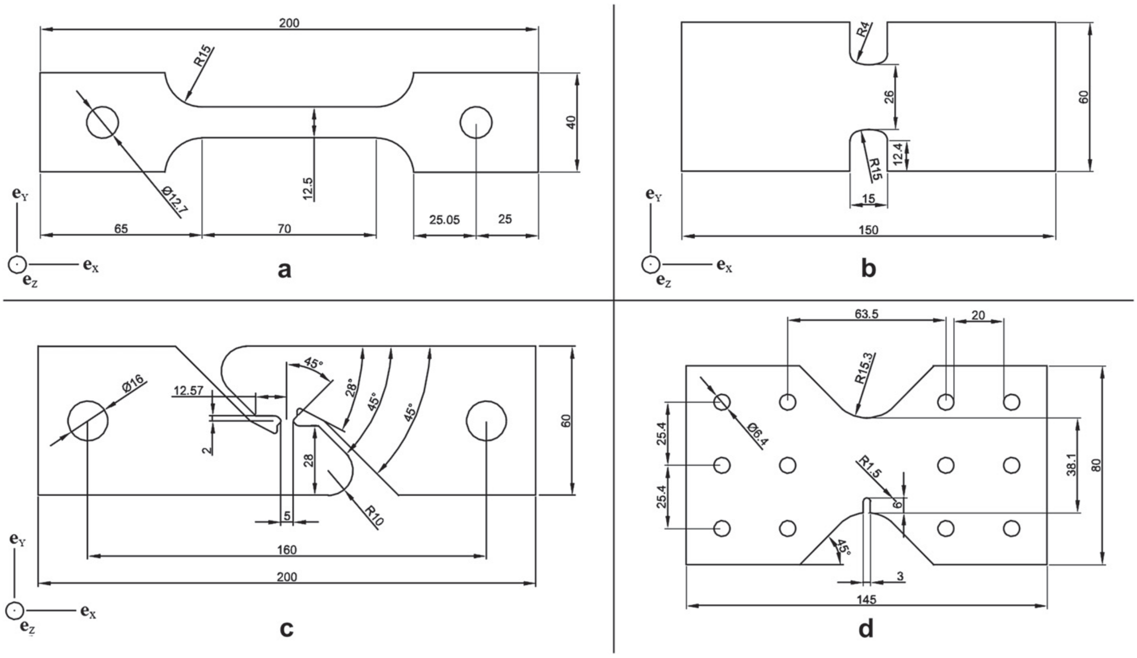

Fig. 1. Geometry of the test specimens (in mm): (a) uniaxial tension specimen, (b) plane-strain tension specimen, (c) in-plane shear specimen, and (d) modified Arcan specimen.

rule have been assumed. The initial equivalent and hydrostatic stresses in the centre of the specimen are then expressed as $\bar{\sigma} = \sqrt{3}/2\sigma_{XX}$ and $\sigma_{\mathrm{h}} = 1/2\sigma_{XX}$, respectively, giving an initial triaxiality $\sigma_0^* = \sqrt{3}/3 \approx 0.58$ and an initial Lode parameter $\mu_0 = 0$.

2.2.3. In-plane shear tests

The geometry of the shear specimens used in this study was developed by Eriksson et al. (2006) based on a design proposed by Bao and Wierzbicki (2004b) for fracture tests in the regime of low stress triaxiality. The specimen is designed to obtain predominant shear deformation under plane-stress conditions and to avoid plastic instability. Two successful shear tests were performed with a cross-head velocity of 0.42 mm/min, which gives a strain rate of about $1.4 \times 10^{-3}\ \mathrm{s}^{-1}$. Fig. 1(c) shows the geometry and dimensions of the specimen. The two specimens were measured with a slide calliper in the gauge area, and the measured thickness was 1.96 mm and the measured length was 5.15 mm for both specimens. The force was measured by the servo-hydraulic test machine and the displacement by an extensometer with gauge length of 40 mm. These measurements were recorded at 10 Hz.

If a pure shear stress state is assumed, the stress tensor in the gauge area is expressed as $\boldsymbol{\sigma} = \sigma_{XY}\mathbf{e}_X \otimes \mathbf{e}_Y + \sigma_{YX}\mathbf{e}_Y \otimes \mathbf{e}_X$. The initial stress triaxiality and Lode parameter are consequently equal to zero, i.e. $\sigma_0^* = \mu_0 = 0$.

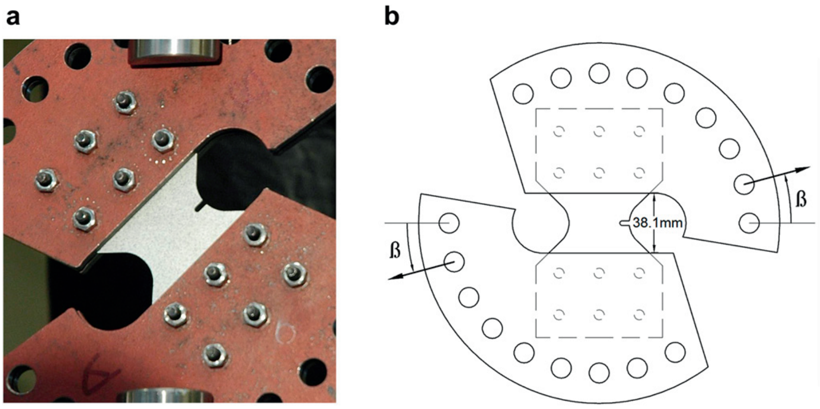

Fig. 2. (a) Modified Arcan test set-up with $\beta = 45°$, and (b) sketch of brackets with specimen defining the loading direction β.

2.2.4. Modified Arcan tests

The experimental set-up for the modified Arcan test is illustrated in Fig. 2. The set-up is a modification based on the work by Voloshin and Arcan (1980), which in turn is based on the original specimen presented by Arcan et al. (1978). A test series was carried out with loading direction, β, set to 45° and 90°, see Fig. 2. The test set-ups were labelled Arcan-β to specify the loading direction. Two successful tests were conducted for each loading direction. The notched specimens, shown in Fig. 1(d), were mounted in the four loading brackets using 12 M6-bolts. The thickness was measured at three locations in the gauge area and practically no deviation was found within each specimen. The thickness was in the range 1.95–1.97 mm for the different specimens. The width of the gauge area was also measured, and found to be 32.1 mm for all the specimens. The tests were conducted with a cross-head velocity of 1 mm/min. Force and displacement were recorded by the hydraulic test machine at 10 Hz.

Due to the complex geometry of the notched Arcan specimen, the initial stress state and strain rate of the material have to be determined through FE analysis.

3. DIC procedures and calculation of strain field values

Prior to the tests, one side of the specimen was spray painted with a combination of black and white paint, obtaining a fine-grained and high-contrast speckle pattern that was used to enhance the optical measurements. During testing, 8-bit grey-scale images of the speckle-patterned specimen surface were recorded at a framing rate of 2 Hz using a Prosilica GC2450 digital camera equipped with a 28–105 mm Nikon lens. The spatial resolution of the recorded images was 2448 × 2050 pixels. The recorded images were post-processed using an in-house two dimensional DIC software (Fagerholt et al., submitted for publication), obtaining information on displacement and strain fields on the surface of the specimens. Table 2 gives the element size used in the DIC mesh of the different tests. The camera was pre-arranged with its optical axis normal to the specimen surface. A linear relationship between coordinates on the specimen surface and the image coordinates is assumed in the DIC analysis.

The DIC algorithm is essentially based on the conservation of optical flow. The displacement fields are calculated by carrying out a global optimization of the nodal displacements in a mesh of quadrilateral elements. This “finite element” DIC method is based on the procedure proposed by Besnard et al. (2006). The strain fields are then calculated from the nodal displacements in a similar manner as in total Lagrangian, non-linear FE methods. Let $u = u(\mathbf{X},t)$ and $v = v(\mathbf{X},t)$ be the displacement fields in the $\mathbf{e}_X$ and $\mathbf{e}_Y$ directions, and $\mathbf{X} = X\mathbf{e}_X + Y\mathbf{e}_Y$ the material coordinates and t the time. Assuming the continuum hypothesis, the displacement inside a “DIC element” can be expressed using a standard FE formulation as

$$u = \mathbf{N}_0\mathbf{d}_X, \quad v = \mathbf{N}_0\mathbf{d}_Y \tag{1}$$

where $\mathbf{d}_X = \mathbf{d}_X(t)$ and $\mathbf{d}_Y = \mathbf{d}_Y(t)$ are column vectors containing the measured nodal displacements in the $\mathbf{e}_X$ and $\mathbf{e}_Y$ directions of the DIC element, and $\mathbf{N}_0 = \mathbf{N}_0(\xi,\eta)$ is a row vector containing the shape functions for a standard isoparametric Q4 element, where (ξ,η) are the coordinates of the parent element, see e.g. Cook et al. (2002). The in-plane displacement gradient is then calculated as

$$\frac{\partial \mathbf{u}}{\partial \mathbf{X}} = \begin{bmatrix} \dfrac{\partial \mathbf{N}_0}{\partial X}\mathbf{d}_X & \dfrac{\partial \mathbf{N}_0}{\partial Y}\mathbf{d}_X \\ \dfrac{\partial \mathbf{N}_0}{\partial X}\mathbf{d}_Y & \dfrac{\partial \mathbf{N}_0}{\partial Y}\mathbf{d}_Y \end{bmatrix} \tag{2}$$

where $\mathbf{u} = u\mathbf{e}_X + v\mathbf{e}_Y$. The derivatives in Equation (2) are conveniently calculated from the derivatives with respect to the natural coordinates and the inverse of the Jacobi matrix as

$$\begin{Bmatrix} \dfrac{\partial \mathbf{N}_0}{\partial X} \\ \dfrac{\partial \mathbf{N}_0}{\partial Y} \end{Bmatrix} = \frac{1}{\dfrac{\partial X}{\partial \xi}\dfrac{\partial Y}{\partial \eta} - \dfrac{\partial X}{\partial \eta}\dfrac{\partial Y}{\partial \xi}} \begin{bmatrix} \dfrac{\partial Y}{\partial \eta} & -\dfrac{\partial Y}{\partial \xi} \\ -\dfrac{\partial X}{\partial \eta} & \dfrac{\partial X}{\partial \xi} \end{bmatrix} \begin{Bmatrix} \dfrac{\partial \mathbf{N}_0}{\partial \xi} \\ \dfrac{\partial \mathbf{N}_0}{\partial \eta} \end{Bmatrix} \tag{3}$$

The material coordinates inside the element are found from isoparametric mapping, $X = \mathbf{N}_0\mathbf{c}_X$ and $Y = \mathbf{N}_0\mathbf{c}_Y$, where $\mathbf{c}_X$ and $\mathbf{c}_Y$ are the material nodal coordinates in the $\mathbf{e}_X$ and $\mathbf{e}_Y$ directions. The displacement gradient is evaluated at the centre of the element ($\xi = \eta = 0$), which corresponds to the superconvergent integration point in linear analysis for rectangular elements. The deformation gradient tensor, $\mathbf{F} = \mathbf{F}(\mathbf{X},t)$, is now calculated from

$$\mathbf{F} = \frac{\partial \mathbf{u}}{\partial \mathbf{X}} + \mathbf{I} \tag{4}$$

where $\mathbf{I}$ is the second order identity tensor. The right Green deformation tensor, $\mathbf{C} = \mathbf{C}(\mathbf{X},t)$, is then obtained using

$$\mathbf{C} = \mathbf{F}^{\mathrm{T}}\cdot\mathbf{F} \tag{5}$$

The principal in-plane stretches, $\lambda_i = \lambda_i(\mathbf{X},t)$, $i = 1,2$, are found from solving the eigenvalue problem for the right Green deformation tensor

$$\left(\lambda_i^2\mathbf{I} - \mathbf{C}\right)\cdot\mathbf{n}_i = \mathbf{0} \tag{6}$$

where $\mathbf{n}_i$, $i = 1,2$, are the principal in-plane directions of $\mathbf{C}$. The logarithmic in-plane principal strains, $\varepsilon_i = \varepsilon_i(\mathbf{X},t)$, $i = 1,2$, are then calculated as

$$\varepsilon_i = \ln(\lambda_i) \tag{7}$$

Assuming plastic incompressibility and negligible elastic strains the out-of-plane principal strain, ε_Z, is estimated as

$$\varepsilon_Z = -(\varepsilon_1 + \varepsilon_2) \tag{8}$$

The effective logarithmic strain, $\varepsilon_{\mathrm{e}} = \varepsilon_{\mathrm{e}}(\mathbf{X},t)$, is here defined by

$$\varepsilon_{\mathrm{e}} = \sqrt{\frac{2}{3}\left(\varepsilon_1^2 + \varepsilon_2^2 + \varepsilon_Z^2\right)} = \sqrt{\frac{4}{3}\left(\varepsilon_1^2 + \varepsilon_1\varepsilon_2 + \varepsilon_2^2\right)} \tag{9}$$

where the relation from Equation (8) is used in the last part. The in-plane Green strain tensor is calculated from

$$\mathbf{E} = \frac{1}{2}\left(\mathbf{F}^{\mathrm{T}}\cdot\mathbf{F} - \mathbf{I}\right) \tag{10}$$

To gain information of the stress state of the material from the DIC recordings, objective strain increments were needed. The increment in Green strain is expressed as

$$\Delta\mathbf{E} = \frac{1}{2}\left(\mathbf{F}_{n+1}^{\mathrm{T}}\cdot\mathbf{F}_{n+1} - \mathbf{F}_n^{\mathrm{T}}\cdot\mathbf{F}_n\right) \tag{11}$$

where $\mathbf{F}_{n+1}$ and $\mathbf{F}_n$ are the deformation gradients at the increments $n+1$ and n respectively. The rate-of-deformation tensor, $\mathbf{D}$, is achieved by the push-forward of $\Delta\mathbf{E}$ as

Table 2
Characteristic element size in DIC analyses (in mm).

Tension	Plane strain	Shear	Arcan-45	Arcan-90
0.90	0.55	0.22	0.51	0.56

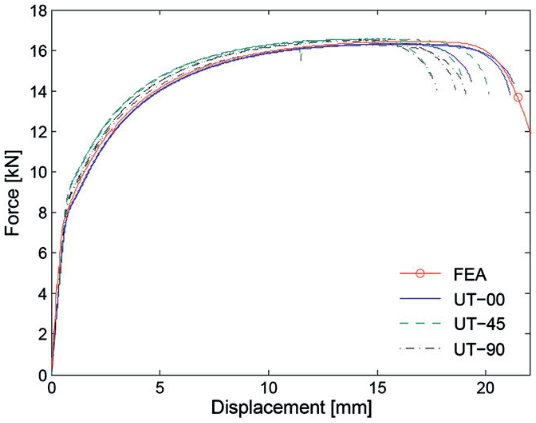

Fig. 3. Force–displacement (F–u) curves from the tension tests and the FE simulation. The circle marks the point of initial fracture assumed in the simulation.

$$\Delta t\mathbf{D} = \mathbf{F}_{n+1}^{-\mathrm{T}}\cdot\Delta\mathbf{E}\cdot\mathbf{F}_{n+1}^{-1} \tag{12}$$

Since **D** vanishes in a rigid rotation, incremental objectivity is ensured (Belytschko et al., 2000). The in-plane principal strain increments, $\Delta\varepsilon_i$, $i = 1,2$, are then calculated by solving the eigenvalue problem

$$(\Delta\varepsilon_i\mathbf{I} - \Delta t\mathbf{D})\cdot\overline{\mathbf{n}}_i = \mathbf{0} \tag{13}$$

where $\overline{\mathbf{n}}_i,\ i = 1,2$ are the corresponding direction vectors. By assuming plastic incompressibility, and neglecting elastic strains, the through-thickness strain increment is estimated as

$$\Delta\varepsilon_Z = -(\Delta\varepsilon_1 + \Delta\varepsilon_2) \tag{14}$$

The equivalent strain, $\overline{\varepsilon}$, is calculated by summing up the equivalent strain increments, $\Delta\overline{\varepsilon}$ as

$$\overline{\varepsilon} = \sum\Delta\overline{\varepsilon} = \sum\sqrt{\frac{2}{3}\left(\Delta\varepsilon_1^2 + \Delta\varepsilon_2^2 + \Delta\varepsilon_Z^2\right)} \tag{15}$$

Under proportional loading, the equivalent strain, Equation (15), and the effective logarithmic strain, Equation (9), give the same values.

4. Experimental results

4.1. Uniaxial tension tests

Fig. 3 shows the force–displacement (F–u) curves measured by the servo-hydraulic test machine from the uniaxial tension tests. As seen, the material displays moderate anisotropy and the curves exhibit low spread within each direction. The location of necking in the gauge area was arbitrary from specimen to specimen, but all specimens fractured in a mode where the crack initiated in the centre of the neck and propagated in the transverse direction. Fig. 4 (a) shows one of the fractured specimens. Using the relations from Section 2, the σ–ε^{p} curve was calculated from the UT-00-3 test, see Fig. 5.

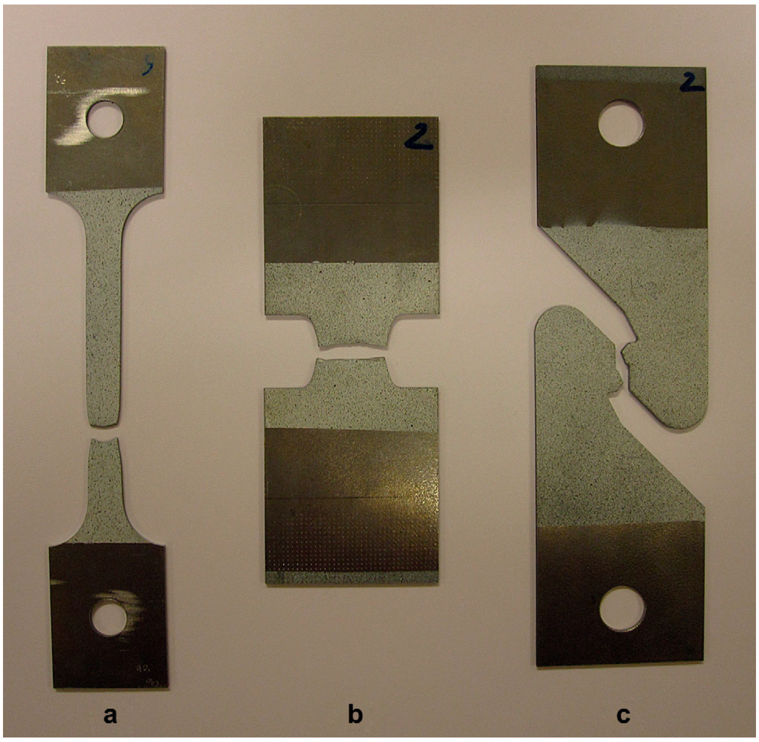

Fig. 4. Specimens after fracture: (a) uniaxial tension specimen, (b) plane-strain tension specimen, and (c) in-plane shear specimen.

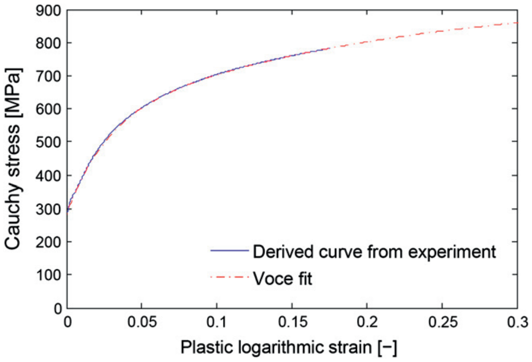

Fig. 5. Stress–strain (σ–ε^p) curve from UT-00-3 and fit to the extended Voce hardening rule.

4.2. Plane-strain tension and in-plane shear tests

The F–u curves for the plane-strain tension tests and the shear tests are given in Fig. 6. The displacement is measured by the servo-hydraulic test machine for the plane-strain tension tests and by an extensometer for the shear tests. The small jump in one of the F–u curves for plane-strain tension is due to a slip in the clamping during the experiment.

For the plane-strain tension tests the fracture initiated in the centre of the specimens, and propagated slowly towards the edges in the transverse direction. Fig. 4(b) shows that the deformation is larger at the centre of the fractured specimen. For the shear tests, fracture occurred almost simultaneously over the whole fracture area. The initiation point was not captured by the DIC recording, and could not be pinpointed during the test. A fractured specimen is shown in Fig. 4(c).

4.3. Modified Arcan tests

Fig. 6 shows the F–u curves for the modified Arcan tests measured by the hydraulic test machine. The Arcan-90 tests show some deviation in the displacement values. This is due to a small slip in the beginning of one of the tests. Fracture initiated close to the notch root in the Arcan-45 tests and in the notch root in the Arcan-90 tests. In the Arcan-45 tests the fracture propagated approximately 35° to the longitudinal direction of the specimen in the beginning and gradually changed into an almost perpendicular mode, see Fig. 7. The fracture in the Arcan-90 specimens propagated in the transverse direction of the specimen. The relatively slow propagation of the crack in all the modified Arcan tests is reflected in the gradual decrease in the force level in the F–u curves after the peak force value.

4.4. Strain fields

The strain fields were derived from one selected specimen from each test set-up. Figs. 8 and 9 show the effective logarithmic strain derived from the last image before fracture initiation for the selected specimens. The figures are plotted in the initial configuration. An arrow marks the point where the in-plane principal strains are collected from each test. This point corresponds to the point of fracture initiation for all the tests, except from the shear test. In the shear test, the point of fracture initiation was not

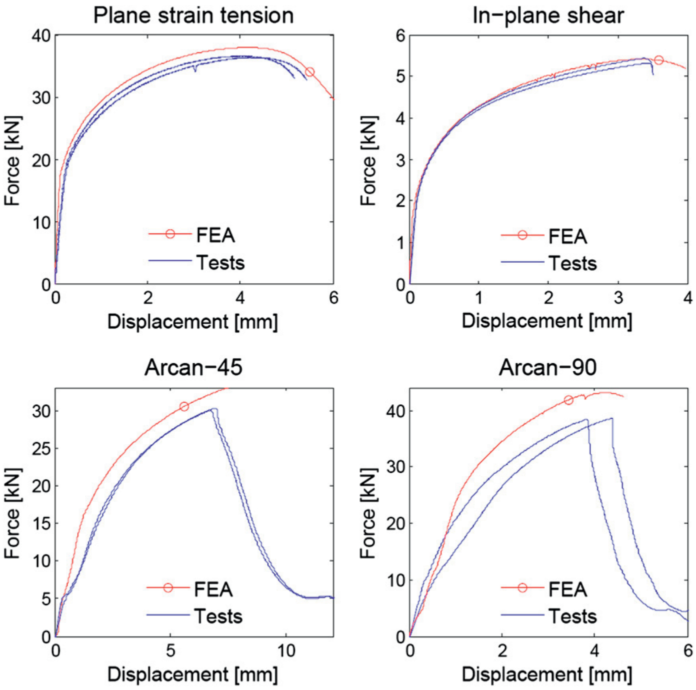

Fig. 6. Force–displacement curves from the plane-strain tension, shear and modified Arcan tests and corresponding FE simulations. The circle marks the point of initial fracture assumed in the FE simulation.

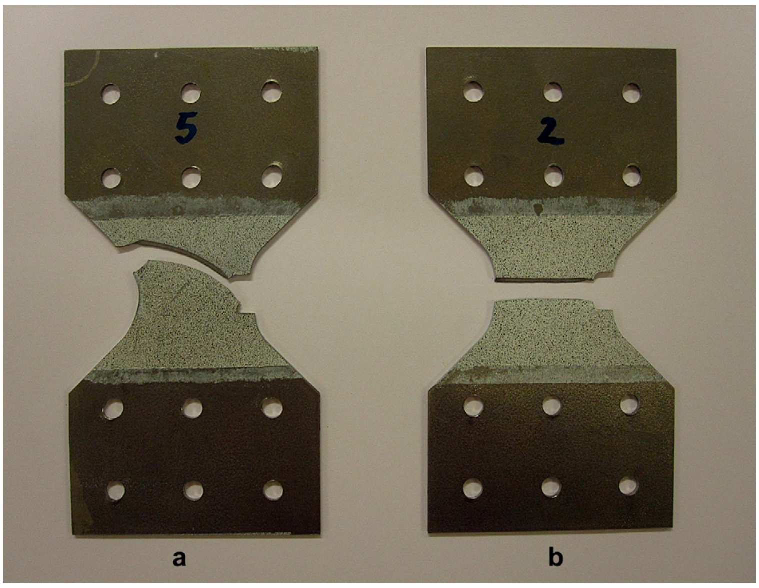

Fig. 7. Fractured specimens from the modified Arcan tests: (a) $\beta = 45^\circ$, and (b) $\beta = 90^\circ$.

accurately captured, and the point in the centre of the shear zone was chosen to represent the strain behaviour.

Fig. 10 presents the first in-plane principal strain versus the second in-plane principal strain from the experiments as obtained from the field measurements. As can be seen, all the tests except the plane-strain tension test, display a first in-plane principal strain approximately equal to 0.8 at fracture. The first in-plane principal strain at fracture is less and about 0.6 in the plane-strain tension test. The shear test displays an almost pure shear mode, while the plane-strain tension test gradually tends towards a plane-strain condition. The Arcan-90 and the tension test exhibit very similar behaviour, while the Arcan-45 test shows a somewhat larger magnitude of the second in-plane principal strain.

5. Stress-state parameters

On the surface of the specimens a plane-stress condition is fulfilled, and the principal stresses and principal strain increments are expressed as

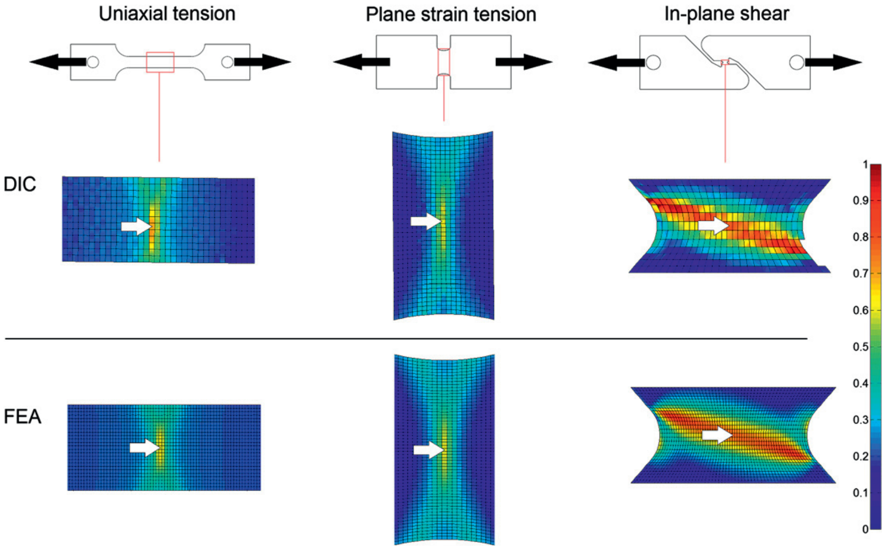

Fig. 8. Effective logarithmic strain fields for uniaxial tension, plane-strain tension and shear tests from DIC recordings and FE analyses. The elements used in collecting 2D principal strain values are marked with arrows.

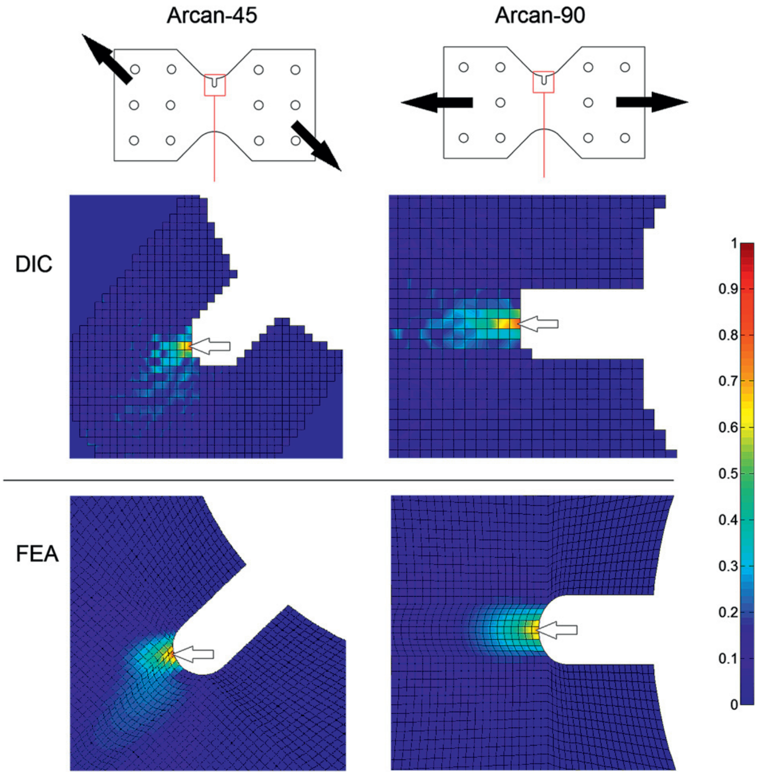

Fig. 9. Effective logarithmic strain fields for modified Arcan tests from DIC recordings and FE analyses. The elements used in collecting 2D principal strain values are marked with arrows.

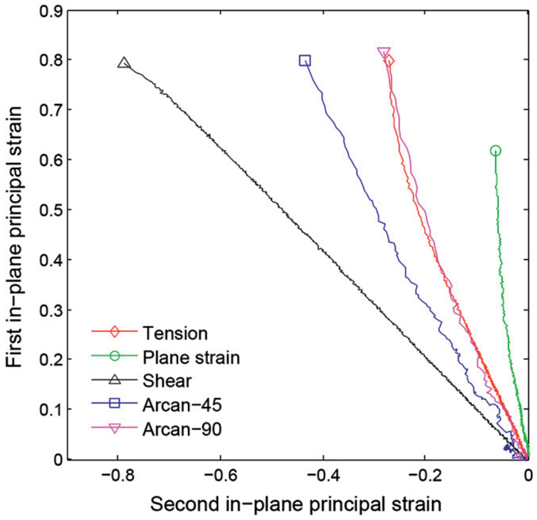

Fig. 10. In-plane principal strain paths to fracture based on the unsmoothed displacements from DIC recordings.

$$\sigma_1 > 0,\ \ \sigma_2 = \alpha\sigma_1,\ \ \sigma_Z = 0 \tag{16}$$

$$\Delta\varepsilon_1 > 0,\ \ \Delta\varepsilon_2 = \beta\Delta\varepsilon_1,\ \ \Delta\varepsilon_Z = -(\beta+1)\Delta\varepsilon_1 \tag{17}$$

Here (σ_1,σ_2) are the first and second in-plane principal stresses, while σ_Z is the principal stress in the thickness direction of the sheet. In our experiments, the first principal stress will always be positive, so this assumption has been adopted in the derivations. Analogously, $(\Delta\varepsilon_1,\Delta\varepsilon_2)$ are the first and second in-plane principal strain increments as defined by Equation (13), whereas $\Delta\varepsilon_Z$ is the principal strain increment in the thickness direction as defined by Equation (14). It is presupposed that the material is isotropic and that the elastic strains are negligible. The coefficients α and β are the stress ratio and the incremental strain ratio, respectively, which take values within the following ranges: $-\infty < \alpha \leq 1$ and $-2 < \beta \leq 1$. Under the assumption of a Levy-Mises material, the relation between α and β can be expressed as

$$\alpha = \frac{2\beta+1}{\beta+2},\quad \beta = \frac{2\alpha-1}{2-\alpha} \tag{18}$$

The hydrostatic stress can be expressed in terms of β by using Equations (16) and (18)

$$\sigma_{\rm h} = \frac{1}{3}(\sigma_{\rm I}+\sigma_{\rm II}+\sigma_{\rm III}) = \frac{1}{3}(\sigma_1+\sigma_2) = \frac{\beta+1}{\beta+2}\cdot\sigma_1 \tag{19}$$

where $(\sigma_{\mathrm{I}},\sigma_{\mathrm{II}},\sigma_{\mathrm{III}})$ are the principal stresses ordered so that $\sigma_{\mathrm{I}} \geq \sigma_{\mathrm{II}} \geq \sigma_{\mathrm{III}}$. For the plane-stress condition σ_{I} is always equal to σ_1, whereas σ_{II} equals σ_2 for $\alpha \geq 0$ (or $\beta \geq -1/2$) and σ_Z otherwise. The von Mises equivalent stress is in the same manner expressed as

$$\bar{\sigma} = \sqrt{\frac{1}{2}\left[(\sigma_{\mathrm{I}}-\sigma_{\mathrm{II}})^2+(\sigma_{\mathrm{II}}-\sigma_{\mathrm{III}})^2+(\sigma_{\mathrm{III}}-\sigma_{\mathrm{I}})^2\right]}$$
$$= \sqrt{\sigma_1^2+\sigma_2^2-\sigma_1\sigma_2} = \sqrt{3}\frac{\sqrt{\beta^2+\beta+1}}{\beta+2}\cdot\sigma_1 \tag{20}$$

The stress triaxiality is defined as the ratio of the hydrostatic stress and the von Mises equivalent stress:

$$\sigma^* = \frac{\sigma_{\mathrm{h}}}{\bar{\sigma}} \tag{21}$$

By using Equations (19) and (20) the stress triaxiality can be expressed in terms of β as

$$\sigma^* = \frac{\sqrt{3}}{3}\frac{\beta+1}{\sqrt{\beta^2+\beta+1}} \tag{22}$$

The Lode parameter (Lode, 1926), which characterizes the deviatoric part of the stress state, is defined as

$$\mu = \frac{2\sigma_{\mathrm{II}}-\sigma_{\mathrm{I}}-\sigma_{\mathrm{III}}}{\sigma_{\mathrm{I}}-\sigma_{\mathrm{III}}} \tag{23}$$

Under the plane-stress assumption, the Lode parameter is conveniently expressed in terms of β as

$$\mu = \begin{cases} 3\dfrac{\beta+1}{\beta-1} & \text{for } -2<\beta\leq-\dfrac{1}{2} \\ \dfrac{3\beta}{\beta+2} & \text{for } -\dfrac{1}{2}<\beta\leq 1 \end{cases} \tag{24}$$

In calculating the average values at fracture of the stress triaxiality and the Lode parameter, an integral expression over the equivalent strain is used

$$\sigma^*_{\mathrm{avg}} = \frac{1}{\bar{\varepsilon}_{\mathrm{f}}}\int_0^{\bar{\varepsilon}_{\mathrm{f}}}\sigma^*(\bar{\varepsilon})\mathrm{d}\bar{\varepsilon}\,, \quad \mu_{\mathrm{avg}} = \frac{1}{\bar{\varepsilon}_{\mathrm{f}}}\int_0^{\bar{\varepsilon}_{\mathrm{f}}}\mu(\bar{\varepsilon})\mathrm{d}\bar{\varepsilon} \tag{25}$$

where we recall that $\bar{\varepsilon}_{\mathrm{f}}$ is the equivalent strain at fracture.

As can be seen from the previous equations, σ^* and μ are derived values from the measured displacements. In order to achieve sensible results for σ^* and μ filtering was necessary. Several techniques were tested (moving average, Fourier analysis, polynomial curve fitting, spline curve fitting), and they all gave approximately the same results in terms of σ^*_{avg} and μ_{avg}. However, to avoid oscillations in the smoothed curves and their derivatives, low-order polynomials were found most suitable. The measured nodal displacements, $\mathbf{d}_X = \mathbf{d}_X(t)$ and $\mathbf{d}_Y = \mathbf{d}_Y(t)$, from the quadrilateral DIC element surrounding the point of fracture initiation in each test (see Figs. 8 and 9) were fitted by C^2 continuous cubic splines by the least squares method. Constraints were imposed on the splines so that the initial and final displacements in the smoothed curves were the same as in the original curves. The constraint in the final displacement ensures that the derived effective logarithmic strain at fracture, $\varepsilon_{\mathrm{e}}^{\mathrm{f}}$, from the smoothed curve is the same as it would be from the original curve, as this value depends on the final displacement only. The number of splines had to be evaluated for each test. The least possible number that still captured the trend in the displacement and effective logarithmic strain was sought. This resulted in 17 splines for the uniaxial tension test, 5 splines for the plane-strain and in-plane shear tests and 3 splines for the modified Arcan tests. The high number of splines for the uniaxial tension test stems from small displacements in the $\mathbf{e}_Y$ direction that turned out to be important in order to capture the deformation properly. The history of σ^* and μ from the experiments, as defined by Equations (22) and (24), was compared with the values from the surface of the FE simulations as defined by Equations (21) and (23). In this regard it was found convenient to use a spline fit also on the β value from Equation (17). Two cubic, C^2 continuous splines were fitted to the β–$\bar{\varepsilon}$ curves with a constraint on the final value. This did not significantly alter the average values of σ^*_{avg} and μ_{avg}, but gave smoother trend curves especially for uniaxial tension. It should be noted that also the equivalent strain, $\bar{\varepsilon}$, as defined by Equation (15), was derived from the smoothed displacement curves.

6. Numerical study

6.1. Material model

The nominal elastic properties were described by a Young's modulus of 210 GPa and a Poisson's ratio of 0.33. The material did not display much anisotropy, and the J_2 flow theory was found suitable to describe the plastic behaviour. A constitutive model was fitted to the σ–ε^{p} curve using the least squares method. The extended Voce rule with a multiplicative viscosity-hardening law was found adequate and is expressed as

$$\bar{\sigma} = \left(\sigma_0+\sum_{i=1}^{2}Q_i(1-\exp(-C_i\bar{\varepsilon}))\right)\left(1+\frac{\dot{\bar{\varepsilon}}}{\dot{\varepsilon}_0}\right)^q \tag{26}$$

where σ_0 is an adjustable parameter representing the yield stress and Q_i and C_i $(i = 1,2)$ are adjustable material parameters governing in turn the primary and secondary hardening. The parameters q and $\dot{\varepsilon}_0$ are material constants defining the strain-rate sensitivity, and $\dot{\bar{\varepsilon}}$ is the rate of the equivalent strain. In uniaxial tension the logarithmic strain is equal to the equivalent strain, and the Cauchy stress is equal to the equivalent stress. Thus, the derived σ–ε^{p} curve from the uniaxial tension test before diffuse necking was used as a basis for the plastic properties. In the calibration process of σ_0, Q_i and C_i, $\dot{\bar{\varepsilon}}$ was set to zero. The strain-rate sensitivity of the material was not explicitly investigated in this study, but as shown in Tarigopula et al. (2006) and Curtze (2009), appropriate values for q and $\dot{\varepsilon}_0$ in dual-phase steels are respectively 0.005 and 0.001. After the necking process has started in the material, the strain rate increases significantly and delays the evolution of the neck. The strain-rate sensitivity term is thus included to capture this effect.

To capture the post necking material behaviour, an iterative method similar to the one described by Bao and Wierzbicki (2004a) was used. The primary hardening in Equation (26) saturates for small strains, while the post necking stress is controlled by the secondary hardening. Using a small value for C_2 and a large value for Q_2 in Equation (26) yields an almost linear hardening for large strains. In the calibration process, the extended Voce model fitted to the pre-necking σ–ε^{p} curve was used in FE models of the tension and shear tests, and F–u curves from the FE simulations were compared with the measured ones. Then the C_2 value was adjusted to change the post necking behaviour. The other parameters in the extended Voce model were once again fitted using the least squares method. The F–u curves obtained in simulations with the new set of parameters were then compared to the measured ones, and this process was repeated until a satisfactory result was achieved. All the adjustable parameters in the extended Voce model are given in Table 3, and a comparison of the Voce fit and the derived σ–ε^{p} curve from experiment is shown in Fig. 5.

Table 3
Values used in the Voce hardening model.

σ_0 [MPa]	Q_1 [MPa]	C_1	Q_2 [MPa]	C_2
283.3	268.3	39.38	396.6	5

6.2. Finite element modelling

The implicit solver of the non-linear finite element code LS-DYNA (LSTC, 2007) was used in the simulations. The use of implicit time integration proved to be less time consuming than explicit time integration with mass scaling. The finite element analyses were run with 1000 increments which proved to be enough to capture the necking instability properly. Deviations from the geometry given in Fig. 1 were not taken into account in the FE models. The modified Johnson–Cook model (Børvik et al., 2001), *MAT_107 in LS-DYNA, was used in the simulations with a constitutive behaviour as described. For all the FE models 8-node, trilinear brick elements with selective reduced integration (LS-DYNA solid elform 2) were used. The FE models had 9 elements in the thickness direction. To capture the stress and strain state on the surface in the gauge area, a thin layer (10^{-4} mm) of Belytschko–Tsay shell elements (LS-DYNA shell elform 2) was merged with the surface nodes of the brick elements. The shell elements had the same material properties as the brick elements. Convergence tests were carried out on all the models to check for mesh size sensitivity, and the simulated time was approximately the same as the time observed in the experiments, i.e. $t \approx 600$ s.

The uniaxial tension test was modelled with deformable elements in the specimen while the bolts connecting the specimen to the hydraulic actuator were modelled using elements with rigid body definition. In Fig. 11(a) the specimen mesh is shown as shaded, while the meshes of the bolts are shown in white. In the gauge area 25 elements were used over the width and 141 elements over the length, giving an in-plane size of approximately 0.5×0.5 mm^2. A prescribed displacement of 6 mm was given to each of the bolts to simulate the loading. A node-to-surface contact algorithm without friction, using the bolts as master nodes, was used to describe the contact interface. To prevent out-of-plane movement, one node of the specimen part was constrained in the $\mathbf{e}_Z$-direction.

The FE model of the plane-strain tension specimen used rigid body definitions in the areas equivalent to the clamped areas of the test specimen. Fig. 11(b) shows the mesh of the model. The elements with rigid body definition are shown in white while the deformable elements are displayed as shaded. The rigid body assumption is a good approximation of the boundary conditions in the test, as the clamping prevents deformation in the transverse direction as well as in the longitudinal direction. The rigid body areas were given prescribed displacements equal to the loading in the test rig. The in-plane element size in the gauge area was approximately 0.5×0.5 mm^2.

In the shear tests, nearly all deformation appeared in the shear zone. In the FE model of the specimen, deformable elements were used in the area close to the shear zone. Fig. 11(c) shows the mesh with rigid elements in white and deformable elements as shaded. The rigid body parts were given a prescribed displacement to simulate the loading. The in-plane element size in the gauge area was approximately 0.1×0.1 mm^2. The elements are smaller in the model of the shear test specimen than the other models, since the gauge area is smaller and thus the deformation is more localized.

The modified Arcan specimen was modelled with deformable elements, while each of the loading brackets and the bolts connecting the specimen to the respective brackets were modelled with rigid elements. The cross-heads were also modelled with rigid body definition and the loading was applied to the cross-heads as a prescribed displacement. This model ensures that boundary conditions are given a correct description. Fig. 11(d) shows the FE model of the Arcan-45 test, where the deformable elements are

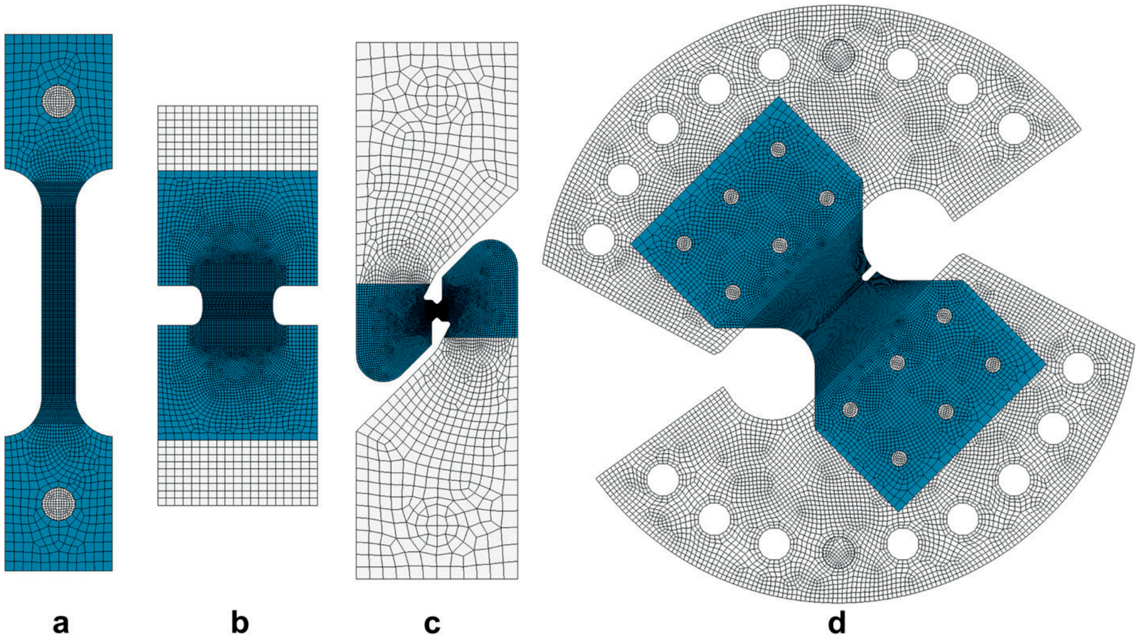

Fig. 11. Finite element meshes: (a) uniaxial tension test, (b) plane-strain tension test, (c) in-plane shear test and (d) Arcan-45 test.

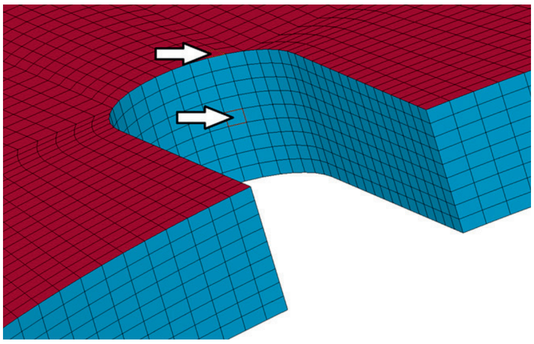

Fig. 12. Surface shell and centre brick elements used for picking history values in the Arcan-45 model.

shaded, whereas the rigid elements are white. Contact was handled in the same manner as in the model of the uniaxial tension test. Also the models of the modified Arcan specimen were constrained to prevent out-of-plane movement. The in-plane element size in the gauge area was approximately $0.3 \times 0.4\ \text{mm}^2$.

6.3. Collecting stress and strain values from the FE models

To investigate to which extent the equivalent strain, the stress triaxiality and the Lode parameter vary over the thickness of the specimens, surface shell and centre brick elements located at the same in-plane coordinates were used in collecting the stress and strain values. Fig. 12 shows the location of the two elements picked in the Arcan-45 model. The in-plane positions of the elements picked in the various models correspond to the positions where fracture initiated in the tests, except in the uniaxial tensile test where the effective logarithmic strain was slightly asymmetric in the experiment. The element with the highest effective logarithmic strain in the FE model was in this case selected. The selected elements are shown in Figs. 8 and 9.

The principal stresses were collected from LS-DYNA and post-processed in MATLAB to compute the stress triaxiality σ^* and the Lode parameter μ. The equivalent strain from the FE analysis, $\bar{\varepsilon}^{\text{FEA}}$, which is the work conjugate with the von Mises equivalent stress, was calculated from the plastic part of the rate-of-deformation tensor in LS-DYNA during the simulation and collected directly from the program.

6.4. Calculation of simulated time at fracture

To find the time at fracture, t_f, in the numerical simulations, different approaches have been reported in the literature. Wilkins et al. (1980) compared a photograph taken just before fracture initiation with the deformed numerical model, and the displacement over an area in the vicinity of the fracture initiation point was compared for finding t_f. Bao (2003) compared the global force–displacement curves to find the global displacement at fracture, and used this to determine t_f. Both methods are displacement

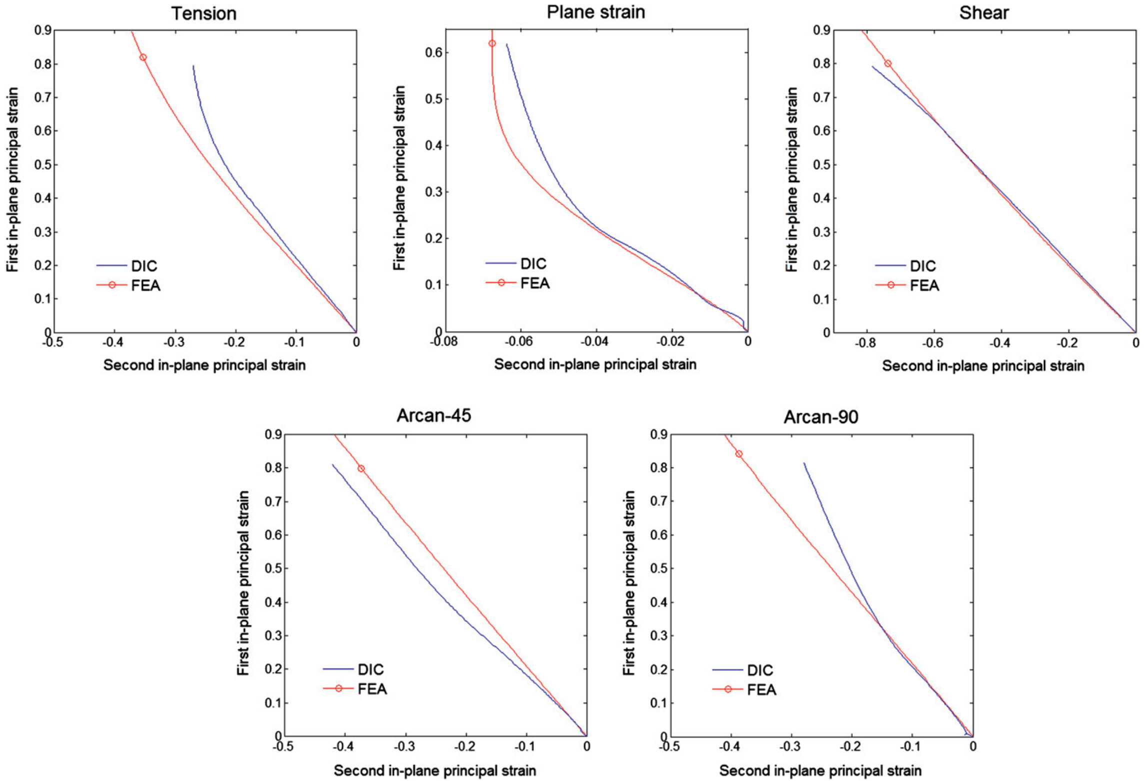

Fig. 13. In-plane principal strain paths to fracture from DIC recordings and FE analyses. The strains from the DIC analyses are based on the smoothed displacements. The circle marks the point of initial fracture assumed in the FE analysis.

based, i.e. the simulated time at fracture is found from the measured displacement at fracture, i.e. $u_f = u^{FEA}(t_f)$. In this study, a local strain-based criterion is used. The displacements at the nodes in the shell element corresponding to the location of fracture initiation, see Figs. 8 and 9, were collected and used to calculate the effective logarithmic strain, ε_e^{FEA}, by Equation (9). The simulation time at fracture, t_f, is taken as the time when ε_e^{FEA} is equal to the effective logarithmic strain at fracture, ε_e^f, from the DIC recording, i.e. $\varepsilon_e^f = \varepsilon_e^{FEA}(t_f)$. Fig. 13 shows the in-plane principal strain curves from the DIC and FE analyses calculated from Equation (7), where the circles on the FE curves mark the values at t_f. The deformation over a larger region around the fracture initiation point is also similar in the FE models and the test specimens. Figs. 8 and 9 show the effective logarithmic strain field from the last image before fracture initiation in the tests compared with the effective logarithmic strain field in the FE models at t_f.

7. Results and discussion

The results from the FE analyses in form of force–displacement curves are shown in Figs. 3 and 6. The circle on the FE curves marks the F–u values at the time of fracture initiation, t_f. The predicted force levels in the FE simulations of the plane-strain tension test and the modified Arcan tests show some deviation compared to the experimental results, see Fig. 6. This is at least partly attributed to the shape of the yield function in the deviatoric plane. The influence of J_3 through e.g. a higher exponent term in the yield function as proposed by Hosford (1972) tends to reduce the force level in these simulations. The global displacement at fracture in the simulations is in general close to the global displacement at fracture in the experiments. The exceptions are the simulations of the modified Arcan tests in which the displacement at fracture is somewhat lower than in the experiments.

The results from the DIC and FE analyses in form of $\bar{\varepsilon}$–σ^* and $\bar{\varepsilon}$–μ curves are shown in Fig. 14. Here Equations (15), (22) and (24) are used to determine the DIC values, while Equations (21) and (23) are used for calculating the stress state in the FE analyses. The equivalent strain in the FEA is collected directly from LS-DYNA. The fracture strain $\bar{\varepsilon}_f$ from the five tests is given in Table 4 as a function of the average values of the stress triaxiality, σ^*_{avg}, and the Lode parameter, μ_{avg}. The table also compares the values of σ^*_{avg} and μ_{avg} obtained with DIC and FE simulations. The stress state parameters σ^* and μ and the equivalent fracture strain, $\bar{\varepsilon}_f$, derived from the field measurements can be compared directly with those obtained from the surface shell elements in the FE analyses, as they are extracted from the same locations on the surface of the specimens.

The stress state parameters σ^* and μ as obtained by DIC and FEA, show significant difference. Looking at the $\bar{\varepsilon}$–σ^* curves in Fig. 14, the triaxiality at fracture, σ^*_f, is higher in the DIC analyses than the corresponding FE shell elements for the uniaxial tension and Arcan-90 tests. This stems from the higher convex curvature in the ε_1–ε_2 curves from the DIC analyses shown in Fig. 13. For the shear test, the value of σ^*_f extracted from the DIC measurements is lower than the corresponding value found from the FE analysis. This is coherent with the concave shape at the end of the ε_1–ε_2 shear curve from the DIC analyses, see Fig. 13. For the plane-strain tension test the ε_1–ε_2

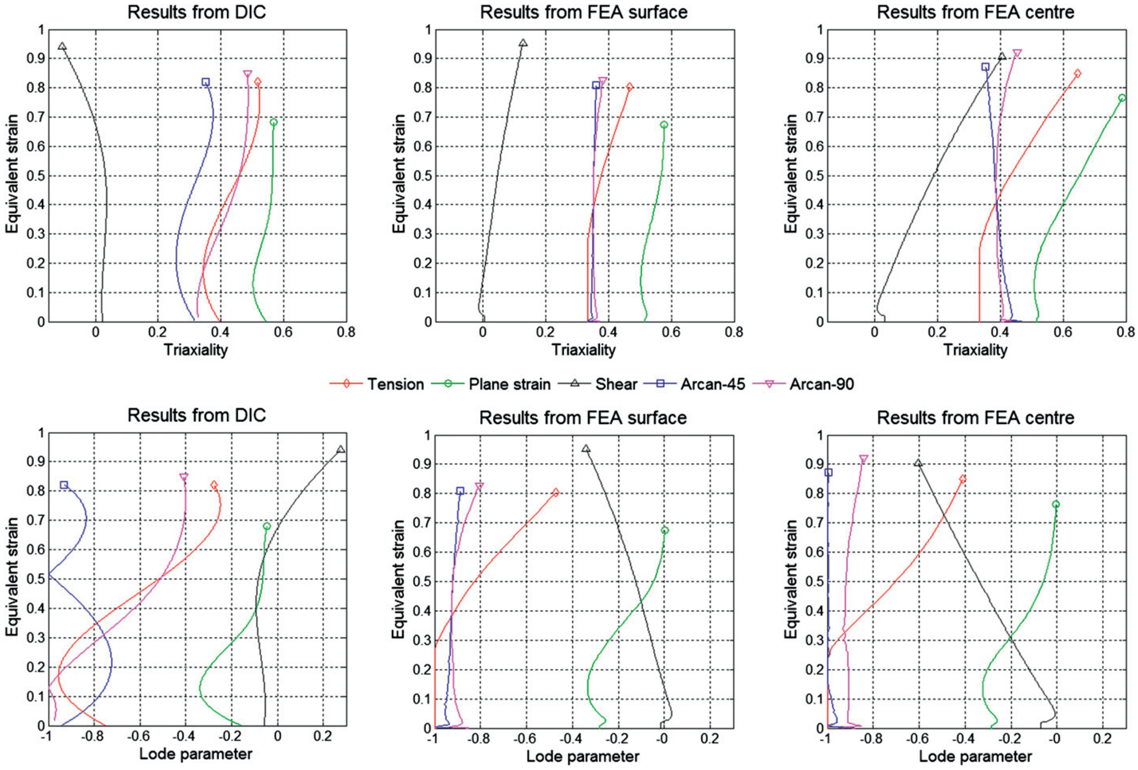

Fig. 14. Equivalent strain as function of triaxiality, $\bar{\varepsilon} = \bar{\varepsilon}(\sigma^*)$, or Lode parameter, $\bar{\varepsilon} = \bar{\varepsilon}(\mu)$, from DIC recordings, surface shell elements and centre brick elements.

Table 4
Effective logarithmic strain at fracture, equivalent strain at fracture and average values for the stress triaxiality and the Lode parameter at initial fracture in the different tests.

		DIC	FE surface	FE centre	Analytical
Uniaxial tension	ε_e^f	0.810		–	–
	$\bar{\varepsilon}_f$	0.818	0.804	0.849	–
	σ_{avg}^*	0.427	0.373	0.429	0.333
	μ_{avg}	−0.631	−0.846	−0.769	−1.000
Plane-strain tension	ε_e^f	0.680		–	–
	$\bar{\varepsilon}_f$	0.682	0.674	0.765	–
	σ_{avg}^*	0.542	0.539	0.609	0.577
	μ_{avg}	−0.167	−0.179	−0.154	0.000
In-plane shear	ε_e^f	0.912		–	–
	$\bar{\varepsilon}_f$	0.940	0.953	0.905	–
	σ_{avg}^*	0.005	0.049	0.178	0.000
	μ_{avg}	−0.013	−0.129	−0.301	0.000
Arcan-45	ε_e^f	0.812		–	–
	$\bar{\varepsilon}_f$	0.821	0.810	0.872	–
	σ_{avg}^*	0.311	0.352	0.391	–
	μ_{avg}	−0.836	−0.924	−0.993	–
Arcan-90	ε_e^f	0.829		–	–
	$\bar{\varepsilon}_f$	0.848	0.826	0.920	–
	σ_{avg}^*	0.415	0.358	0.401	–
	μ_{avg}	−0.637	−0.901	−0.902	–

and $\bar{\varepsilon}$–σ^* curves are similar in the DIC and FE analyses, while for the Arcan-45 test some deviations are again exhibited.

The deviations in the Lode parameter derived from the DIC measurements and the surface shell elements are larger than those for the stress triaxiality. This is as expected as a small variation in stress triaxiality results in a much larger variation in the Lode parameter when the two parameters are related through the plane-stress condition. This is illustrated by the slope of the plane-stress locus shown in Fig. 15. It is also noted that the $\bar{\varepsilon}$–μ curves from the modified Arcan tests, as obtained from the DIC results in Fig. 14, are not continuously differentiable at $\mu = -1$. At this point, $\beta = -0.5$ in Equation (24) and the expression for the Lode parameter in terms of β changes.

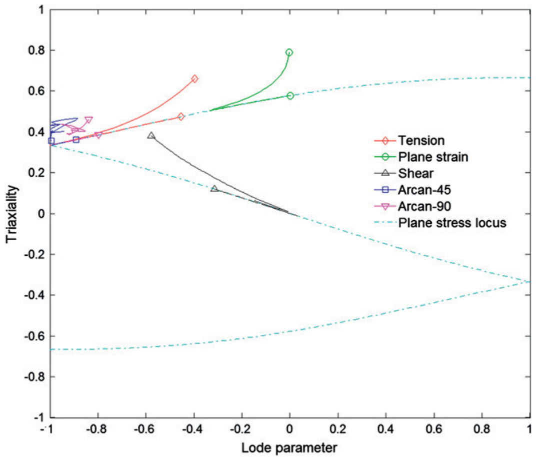

Fig. 15. Relation between stress triaxiality and Lode parameter for plane-stress states (plane-stress locus) and stress paths from shell elements at the surface and solid elements at the centre of the sheet. The dashed lines are from surface shell elements and lie exactly on the plane-stress locus, while solid lines are from centre brick elements. The deviations for the solid elements show that the plane-stress assumption is not fulfilled at the centre of the sheet.

The average stress triaxiality, σ_{avg}^*, obtained with the DIC and FE analyses (see Table 4) is not considerably affected by the deviations found in the $\bar{\varepsilon}$–σ^* curves. In agreement with the preceding discussion, the average Lode parameter, μ_{avg}, exhibits more significant discrepancies, in particular for the uniaxial tension test and the Arcan-90 test.

An interesting observation is that while the FE models of the tension and shear tests exhibit a very close fit to the experimental data in form of the global F–u curves, they display some deviation in terms of the local ε_1–ε_2 and $\bar{\varepsilon}$–σ^* curves compared to data from the DIC analyses. For the FE simulation of the plane-strain tension test the opposite trend is seen. Looking at the ε_1–ε_2 curves for the tension and shear tests in Fig. 13, the deviations in the FE values arise in the last stages of the straining at a time after necking has occurred in the tests.

In order to investigate how the equivalent strain $\bar{\varepsilon}$ and the stress-state parameters σ^* and μ vary through the thickness, values from the shell elements at the surface and the brick elements in the centre of sheet material are compared, see Fig. 14. In general the equivalent strain at fracture, $\bar{\varepsilon}_f$, is 5–10% higher in the brick elements at the centre than in the corresponding shell elements at the surface. The FE model of the shear test is an exception, since here the shell element exhibits approximately 5% higher equivalent strain at fracture than the corresponding brick element. The deviations in μ between the shell and brick elements are smaller than the deviations in σ^*, as shown in Fig. 14. This is possible as the centre brick elements are not subject to the plane-stress condition. Fig. 15 shows how the stress paths in the brick elements deviate from the theoretical plane-stress locus in the σ^*–μ space, while the stress paths from the shell elements lie exactly on the locus. The average values of σ^* and μ do not deviate much in the brick and shell elements in most analyses, as shown in Table 4. The largest differences in σ_{avg}^* and μ_{avg} between the shell and brick values are apparent in the simulation of the shear test, where the deviations are 0.13 and 0.17, respectively. The analytically derived initial values of the stress triaxiality, σ_0^*, and the Lode parameter, μ_0, are summarized in Table 4. These values are based on a plane-stress assumption, and can adequately be compared with the average values σ_{avg}^* and μ_{avg} from the DIC analyses and the shell elements on the surface. The analytical values for the shear test are in good agreement with the values from the DIC and FE analyses, while the analytical values for the tension test are somewhat low. The analytical values for the plane-strain tension test deviate significantly from the values obtained in the DIC and FE analyses. From the FE model it was seen that the stress state at the centre of the specimen is $\boldsymbol{\sigma} = \sigma_{XX}\mathbf{e}_X \otimes \mathbf{e}_X + A\sigma_{XX}\mathbf{e}_Y \otimes \mathbf{e}_Y$ with $A \approx 0.4$ rather than the assumed $A = 0.5$. Using this correction, the resulting analytical values are $\sigma_0^* \approx 0.54$ and $\mu_0 \approx -0.20$ which are in very good agreement with the values found in the DIC and FE analyses.

Mohr and Ebnoether (2009) studied the fracture behaviour of a martensitic boron steel under plane-stress conditions. They found a distinct peak in $\bar{\varepsilon}_f = \bar{\varepsilon}_f(\sigma^*)$ for $\sigma^* \approx 0.4$, and a rather large dispersion in $\bar{\varepsilon}_f$ in the range of stress triaxiality studied ($0 \le \sigma^* \le 0.67$). In a study conducted by Bai et al. (2009), a 1045 steel displayed the same kind of peak in the ductility for $\sigma^* \approx 0.4$. In the same study, it was found that DH36 steel did not show this behaviour, but rather a decreasing ductility with increasing stress triaxiality. The former result in the study of Bai et al. (2009) is in accordance with the results from Hancock and Brown (1983), who investigated the fracture properties of two grades of a plain carbon steel. The fracture strain as a function of average stress triaxiality, $\bar{\varepsilon}_f = \bar{\varepsilon}_f(\sigma_{avg}^*)$, is shown in Fig. 16 for the Docol 600DL sheet material used in this study. The average stress triaxiality is based on the FE simulations and both the fracture strains at the surface and in the centre of the sheet are presented. It is evident that the material

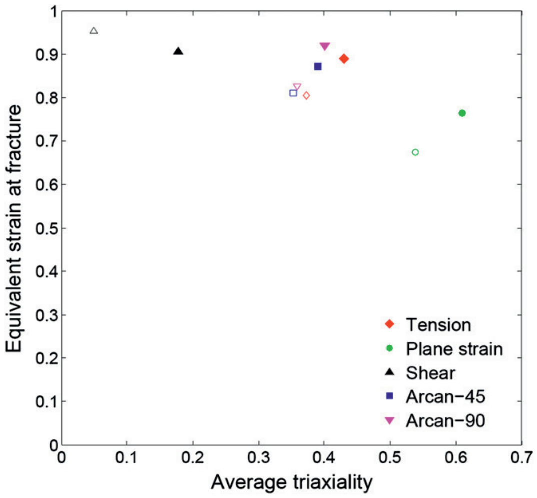

Fig. 16. Equivalent strain at fracture versus average stress triaxiality, $\bar{\varepsilon}_{\mathrm{f}} = \bar{\varepsilon}_{\mathrm{f}}(\sigma^{*}_{\mathrm{avg}})$, based on FE simulations. Filled symbols are for the centre of the sheet, while open symbols are for surface elements.

exhibits only moderate variations of ductility within the investigated range of stress triaxiality. It is further noted that, in general, the equivalent strain is larger and the average stress triaxiality higher in the centre of the sheet than at the surface, and it is thus reasonable to assume that the fracture process started at the centre. This is in accordance with the findings of Dunand and Mohr (2010) for a TRIP steel sheet. In this study, an exception from this phenomenon is the shear test in which the equivalent strain is largest at the surface, while the stress triaxiality is highest in the centre of the sheet. If the fracture strain at the centre is considered, the equivalent strain to fracture seems to be about the same for all tests, except the plane-strain tension test which exhibits somewhat lower ductility. There might even be a weak tendency towards a somewhat higher ductility at a stress triaxiality around 0.4 as found in the abovementioned studies. Considering instead the surface of the sheet, there is a nearly linear increase in the equivalent strain at fracture with decreasing average stress triaxiality. The results from the surface give generally a conservative estimate on the ductility of the material, if we assumed that the fracture occurs in the centre of the sheet. If the sheet material were to be modelled with plane-stress shell elements, which is indeed often the case, the fracture criterion should be based on the equivalent fracture strain at the surface. If solid elements were used, it would be more appropriate to determine the fracture criterion from the equivalent fracture strain at the centre.

It is important to realize that two spatial discretizations are applied to obtain the fracture characteristics of the steel sheet. In both the DIC and the FE analyses, the element size determines the resolution of the strain gradient occurring as the strain localizes before final fracture. Since both methods adopt linear interpolation, the relative resolution depends only on the mesh size. It follows that the resulting fracture locus (as shown in Fig. 16) depends on the element size used to determine the strain fields. A coarse grid will underestimate the fracture strain and lead to conservative estimates. However, since the degree of localization may well vary between the different specimen geometries, it is not certain that the fracture locus is equally conservative for all levels of stress triaxiality. It was for instance noted that the strain field was extremely localized in the shear test, which would tend to make the measured fracture strain more conservative for this loading case. It is important to keep the discretization issue in mind when interpreting fracture data from experiments. The DIC analysis is, however, limited in the way that a smaller element size gives increasing amount of noise in the measured displacement field (Fagerholt et al., submitted for publication). This should therefore be considered when planning the experiments and making the finite element models. By reducing the camera field of view, the DIC element size (in mm) can be reduced to the desired size. In this study, the characteristic element size was about the same in the DIC and FE analyses of the plane-strain tension test, while for the shear test the element size was about twice as large in the DIC analysis. These were the two extreme cases. Ideally one should aspire to use the same element size in the DIC algorithm as in the FEM analysis. In implicit FEA also the time discretization is an issue, in the way that too large increments delay the necking process. However, it should be noted that as long as the simulated time at fracture in the FE models is determined by the effective logarithmic strain at fracture from the DIC recording, rather than a displacement measure, see Section 6.4, the parameters σ^{*}, μ and $\bar{\varepsilon}$ from the FEA are not significantly affected by the element size. The only exception is the fracture strain from the centre of the FE models which must be considered as conservative. A simulation of the uniaxial tension test with 32 elements through the thickness and proportionally decreased in-plane element size resulted in a fracture strain 3.7% higher at the centre element.

8. Conclusions

Experiments have been carried out using five different specimen geometries to characterize the fracture characteristics of a cold-rolled, low-strength, high-hardening steel sheet (Docol 600DL). The tests ranged from plane-strain tension tests to shear tests, covering a domain of stress triaxiality from about 2/3 to zero. The fracture characteristics were obtained using optical field measurements and finite element simulations in combinations with the mechanical testing. A novel method for derivation of the stress triaxiality and the Lode parameter on the surface of the specimen based on DIC measurements was proposed, assuming a Levy-Mises material. In the range of stress states investigated, only moderate variations in the fracture strain were found. In general, the fracture process is likely to initiate at the centre of the specimens where the equivalent strain is larger and the average stress triaxiality is higher than at the surface. For the shear test it was not possible to determine whether the fracture initiates at the surface where the strains are larger or in the centre where the triaxiality is higher.

Acknowledgement

The financial support of this work from the Structural Impact Laboratory (SIMLab), Centre for Research-based Innovation (CRI) at the Norwegian University of Science and Technology (NTNU), is gratefully acknowledged. Thanks are also given to MSc. Torstein Kjøs for thorough work done during the experimental program.

References

Arcan, M., Hashin, Z., Voloshin, A., 1978. A method to produce uniform plane-stress states with applications to fiber-reinforced materials. Exp. Mech. 18, 141–146.
Bai, Y., Teng, X., Wierzbicki, T., 2009. On the application of stress triaxiality formula for plane strain fracture testing. J. Eng. Mater. Technol. 131, 021002.
Bai, Y., Wierzbicki, T., 2008. A new model of metal plasticity and fracture with pressure and Lode dependence. Int. J. Plasticity 24, 1071–1096.
Bao, Y., 2003. Prediction of ductile crack formation in uncracked bodies. PhD thesis, Massachusetts Institute of Technology.
Bao, Y., Wierzbicki, T., 2004a. A comparable study on various ductile crack formation criteria. J. Eng. Mater. Technol. 126, 314–324.

Bao, Y., Wierzbicki, T., 2004b. On fracture locus in the equivalent strain and stress triaxiality space. Int. J. Mech. Sci. 46, 81–98.

Barsoum, I., Faleskog, J., 2007. Rupture mechanisms in combined tension and shear – experiments. Int. J. Solids Struct. 44, 1768–1786 (2.2).

Belytschko, T., Liu, W.K., Moran, B., 2000. Nonlinear Finite Elements for Continua and Structures. John Wiley & Sons, Ltd, Chichester.

Besnard, G., Hild, F., Roux, S., 2006. "Finite-element" displacement fields analysis from digital images: application to Portevin–Le Châtelier bands. Exp. Mech. 46, 789–803.

Børvik, T., Hopperstad, O.S., Berstad, T., 2003. On the influence of stress triaxiality and strain rate on the behaviour of a structural steel. Part II. Numerical study. Eur. J. Mech. A Solids 22, 15–32.

Børvik, T., Hopperstad, O.S., Berstad, T., Langseth, M., 2001. A computational model of viscoplasticity and ductile damage for impact and penetration. Eur. J. Mech. A Solids 20, 685–712.

Bridgman, P.W., 1952. Studies in Large Plastic Flow and Fracture: With Special Emphasis on the Effects of Hydrostatic Pressure. Harvard Univ. Press, Cambridge, Mass.

Cook, R.D., Malkus, D.S., Plesha, M.E., Witt, R.J., 2002. Concepts and Applications of Finite Element Analysis. John Wiley & Sons.

Curtze, S., 2009. Deformation behavior of TRIP and DP steels in tension at different temperatures over a wide range of strain rates. Mater. Sci. Eng.: A 507, 124–131.

Dunand, M., Mohr, D., 2010. Hybrid experimental-numerical analysis of basic ductile fracture experiments for sheet metals. Int. J. Solids Struct. 47, 1130–1143.

El-Magd, E., Abouridouane, M., 2006. Characterization, modelling and simulation of deformation and fracture behaviour of the light-weight wrought alloys under high strain rate loading. Int. J. Impact Eng. 32, 741–758.

Eriksson, M., Lademo, O.-G., Hopperstad, O.S., 2006. Development and use of in-plane shear tests to identify ductile failure parameters of aluminium alloys. In: Proceedings of 9th International Conference on Material Forming (ESAFORM-2006), April 26–28, 2006, Glasgow, pp. 331–334.

Fagerholt, E., Børvik, T., Hopperstad, O.S. Detection and handling of crack propagation in ductile materials using two-dimensional digital image correlation (2D-DIC). Exp. Mech., submitted for publication.

Gao, X., Kim, J., 2006. Modeling of ductile fracture: significance of void coalescence. Int. J. Solids Struct. 43, 17.

Hancock, J.W., Brown, D.K., 1983. On the role of strain and stress state in ductile failure. J. Mech. Phys. Solids 31, 1–24.

Hancock, J.W., Mackenzie, A.C., 1976. On the mechanisms of ductile failure in high-strength steels subjected to multi-axial stress-states. J. Mech. Phys. Solids 24, 147–169.

Hill, R., 1950. The Mathematical Theory of Plasticity. Oxford Science Publications.

Hosford, W.F., 1972. A general isotropic yield criterion. J. Appl. Mech. 39, 607–609.

Johnson, G.R., Cook, W.H., 1985. Fracture characteristics of three metals subjected to various strains, strain rates, temperatures and pressures. Eng. Fract. Mech. 21, 31–48.

Kim, J., Zhang, G., Gao, X., 2007. Modeling of ductile fracture: application of the mechanism-based concepts. Int. J. Solids Struct. 44, 1844–1862.

Lode, W., 1926. Versuche fiber den Einfluß der mittleren Hauptspannung auf das Fließen der Metalle Eisen, Kupfer und Nickel. Z. Physik 36, 913–939.

LSTC, 2007. LS-DYNA Keyword User's Manual, Version 971. Livermore Software Technology Corporation.

McClintock, F.A., 1968. Criterion for ductile fracture by growth of holes. J. Appl. Mech. 35, 363–371.

Mohr, D., Ebnoether, F., 2009. Plasticity and fracture of martensitic boron steel under plane stress conditions. Int. J. Solids Struct. 46, 3535–3547.

Mohr, D., Oswald, M., 2008. A new experimental technique for the multi-axial testing of advanced high strength steel sheets. Exp. Mech. 48, 65–77.

Rice, J.R., Tracey, D.M., 1969. On the ductile enlargement of voids in triaxial stress fields. J. Mech. Phys. Solids 17, 201–217.

SSAB, 2009. Docol DP/DL Cold Reduced Dual Phase Steels. SSAB Swedish Steel Ltd. http://www.ssab.com/Global/DOCOL/datasheets_docol/en/201_Docol%20DP,%20DL.pdf. (accessed 10.05.10).

Tarigopula, V., Langseth, M., Hopperstad, O.S., Clausen, A.H., 2006. Axial crushing of thin-walled high-strength steel sections. Int. J. Impact Eng. 32, 847–882.

Voloshin, A., Arcan, M., 1980. Failure of unidirectional fiber-reinforced materials—new methodology and results. Exp. Mech. 20, 280–284.

Wierzbicki, T., Bao, Y., Lee, Y.-W., Bai, Y., 2005. Calibration and evaluation of seven fracture models. Int. J. Mech. Sci. 47, 719–743.

Wilkins, M.L., Streit, R.D., Reaugh, J.E., 1980. Cumulative-Strain-Damage Model of Ductile Fracture: Simulation and Prediction of Engineering Fracture Tests. Technical Report UCRL-53058. Lawrence Livermore National Laboratory.

Part II

G. Gruben, D. Vysochinskiy, T. Coudert, A. Reyes and O.-G. Lademo

Determination of ductile fracture parameters of a dual-phase steel by optical measurements

Submitted for possible journal publication

Determination of ductile fracture parameters of a dual-phase steel by optical measurements

G. Gruben[a,*] , D. Vysochinskiy[a], T. Coudert[b,a], A. Reyes[a] and O.-G.Lademo[b,a]

[a]Structural Impact Laboratory (SIMLab), Centre for Research-based Innovation (CRI) and Department of Structural Engineering, Norwegian University of Science and Technology, Rich. Birkelands vei 1A, NO-7491 Trondheim, Norway

[b]SINTEF Materials and Chemistry, Applied Mechanics and Corrosion, NO-7465 Trondheim, Norway

ABSTRACT: Marciniak-Kuczynski and Nakajima tests of the dual-phase steel Docol 600DL have been carried out for a range of stress states spanning from uniaxial tension to equi-biaxial tension. The deformation histories of the specimens have been recorded by digital images, and the displacement and strain fields have been determined by post-processing the images with digital image correlation software. The stress triaxiality, Lode parameter and the equivalent strain are calculated from the optical measurements, and presented as parameters to describe the fracture characteristics of the material. It is found that the material displays a significantly lower ductility in plane-strain tension than in uniaxial tension and equi-biaxial tension. Fractographs of selected specimens reveal that fracture is due to dilatational growth and coalescence of voids that occur in localized areas governed by shear-band instability. A verification of the method used in deriving the stress triaxiality and the Lode parameter has been conducted.

KEY WORDS: *Digital image correlation, dual-phase steel, ductile fracture, Lode parameter, stress triaxiality*

Introduction

Ductile fracture is controlled by nucleation, growth and coalescence of microvoids as explained by McClintock [1] and Rice and Tracey [2]. Increased hydrostatic pressure tends to decrease the rate of void growth, and so increase the ductility. The ductility can

---

[*] Corresponding author. Tel. +47-73-59-46-87

Email address: gaute.gruben@ntnu.no (G. Gruben) be expressed by the equivalent strain at fracture, $\bar{\varepsilon}_f = \bar{\varepsilon}(t_f)$, where t_f is the time at fracture and $\bar{\varepsilon}$ is the equivalent strain, defined as $\bar{\varepsilon} = \int_0^t \sqrt{2/3 D_{ij} D_{ij}}\, dt$ where D_{ij} is the rate-of-deformation tensor. A commonly used parameter to describe the hydrostatic stress state is the stress triaxiality, σ^*, defined as

$$\sigma^* = \frac{\sigma_h}{\bar{\sigma}} \tag{1}$$

where $\sigma_h = \sigma_{ii}/3$ is the hydrostatic stress and $\bar{\sigma} = \sqrt{3 s_{ij} s_{ij}/2}$ is the von Mises equivalent stress with σ_{ii} as the Cauchy stress tensor and s_{ij} as the stress deviator. Recent findings from macro-scale experiments e.g. [3-5] indicate that the deviatoric stress state also influences the ductility in the range of low stress triaxiality σ^*. The deviatoric stress state can be expressed by the Lode parameter, μ, defined as [6]

$$\mu = \frac{2\sigma_{II} - \sigma_I - \sigma_{III}}{\sigma_I - \sigma_{III}} \tag{2}$$

where σ_i, $i = I, II, III$ are the principal stresses ordered so that $\sigma_I \geq \sigma_{II} \geq \sigma_{III}$.

The Digital Image Correlation (DIC) technique [7] is a powerful tool for determining material properties from experiments. DIC was applied by Wu et al. [8] to estimate the accumulated damage in a 15-5PH steel during plastic deformation. Kirugulige and Tippur [9] used DIC to determine the stress intensity factors of a foam material under dynamic loading, while Luo and Wang [10] used DIC in determining the stress intensity factors as well as the J-integral from compact tension shear specimens made of 2024-O aluminium. However, stress and strain histories from material tests are traditionally found from numerical simulations of the tests, e.g. [3, 11-15], or analytical models, e.g. [16-17].

Gruben et al. [18] carried out experiments in the low range of stress triaxiality on steel sheets of Docol 600DL. The five test series included uniaxial tension, plane-strain tension and in-plane shear as well as two types of modified Arcan tests. In that study a novel method for experimental determination of σ^* and μ based on optical measurements of the displacement fields was presented and applied on selected tests. The method was used to derive σ^* and μ as well as the equivalent strain, $\bar{\varepsilon}$. In addition, σ^*, μ and $\bar{\varepsilon}$ were derived from finite element simulations, and it was found that the average values of the stress state parameters, σ^*_{avg}, μ_{avg}, as well as the fracture strain, $\bar{\varepsilon}_f$, extracted by two approaches were in good agreement. It was further found from the finite element simulations that the equivalent strain and the stress triaxiality were larger in the centre than on the surface of the specimen in four out of five tests, and so fracture was more likely to initiate in the centre of the specimen in these tests. As the experimental method is restricted to the surface of the specimen, it was concluded that use of surface displacement fields to determine the fracture strain could be considered a conservative approach for these tests.

In this study, the experimental technique presented in [18] is applied to Marciniak-Kuczynski [19] and Nakajima [20] formability tests conducted on specimens made of Docol 600DL material from the same batch as used in [18], and thus expanding the experimental database for this material. Further, the measuring technique is verified against finite element models utilized in [18], and the fracture surfaces of selected test specimens are studied in a scanning electron microscope (SEM). It is concluded that the ductility of the material is significantly lower for (in-plane) plane-strain tension than for uniaxial tension or equi-biaxial tension, and that fracture is governed by nucleation, growth and coalescence of microvoids that occur in shear bands.

Experiments

Material

The material is a dual-phase steel delivered as 2 mm thick sheets from Swedish Steel AB (SSAB). It can be characterized as a low-strength, high-hardening material where the nominal yield stress is reported from the manufacturer to be in the range 280-360 MPa and the nominal ultimate stress is reported to be between 600 MPa and 700 MPa [21]. Through heat treatment the material is given a two-phase structure of ferrite and martensite, in which the ferrite gives the formability features, while the martensite proportion determines the strength. The nominal chemical composition of the material is given in Table 1. A previous study has shown that the material exhibits a nearly isotropic behaviour in terms of work hardening and plastic flow [18].

Table 1 Chemical composition of Docol 600DL (in wt %) [21].

C	Si	Mn	P	S	Al_{tot}
0.10	0.40	1.50	0.010	0.002	0.040

Experimental set-up and optical measuring procedure

The Marciniak-Kuczynski and Nakajima experiments were carried out in a Zwick/Roell BUP 600 test machine as depicted in Figure 1(A). All experiments were carried out under quasi-static loading conditions and displacement control. The punch velocity was 0.3 mm/s, and two duplicate tests were performed for each specimen geometry. For both tests, a sheet of the material was clamped between a die and a blank holder with a clamping force. The clamping force can be altered, and in order to obtain fracture in the fracture zone and not in the clamping, some tests were carried out to determine a reasonable clamping force for the tests in this study. This might be different for a different material and sheet thickness. Further details about the clamping force can be found in [22].

Apart from the test set-up and the use of a three-dimensional DIC, the approach in collecting data from the optical measurements is the same as in [18]. The main aspects of the approach are repeated here for convenience. Before testing, one side of the specimen was spray-painted by a combination of black and white paint, obtaining a high-contrast speckle pattern to improve the optical measurements. Two Prosilica GC2450 cameras equipped with 50 mm Nikon lenses were attached above the specimens as shown in Figure 1(A). The cameras were recording the experiments with a framing rate of 2 Hz. A zone of each image from the gauge area, Figure 1(B), were post-processed by the three-dimensional DIC software 7D [23] following the coordinates of nodes, initially lying in a square pattern with 0.77 mm distance between them, see Figure 1(C). Triangular elements were used in deriving the effective logarithmic strain field in the gauge area of each test in the last frame before fracture. The effective logarithmic strain is here defined as

$$\varepsilon_e = \sqrt{\frac{2}{3}\left(\varepsilon_1^2 + \varepsilon_2^2 + \varepsilon_Z^2\right)} \tag{3}$$

where ε_i, $i = 1,2$ are the in-plane principal strains, found by solving the eigenvalue problem for the right Green deformation tensor (see [18] for details), and ε_Z is the through-thickness strain. Assuming incompressibility and that the through-thickness shear strains are negligible (i.e. the thickness direction is assumed to be a principal direction), we have that $\varepsilon_Z = -(\varepsilon_1 + \varepsilon_2)$.

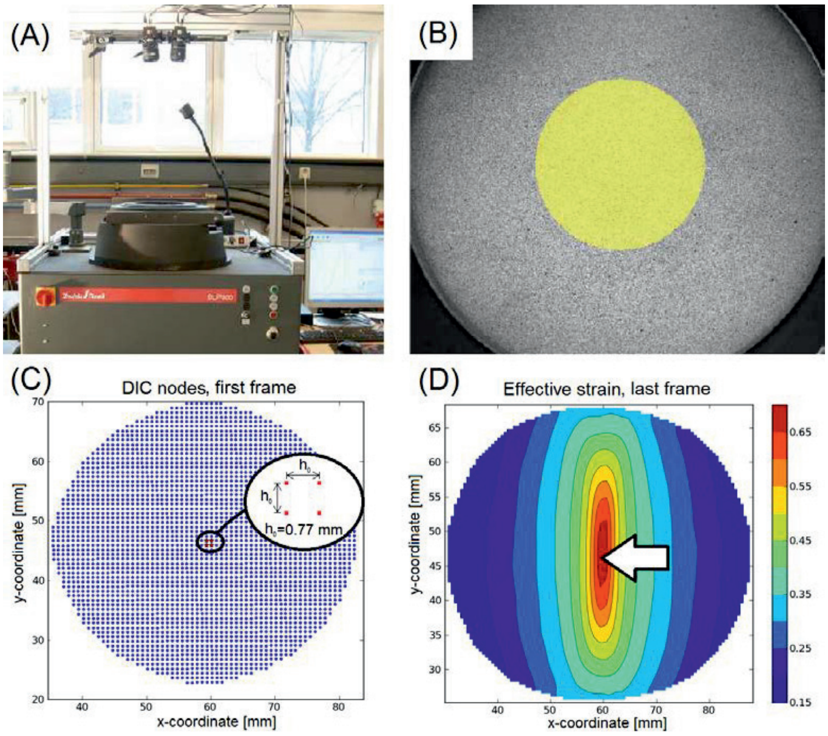

Figure 1 (A) The Zwick/Roell BUP 600 test machine with two cameras for DIC measurements and (B) specimen with speckle pattern and zone (in yellow) for DIC measurement [22]. (C) DIC nodes in the first image. The nodes constituting the element used for collecting fracture parameters are marked. (D) Effective strain in the last frame before fracture. The arrow points at the element used for collecting fracture data.

It was generally not possible to pinpoint the exact position of fracture initiation within the gauge area. The point of the largest effective logarithmic strain in the last image before fracture was thus chosen as the point for collecting the deformation data; this is illustrated in Figure 1(D). The four nodes enclosing the point of fracture initiation cf. Figure 1(C), constituted the element used in calculating the fracture parameters. It was found that warping of this four-node element was negligible in all the tests, i.e. the out-of-plane displacement was neglected. Using a total Lagrangian formulation, the displacement gradient was evaluated at the centre point of the element from the displacement histories of the nodes. Further, the in-plane Green strain tensor, $\mathbf{E}$, was calculated and the temporal increment of the in-plane Green strain tensor, $\Delta\mathbf{E}$, was derived. The push-forward operation was conducted on $\Delta\mathbf{E}$ to obtain an objective in-plane strain-increment tensor. The principal in-plane strain increments, $(\Delta\varepsilon_1, \Delta\varepsilon_2)$, were then calculated by solving the eigenvalue problem for the objective in-plane strain-increment tensor (see [18] for details). From $(\Delta\varepsilon_1, \Delta\varepsilon_2)$ the stress triaxiality and the equivalent strain were calculated under the assumption of a Levy-Mises material. These parameters are expressed as

$$\sigma^* = \frac{\sqrt{3}}{3}\frac{\beta+1}{\sqrt{\beta^2+\beta+1}} \tag{4}$$

$$\bar{\varepsilon} = \sum \Delta\bar{\varepsilon} = \sum\sqrt{\frac{2}{3}(\Delta\varepsilon_1^2 + \Delta\varepsilon_2^2 + \Delta\varepsilon_Z^2)} \tag{5}$$

where

$$\Delta\varepsilon_1 > 0, \qquad \beta = \frac{\Delta\varepsilon_2}{\Delta\varepsilon_1} \ \left(-\infty < \beta \le 1\right), \qquad \Delta\varepsilon_Z = -(\Delta\varepsilon_1 + \Delta\varepsilon_2) \tag{6}$$

The last relation in Equation (6) is found by assuming incompressibility and that the thickness direction is a principal direction. Filtering was necessary to calculate σ^* and $\bar{\varepsilon}$, and the same procedure as described in [18] was applied. Thus, C^2 continuous cubic splines were fitted by the least squares method to the histories of the nodal displacements. The initial and final displacements were used as boundary conditions on the smoothed curves. In the tests used in this study, 12 splines were found to be suitable. For the history curve of σ^*, the same filtering as used in [18] was applied for visualization purposes. When calculating the logarithmic strains, $\varepsilon_1, \varepsilon_2, \varepsilon_Z$ and the effective logarithmic strain ε_e, filtering was not used. For further details regarding the method, the reader is referred to [18].

Marciniak-Kuczynski set-up

The Marciniak-Kuczynski (M-K) test set-up is illustrated in Figure 2(A). The test specimens are rectangular plates with a length of 205 mm and varying widths of 155 mm, 160 mm, 165 mm and 205 mm, see Figure 2(B). The specimens were labelled MK-XXX-Y, where XXX is the width of the specimen, and Y=1,2 is the duplicate number. A centring device, cf. Figure 2(C), was used to lock the position of the specimen at the centre of the punch. To ensure that no tractions from the punch acted on the centre zone of the specimen, a friction sheet with the same width and length as the specimen and with a centred hole of 40 mm diameter was placed between the punch and the specimen. The friction sheet was 1.4 mm thick and made of a steel material with yield and ultimate stress around 185 MPa and 375 MPa, respectively. The friction sheet was sand blasted on the side facing the specimen to increase the friction between the specimen and the friction sheet. This ensured that the friction sheet deformed together with the specimen. In order to reduce the strains in the specimen around the punch edges and make sure that fracture would occur at the centre of the specimen [24], a 0.1 mm thick layer of PTFE (Teflon) was placed between the punch and the friction plate, and the punch was lubricated with grease.

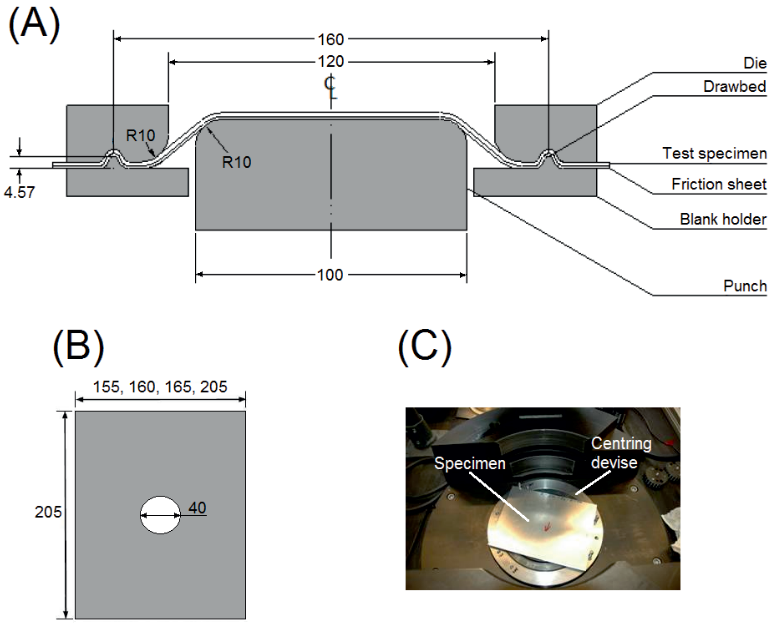

Figure 2 Marciniak-Kuczynski test set up (measurements in mm). (A) Sketch of test set-up, and (B) specimen dimensions (the hole is only for the friction sheet). (C) Centring devise used for the specimens.

Nakajima set-up

The Nakajima test specimens consist of circular disks with eight various cut-outs. The specimens were labelled NK-X-Y, where X=1,2,..,8 is the test number and Y=1,2 is the duplicate number. Figure 3(A) displays the specimen geometries. The specimens were cut as illustrated in Figure 3(B) with 3 mm strips still attached to rectangular blanks, thus allowing the use of the same centring device as used in the M-K tests to ensure a proper position of the specimens. The set-up is similar to the M-K test set-up displayed in Figure 2(A), but without the friction sheet. A 0.1 mm thick layer of Teflon was placed between the specimen and the punch to reduce friction. While the M-K test utilize a flat punch as illustrated in Figure 2(A), the Nakajima tests are carried out with a hemispherical punch with a radius of 50 mm.

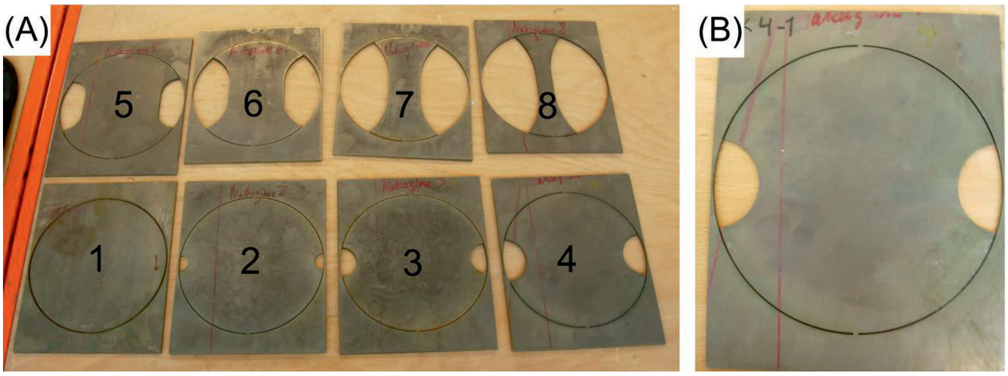

Figure 3 (A) Nakajima test geometries, and (B) close-up of a specimen attached to the rectangular blank [22].

Verification of experimental procedure

The experimental procedure used in extracting the stress triaxiality and the equivalent strain were compared with the more traditional approach using a hybrid experimental-numerical procedure in [18]. The results in terms of average stress triaxiality, cf. Equation (8) below, and fracture strain derived by the two approaches were in good agreement. However, a proper verification of the method was not conducted. As part of this study, a verification of the method has been carried out. In order to do so, the finite element models utilized in [18] have been used. The method was applied on the nodal displacement histories from the finite element simulations. In this way the calculated $\sigma^* - \bar{\varepsilon}$ curve could be compared directly with results extracted from the finite element corresponding to the nodes. Figure 4 displays the discretizations of the five tests used in the verification. Here Figure 4(A) gives the uniaxial tension test, while (B) shows the plane-strain tension test, (C) gives the in-plane shear test and (D) displays the modified Arcan test. In the modified Arcan tests the β angle in Figure 4(D) was set to $45°$ and $90°$. The tests covers a range of initial stress triaxiality from simple shear $(\sigma^* = 0)$ to plane-strain tension $(\sigma^* \approx 0.58)$. For further details regarding the finite element simulations the reader is referred to [18]. The principal stress histories from the elements at the surface corresponding to the in-plane point of fracture initiation in each test were collected and used in deriving the histories of the stress triaxiality according to

Equation (1). The equivalent strain histories from the same elements were also collected, and the results in terms of $\sigma^* - \bar{\varepsilon}$ curves are shown in Figure 5(A). Additionally, the displacement histories of the corresponding surface nodes were used in calculating $\Delta\varepsilon_1$ and $\Delta\varepsilon_2$. Subsequently, σ^* and $\bar{\varepsilon}$ were calculated from Equations (4) and (5), respectively. In these calculations filtering were not applied since the displacement curves from the finite element analysis were sufficiently smooth. The results in terms of $\sigma^* - \bar{\varepsilon}$ curves are shown in Figure 5(B). As can be seen from Figure 5(A) and (B), the two different approaches are in very good agreement. The Lode parameter is not shown in the verification as there is a unique relation between the Lode parameter and the stress triaxiality in plane stress, see Equation (7) below.

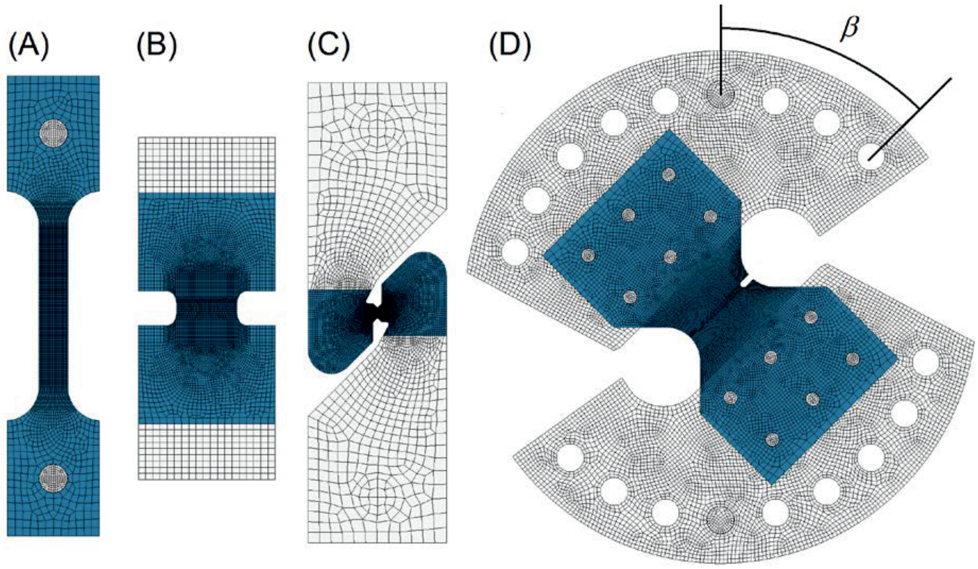

Figure 4 Finite element models used in verification of the experimental procedure [18]. (A) uniaxial tension test, (B) plane-strain tension test, (C) in-plane shear test and (D) modified Arcan test.

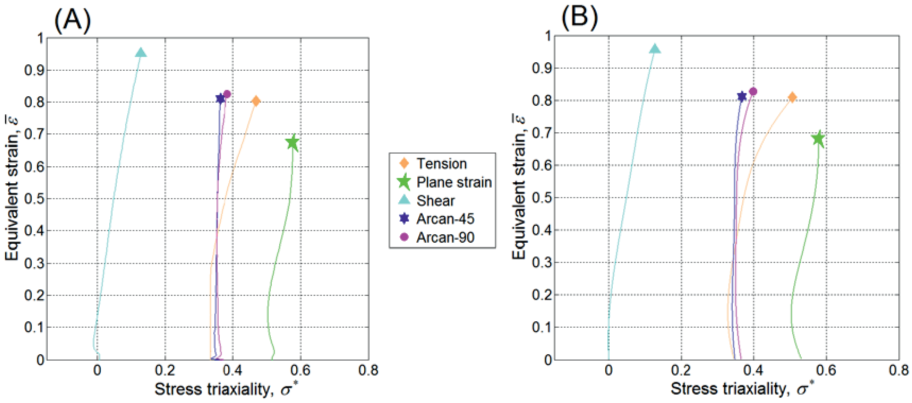

Figure 5 Validation of experimental procedure. (A) $\sigma^* - \bar{\varepsilon}$ curves as collected directly from the integration point in the finite element software, and (B) $\sigma^* - \bar{\varepsilon}$ curves as derived from the nodal displacements and the experimental procedure.

Results

Marciniak-Kuczynski tests

Three of the set-ups are close to plane-strain tension (MK-155, MK-160 and MK-165), while the fourth is close to equi-biaxial tension (MK-205). Two of the test specimens did not fracture (MK-165-2 and MK-205-1), due to premature termination of the test. Figure 6 gives the effective logarithmic strain for the successful tests in the last image before fracture as well as the fractured specimens. The position at which deformation data were collected is indicated by arrows. The results in form of major vs. minor principal logarithmic strains and fracture strain as function of stress triaxiality are shown in Figure 7(A) and (B), respectively. As can be seen in Figure 7(A), the MK-155 and MK-160 tests display very similar histories, while MK-165 starts out with a deformation unlike the other two, but ends up in plane-strain deformation. The MK-205 test is in a deformation state near equi-biaxial tension throughout the whole history. Figure 7(B) shows that the fracture strain differs about 0.05 in the two set-ups where both duplicates were successful. Notably, the test in equi-biaxial tension displays a significantly higher ductility than the other tests.

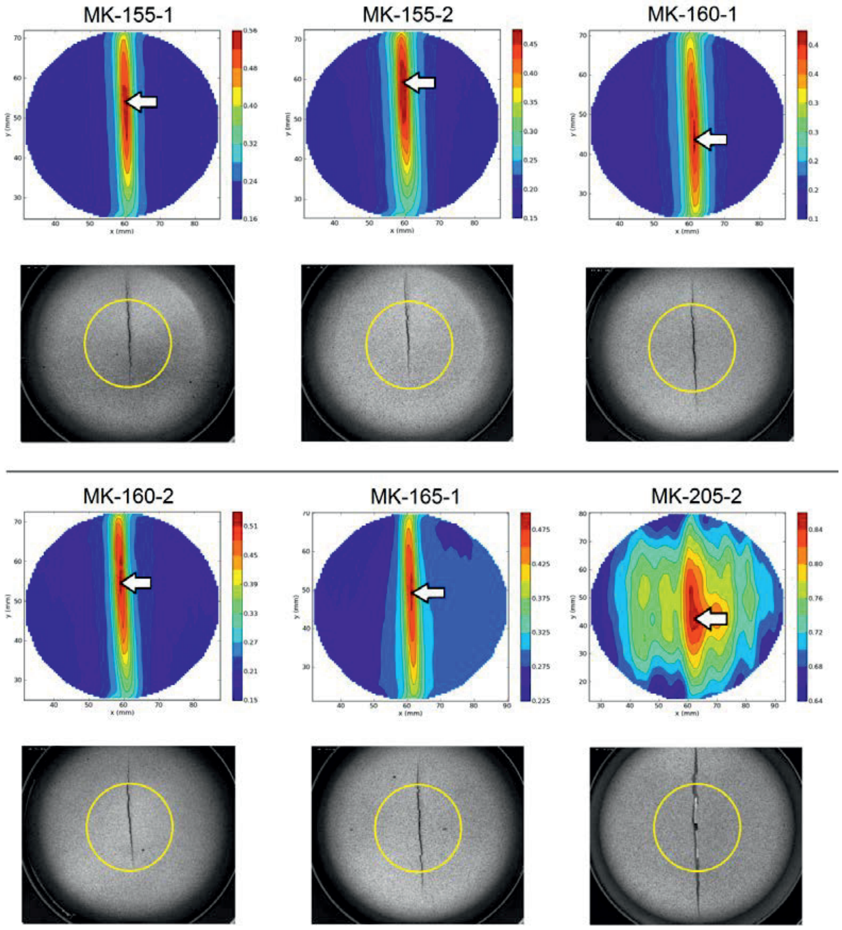

Figure 6 Effective logarithmic strain in the last frame before fracture in the Marciniak-Kuczynski tests, and specimens after fracture. The arrows show where the deformation histories are collected, while the circles display the zones where the DIC measurements were applied.

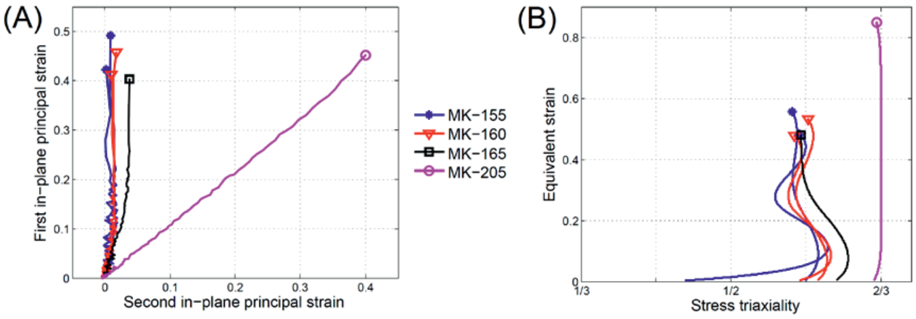

Figure 7 Results from Marciniak-Kuczynski tests. (A) Principal in-plane logarithmic strains and (B) equivalent strain as function of stress triaxiality.

Nakajima tests

The stress state in the Nakajima tests varied between equi-biaxial tension for NK-1 to near uniaxial tension in NK-8. Two of the tests failed (NK-4-1 and NK-4-2) as fracture occurred in the clamping zone rather than in the gauge area. The effective logarithmic strain in the last image before fracture in each successful test is shown in Figure 8. The major vs. minor principal logarithmic strains for all 14 successful tests are given in Figure 9(A). As can be seen, the deformation state is very similar in both duplicate tests for each set-up. All tests except NK-8 (uniaxial tension) start out in equi-biaxial tension before they move into their assumed “natural” stress state when the major principal strain is around 0.035. NK-8 starts out in near plane-strain tension before it moves over to uniaxial tension. Fracture strain versus stress triaxiality for all tests is given in Figure 9(B), which also shows that the fracture strain between duplicates is consistent for four of the specimen geometries. On the contrary, in NK-1, NK-2 (equi-biaxial tension) and NK-6 (plane-strain tension) tests the difference in fracture strain between the duplicates is somewhat larger, see Figure 9(B). As in the M-K tests, high ductility in equi-biaxial tension and low ductility in plane-strain tension is observed.

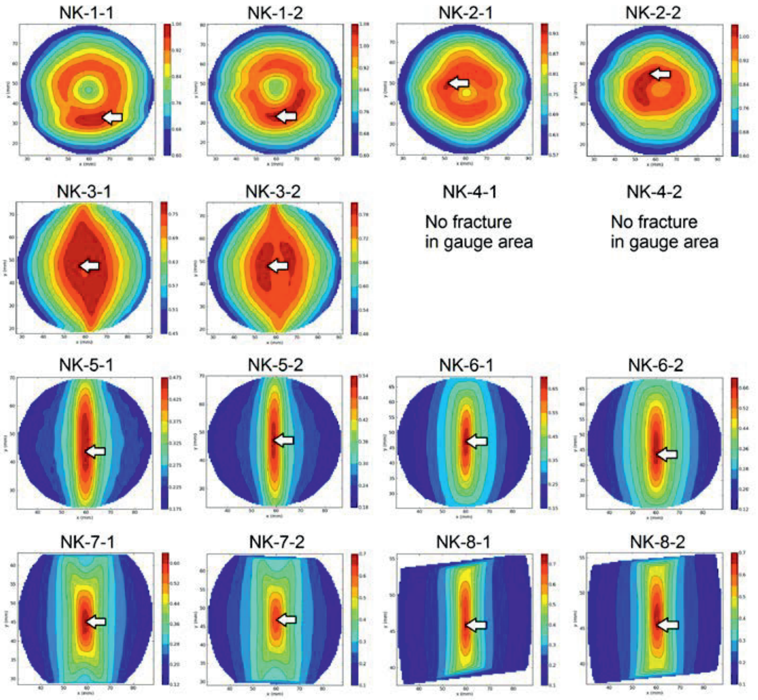

Figure 8 Effective logarithmic strain in the last image before fracture in the Nakajima tests. The arrows show where the deformation values are collected.

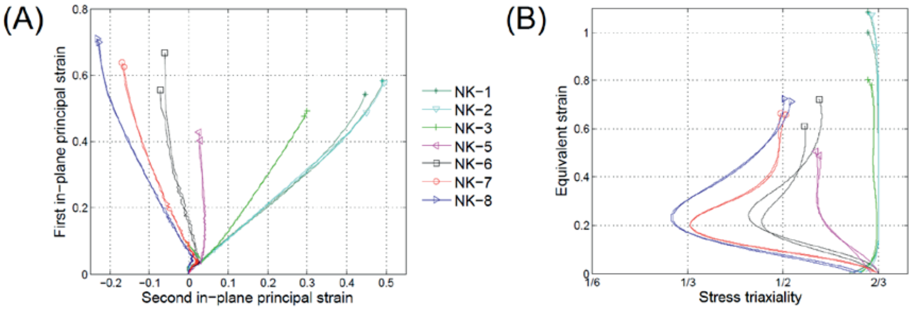

Figure 9 Results from Nakajima tests. (A) Principal in-plane logarithmic strains, and (B) equivalent strain as function of stress triaxiality.

Instability and fracture

Instability and fracture of the material in the investigated range of stress-states is examined by selecting a few tests that are subject to a closer study. The NK-8-2 test represents uniaxial tension, while the NK-5-1 and MK-155-1 tests represent plane-strain tension, and the NK-1-1 and MK-205-2 tests represent equi-biaxial tension. As indicated in Figure 10(A), the Nakajima tests in uniaxial tension display a diffuse neck and a through-thickness neck before fracture. Figure 10(B) and (D) show that the Nakajima and M-K tests in plane-strain tension display a through-thickness neck, while Figure 10(C) and (E) show that the equi-biaxial Nakajima and M-K tests do not exhibit necking instability before fracture. Figure 11(A) displays the effective strain as function of time, $\varepsilon_e(t)$, taken from the spatial point of fracture initiation, see Figure 6 and Figure 8. The time derivative of the effective strain, $\dot{\varepsilon}_e(t)$, are given in Figure 11(B). As illustrated in Figure 11(A), the NK-1-1 and MK-205-2 tests, which are in equi-biaxial tension, display a gradual increase in the strain-rate. This stems from a nonlinear correlation between the applied displacement and the straining. The necking instability in the NK-8-2, NK-5-1 and MK-205-2 tests can be interpreted as the abrupt change in $\dot{\varepsilon}_e(t)$ displayed in Figure 11(B). Before final failure, shear-band instability occurs in the material in all tests. This phenomenon occurs on a scale which is too small to be captured by the DIC technique with the resolution of the images used in this study. However, shear lips which typically follows shear-band localization, are present in all the fractured specimens. This is exemplified by the specimens displayed in Figure 10. It is noted that the specimens in plane-strain tension display a more rough fracture surface, as illustrated in Figure 10(B) and (D), than the specimens in uniaxial or equi-biaxial tension.

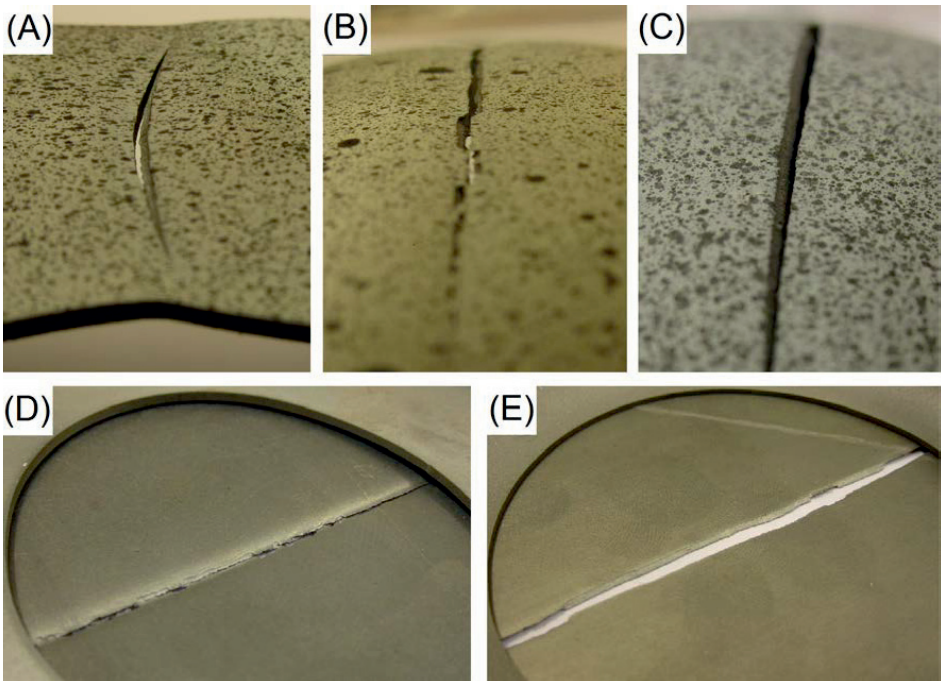

Figure 10 Necking instability and fracture of selected tests. (A) NK-8-2, uniaxial tension, with diffuse and through thickness necking, (B) NK-5-1, plane-strain tension, with through thickness neck, (C), NK-1-1, equi-biaxial tension, and no necking instability, (D) MK-155-1, plane-strain tension, with through-thickness necking and (E) MK-205-2, equi- biaxial tension, with no necking.

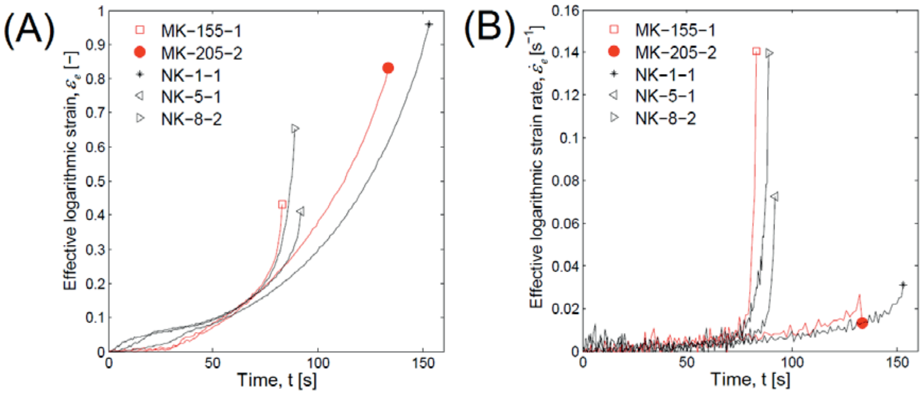

Figure 11 Plots of (A) $\varepsilon_e(t)$ and (B) $\dot{\varepsilon}_e(t)$ curves for selected tests. MK-155-1, NK-5-1 and NK-8-2, display an abrupt change in strain rate due to necking instability, while tests MK-205-2 and NK-1-1 display only moderate change in strain rate.

The fracture surfaces of the five selected tests were further investigated in a scanning electron microscope of type Hitachi SU6600. Figure 12(A-E) displays high magnification fractographs of the fracture initiation point in the Nakajima and M-K tests, while Figure 12(F) displays the fracture surface of the NK-1-1 test at low magnification. It can be seen from Figure 12(A-E) that most of the dimples are small, $< 5\ \mu\text{m}$. This suggests that voids are nucleated at small particles that are closely spaced, and that the voids coalesce before they reach a larger size, leaving a macroscopically smooth surface typical for shear lips [25]. Three larger dimples with visible inclusions marked with an 'i' can be seen in Figure 12(A-B) and (D). Areas with elongated dimples typical for shear fracture can be observed in Figure 12(A-C). Some of these areas are marked with an 's'. An interesting observation in the NK-5-1, NK-1-1 and MK-205-2 tests is a groove located at the centre of the fracture surface. The groove, which is marked with a 'g', is illustrated in Figure 12(F) at low magnification and in Figure 12(B-C) and (E), at higher magnification. The groove might be a result of the concentrated deformation at the locus where the two shear bands meet.

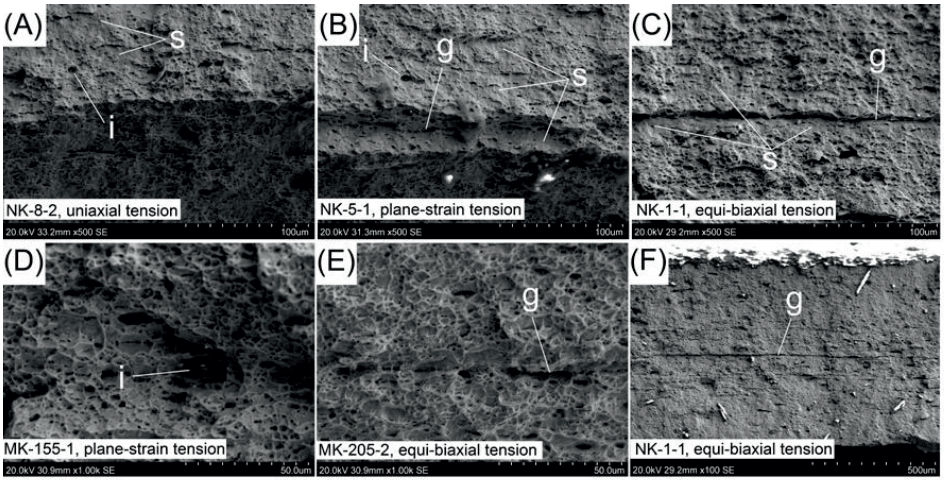

Figure 12 (A-E) High magnification SEM fractographs of selected Nakajima and Marciniak-Kuczynski tests and (F) NK-1-1 at a lower magnification. 's' indicates some typical areas with shear fracture, while 'i' marks inclusions, and 'g' shows grooves found on the surface in three of the tests.

Ductility as function of average hydrostatic and deviatoric stress state

As a complementary stress-state parameter to the stress triaxiality, the Lode parameter, μ, can be used to describe the deviatoric stress state of the material. Assuming von Mises yield function and plane-stress conditions, it can be shown that the Lode parameter can be expressed as a function of stress triaxiality as

$$\mu = \begin{cases} \dfrac{-3}{9(\sigma^*)^2 - 1} \cdot \left(1 - \sqrt{12(\sigma^*)^2 - 27(\sigma^*)^4}\right) & \text{for} \quad \sigma_I = 0, \quad -\tfrac{2}{3} \le \sigma^* \le -\tfrac{1}{3} \\ \sqrt{\dfrac{27(\sigma^*)^2}{4 - 9(\sigma^*)^2}} & \text{for} \quad \sigma_{II} = 0, \quad -\tfrac{1}{3} \le \sigma^* \le 0 \\ -\sqrt{\dfrac{27(\sigma^*)^2}{4 - 9(\sigma^*)^2}} & \text{for} \quad \sigma_{II} = 0, \quad 0 \le \sigma^* \le \tfrac{1}{3} \\ \dfrac{3}{9(\sigma^*)^2 - 1} \cdot \left(1 - \sqrt{12(\sigma^*)^2 - 27(\sigma^*)^4}\right) & \text{for} \quad \sigma_{III} = 0, \quad \tfrac{1}{3} \le \sigma^* \le \tfrac{2}{3} \end{cases} \tag{7}$$

When the material is in a plane-stress condition, the Lode parameter does not provide more information about the stress-state due to the one-to-one relation between the Lode parameter and the stress triaxiality. However, while the change in stress triaxiality is small when going from plane-strain tension $(\sigma^* \approx 0.58)$ to equi-biaxial tension $(\sigma^* \approx 0.67)$ the change in the deviatoric stress state is significant. This is captured by the Lode parameter which is zero in plane-strain tension and unity in equi-biaxial tension. Similarly the Lode parameter clearly distinguishes the uniaxial tension stress state by $\mu = 1$. Figure 7(B) and Figure 9(B) which gives $\bar{\varepsilon}$ as function of σ^* do not display the large change in the deviatoric stress state. In order to explicitly illustrate the effect of both the hydrostatic and deviatoric stress state on the fracture strain, data including the Lode parameter are given in this section and used in the subsequent discussion. Here, the average values of the stress triaxiality and the Lode parameter are used rather than the history curves. The average values are calculated by an integral expression over the equivalent strain as

$$\sigma^*_{\text{avg}} = \frac{1}{\bar{\varepsilon}_f} \int_0^{\bar{\varepsilon}_f} \sigma^*(\bar{\varepsilon}) d\bar{\varepsilon}, \qquad \mu_{\text{avg}} = \frac{1}{\bar{\varepsilon}_f} \int_0^{\bar{\varepsilon}_f} \mu(\bar{\varepsilon}) d\bar{\varepsilon} \tag{8}$$

In order to facilitate the comparison of data from the different tests, the average values of the two duplicates for each test is presented. In the two M-K tests where only one duplicate was successful, the value from this test is presented. The results are compared to the data from [18] and given in Figure 13 and Table 2. Figure 13(A) displays the fracture strain as function of average stress triaxiality, while Figure 13(B) gives the fracture strain as function of average Lode parameter. The plane-stress locus as defined by Equation (7), is compared to the parameters $(\sigma^*_{\text{avg}}, \mu_{\text{avg}})$ from the 16 tests in Figure 13(C). It is noted that the deviation from the plane-stress locus in Figure 13(C), most notably observed for the modified Arcan tests [18], stems from the averaging defined by Equation (8).

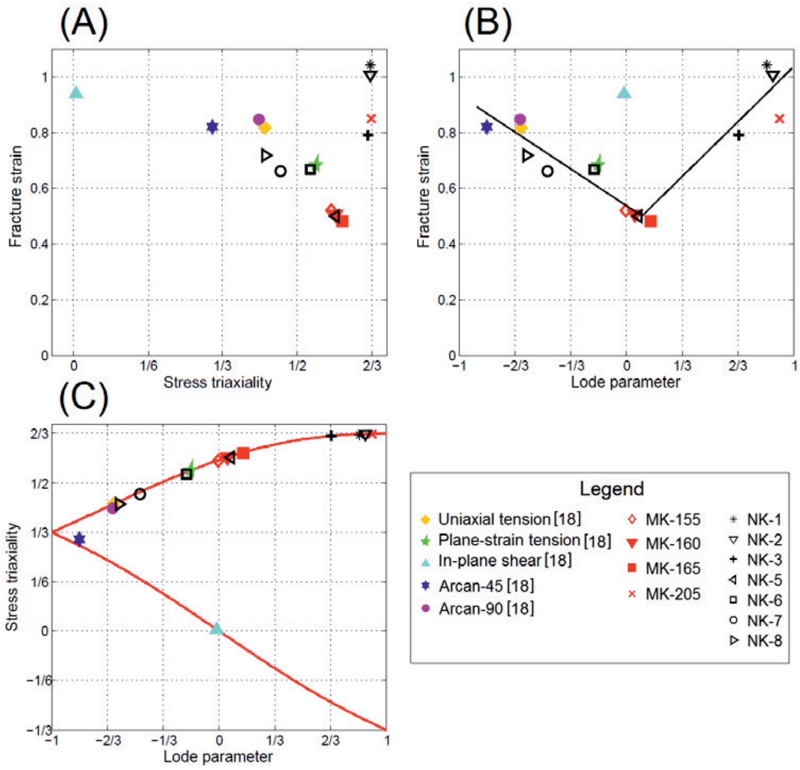

Figure 13 (A) Fracture strain as function of average stress triaxiality. (B) Fracture strain as function of average Lode parameter, a trend line for the tests with $\sigma^*_{\text{avg}} > 1/3$ is marked. (C) Average stress triaxiality versus average Lode parameter for the various tests compared to the plane stress locus.

Table 2 Fracture characteristics data for Docol 600DL steel.

Test name	σ^*_{avg}	μ_{avg}	$\bar{\varepsilon}_f$
Uniaxial tension [18]	0.427	-0.631	0.818
Plane-strain tension [18]	0.542	-0.167	0.682
In-plane shear [18]	0.005	-0.013	0.940
Arcan-45 [18]	0.311	-0.836	0.821
Arcan-90 [18]	-0.415	0.637	0.848
MK-155	0.576	-0.004	0.521
MK-160	0.586	0.049	0.505
MK-165	0.601	0.143	0.481
MK-205	0.666	0.911	0.851
NK-1	0.663	0.8359	1.041
NK-2	0.664	0.870	1.007
NK-3	0.658	0.667	0.791
NK-5	0.585	0.069	0.498
NK-6	0.530	-0.192	0.667
NK-7	0.463	-0.474	0.660
NK-8	0.429	-0.595	0.719

Discussion

From Figure 13(A) it is seen that the tests in plane-strain tension display a drop in ductility compared to the tests in uniaxial tension and equi-biaxial tension. The low ductility in plane-strain tension is coherent with previous observations from thin-walled experiments on a martensitic boron steel by Mohr and Ebnoether [5] and on a TRIP780 steel by Dunand and Mohr [26]. Figure 13(A) also shows that the shear test displays a somewhat larger fracture strain than the tests in uniaxial tension. The abrupt increase in ductility observed when going from plane-strain to equi-biaxial tension in Figure 13(A) is due to a large change in the Lode parameter. This is illustrated by expressing the experimental data in the $\bar{\varepsilon}_f - \mu_{\text{avg}}$ space, see Figure 13(B), where a V-shaped pattern is observed for the tests with $\sigma^* > 1/3$. As can be seen in Figure 13(B), there is a tendency for higher ductility in equi-biaxial tension, $\mu = +1$, than uniaxial tension $\mu = -1$. This is also in accordance with the observations in [5] and [26]. By inspecting

Figure 13(A) it can be seen that the Nakajima tests differ somewhat from the other tests in ductility for comparable stress triaxiality values. In uniaxial tension the fracture strain is lower than in the other tests, while in equi-biaxial tension the ductility is higher than in the other tests. The larger ductility in the equi-biaxial Nakajima tests compared to the M-K result may stem from a through-thickness strain gradient induced by the cone-shaped punch. The fracture strains found in the plane-strain tension Nakajima and M-K tests are consistent. In this case, the effect of the cone is reduced in the Nakajima tests due to the reduced transverse straining. The apparent lower ductility in the Nakajima tests in the lower range of stress triaxiality $(\sigma^*_{\text{avg}} \approx 0.4 - 0.5)$ compared to the tests presented in [18] is harder to explain. This might be due to experimental scatter.

As pointed out above, fracture occurs due to the nucleation-growth-coalescence mechanisms in localized areas. In the literature several fracture criteria have been proposed that include this mechanism, most notably the Rice-Tracey criterion [2] which is uncoupled with the constitutive relation and the Gurson model [27] which is coupled with the constitutive relation. These criteria do not, however, include the effect of the deviatoric stress-state on the fracture strain, and would not be able to predict the drop in ductility in plane-strain tension as observed in Figure 13(A) and (B). Attempts have been made to include the effect of the deviatoric stress state in ductile fracture criteria. Examples of coupled approaches are e.g. the modified versions of the Gurson model presented by Xue [28] and Nahshon and Hutchinson [29]. In a parallel study [30], the modified Mohr-Coulomb criterion presented by Bai and Wierzbicki [31], and the extended Cockcroft-Latham and the extended Rice-Tracey criteria presented in [30] have been assessed for the Docol 600DL material. These three criteria are examples of uncoupled fracture criteria which explicitly takes into account the effect of the deviatoric stress state for low values of stress triaxiality.

Conclusions

In this study, two series of formability tests have been performed using Marciniak-Kuczynski and Nakajima test set-ups. Displacement field data obtained by use of digital image correlation have been used to determine the fracture strain of the material as function of stress triaxiality and Lode parameter. The results have been compared with results from a previous study on the same material with other material tests. The main finding is that the material displays a significant drop of ductility in the range of triaxiality around plane-strain tension, which was not captured by the tests conducted in the previous study. Further, it is found that fracture is due to void growth and coalescence that mainly occurs in localized areas controlled by shear-band instability. The experimental method used for deriving the stress triaxiality, Lode parameter and equivalent strain gives results that are in good agreement with results obtained directly from stress and strain histories of FE models.

ACKNOWLEDGEMENTS

The financial support from of this work from the Structural Impact Laboratory at the Norwegian University of Science and Technology is acknowledged. Thanks are also given to MSc Ragnhild Stormoen for thorough work during the mechanical testing and to Dr Ida Westermann for providing the SEM fractographs. The valuable comments from Prof. Odd S. Hopperstad and Prof. Tore Børvik are appreciated.

REFERENCES

1. McClintock, F.A. (1968) Criterion for ductile fracture by growth of holes. *J. Appl. Mech.* **35,** 363-371.
2. Rice, J.R. and Tracey, D.M. (1969) On the ductile enlargement of voids in triaxial stress fields. *J. Mech. Phys. Sol.* **17,** 201-217.
3. Bao, Y. and Wierzbicki, T. (2004) On fracture locus in the equivalent strain and stress triaxiality space. *Int. J. Mech. Sci.* **46,** 81-98.
4. Barsoum, I. and Faleskog, J. (2007) Rupture mechanisms in combined tension and shear—Experiments. *Int. J. Solids Struct.* **44,** 1768-1786.
5. Mohr, D. and Ebnoether, F. (2009) Plasticity and fracture of martensitic boron steel under plane stress conditions. *Int. J. Solids Struct.* **46,** 3535-3547.
6. Lode, W. (1926) Versuche fiber den Einfluß der mittleren Hauptspannung auf das Fließen der Metalle Eisen, Kupfer und Nickel. *Zeitschrift für Physik: A* **36,** 913-939.
7. Sutton, M.A., Mingqi, C., Peters, W.H., Chao, Y.J. and McNeill, S.R. (1986) Application of an optimized digital correlation method to planar deformation analysis. *Image and Vision Computing* **4,** 143-150.
8. Wu, T., Coret, M. and Combescure, A. (2011) Strain Localisation and Damage Measurement by Full 3D Digital Image Correlation: Application to 15-5PH Stainless Steel. *Strain* **47,** 49-61.
9. Kirugulige, M.S. and Tippur, H.V. (2009) Measurement of Fracture Parameters for a Mixed-Mode Crack Driven by Stress Waves using Image Correlation Technique and High-Speed Digital Photography. *Strain* **45,** 108-122.
10. Luo, P.F. and Wang, C.H. (2008) An Experimental Study on the Elastic–Plastic Fracture in a Ductile Material under Mixed-Mode Loading. *Strain* **44,** 223-230.
11. Wilkins, M.L., Streit, R.D. and Reaugh, J.E. (1980) *Cumulative-strain-damage model of ductile fracture: simulation and prediction of engineering fracture tests*. Technical Report UCRL-53058. Lawrence Livermore National Laboratory.
12. Hancock, J.W. and Brown, D.K. (1983) On the role of strain and stress state in ductile failure. *J. Mech. Phys. Sol.* **31,** 1-24.
13. Johnson, G.R. and Cook, W.H. (1985) Fracture characteristics of three metals subjected to various strains, strain rates, temperatures and pressures. *Eng. Fract. Mech.* **21,** 31-48.
14. Børvik, T., Hopperstad, O.S. and Berstad, T. (2003) On the influence of stress triaxiality and strain rate on the behaviour of a structural steel. Part II. Numerical study. *Eur. J. Mech. - A/Solids* **22,** 15-32.
15. El-Magd, E. and Abouridouane, M. (2006) Characterization, modelling and simulation of deformation and fracture behaviour of the light-weight wrought alloys under high strain rate loading. *International journal of impact engineering* **32,** 741-758.
16. Bridgman, P.W. (1952) *Studies in large plastic flow and fracture: with special emphasis on the effects of hydrostatic pressure* Harvard Univ. Press, Cambridge, Mass.

17. Hancock, J.W. and Mackenzie, A.C. (1976) On the mechanisms of ductile failure in high-strength steels subjected to multi-axial stress-states. *J. Mech. Phys. Sol.* **24,** 147-169.
18. Gruben, G., Fagerholt, E., Hopperstad, O.S. and Børvik, T. (2011) Fracture characteristics of a cold-rolled dual-phase steel *European Journal of Mechanics - A/Solids* **30,** 204-218.
19. Marciniak, Z. and Kuczyński, K. (1967) Limit strains in the processes of stretch-forming sheet metal. *Int. J. Mech. Sci.* **9,** 609-620.
20. Nakajima, K., Kikuma, T. and Hasuka, K. (1968) *Study on the formability of steel sheets*. Yawata Technical Report.
21. SSAB (2009) Docol DP/DL Cold reduced dual phase steels.Swedish Steel AB. http://www.ssab.com/Global/DOCOL/datasheets_docol/en/201_Docol%20DP%20DL.pdf (Accessed: 27.04.2012)
22. Stormoen, R. (2011) Experimental investigation and numerical modelling of sheet metal formability.Master thesis, Norwegian University of Science and Technology.
23. Vacher, P., Dumoulin, S., Morestin, F. and Mguil-Touchal, S. (1999) Bidimensional strain measurement using digital images. *Journal of Mechanical Engineering Science* **213,** 811-817.
24. Hu, S.J., Marciniak, Z. and Duncan, J.L. (2002) *Mechanics of Sheet Metal Forming*. 2nd edn. Butterworth-Heinemann, Woburn.
25. Anderson, T.L. (2005) *Fracture Mechanics; Fundamentals and Applications*. Third edn. Taylor & Francis Group, LLC, Boca Raton.
26. Dunand, M. and Mohr, D. (2010) Hybrid experimental-numerical analysis of basic ductile fracture experiments for sheet metals. *International Journal of Solids and Structures* **47,** 1130-1143.
27. Gurson, A.L. (1977) Continuum theory of ductile rupture by void nucleation and growth, 1. Yield criteria and flow rules for porous ductile media. *J. Eng. Mat. Tech.*, 2-15.
28. Xue, L. (2008) Constitutive modeling of void shearing effect in ductile fracture of porous materials. *Eng Fract Mech* **75,** 3343-3366.
29. Nahshon, K. and Hutchinson, J.W. (2008) Modification of the Gurson Model for shear failure. *Eur J Mech A/Solids* **27,** 1-17.
30. Gruben, G., Hopperstad, O.S. and Børvik, T. (2012) Evaluation of uncoupled ductile fracture criteria for the dual-phase steel Docol 600DL. *Int. J. Mech. Sci.* In press.
31. Bai, Y. and Wierzbicki, T. (2010) Application of extended Mohr–Coulomb criterion to ductile fracture. *Int. J. Fract.* **161,** 1-20.

Part III

G. Gruben, O.S. Hopperstad and T. Børvik

Evaluation of uncoupled ductile fracture criteria for the dual-phase steel Docol 600DL

International Journal of Mechanical Sciences 62 (2012) 133-146

International Journal of Mechanical Sciences 62 (2012) 133–146

Contents lists available at SciVerse ScienceDirect

International Journal of Mechanical Sciences

journal homepage: www.elsevier.com/locate/ijmecsci

Evaluation of uncoupled ductile fracture criteria for the dual-phase steel Docol 600DL

G. Gruben*, O.S. Hopperstad, T. Børvik

Structural Impact Laboratory (SIMLab), Centre for Research-based Innovation (CRI) and Department of Structural Engineering, Norwegian University of Science and Technology, Rich. Birkelands vei 1A, NO-7491 Trondheim, Norway

ARTICLE INFO

Article history:
Received 17 April 2011
Received in revised form
13 June 2012
Accepted 18 June 2012
Available online 26 June 2012

Keywords:
Cockcroft–Latham
Rice–Tracey
Mohr–Coulomb
Ductile fracture

ABSTRACT

The modified Mohr–Coulomb (MMC) fracture criterion recently proposed in the literature and novel extended versions of the Cockcroft–Latham (ECL) and Rice–Tracey (ERT) fracture criteria, explicitly accounting for Lode dependence, are evaluated for the cold-rolled, dual-phase steel Docol 600DL. In addition, two special cases of the ECL criterion as well one special case of the ERT criterion are assessed. To this end, experimental data from uniaxial tension, plane-strain tension, in-plane shear and modified Arcan tests on 2 mm thick steel sheets are utilized. The experimental results display only moderate variation of the fracture strain as a function of the stress state. The criteria are calibrated by using two of the tests, while the remaining three tests are used for validation purposes. The shape of the fracture strain surface as function of stress-state is similar for the MMC, ECL and ERT fracture criteria, but the MMC criterion tends to give a larger range in predicted fracture strain, and the ERT criterion does not distinguish between axisymmetric stress states having Lode parameter equal to $+1$ and -1. The damage evolution of the MMC and ECL criteria are linear functions of the equivalent plastic strain, while the damage evolution is exponential with the equivalent plastic strain for the ERT criterion. The damage evolution of the ERT criterion displays a similar shape as the evolution of void area fraction of a comparable steel material. The fracture strains obtained with the fracture criteria are compared with experimental data. In order to extend the range of the experimental validation, additional data from formability tests conducted on material from the same batch are employed. The ECL criterion gave good predictions on the equivalent strain at fracture initiation, while a somewhat larger spread was observed for the ERT and MMC criteria.

1. Introduction

Over the years several criteria have been proposed to describe ductile fracture. These criteria can be divided into two main groups: criteria using a coupled approach and criteria using an uncoupled approach. For the criteria with a coupled approach, influence of damage is included in the constitutive equations. This can be modelled by porous plasticity, e.g., Shima [1], Gurson [2] and Rousselier [3], or by continuum damage mechanics, e.g., Lemaitre and Chaboche [4] and Lemaitre [5]. In the criteria with the uncoupled approach, the yield criterion, plastic flow and strain hardening are unaffected by the damage. Examples of such criteria are Freudenthal [6], Cockcroft-Latham [7], Wilkins [8], Johnson-Cook [9] and Xue-Wierzbicki [10]. The coupled approach is, in general, based on a more sound physical theory, but the identification of the parameters is usually more involved.

The physical mechanism controlling ductile fracture is the nucleation, growth and coalescence of microvoids in the material during plastic deformation [11]. The Rice–Tracey (RT) criterion [12] describes the growth of a spherical void with radius R in an infinite medium. It was assumed that the material was perfectly plastic and obeying the von Mises yield criterion with the associated flow rule. According to the RT criterion, the void growth is defined by

$$\frac{\dot{R}}{R} = \kappa_g \exp(\psi\sigma^*)\dot{\bar{\varepsilon}}^p \tag{1}$$

where $\kappa_g = 0.283$ and $\psi = 1.5$; $\bar{\varepsilon}^p$ is the equivalent plastic strain, and σ^* is the stress triaxiality defined as

$$\sigma^* = \frac{\sigma_h}{\bar{\sigma}} \tag{2}$$

The hydrostatic stress σ_h and the equivalent von Mises stress $\bar{\sigma}$ are in turn given by

$$\sigma_h = \tfrac{1}{3}(\sigma_I + \sigma_{II} + \sigma_{III}) \tag{3}$$

$$\bar{\sigma} = \sqrt{\tfrac{1}{2}\left[(\sigma_I - \sigma_{II})^2 + (\sigma_{II} - \sigma_{III})^2 + (\sigma_{III} - \sigma_I)^2\right]} \tag{4}$$

---

* Corresponding author. Tel.: +47 73 59 46 87; fax: +47 73 59 47 01.
E-mail address: gaute.gruben@ntnu.no (G. Gruben).

0020-7403/$ - see front matter © 2012 Elsevier Ltd. All rights reserved.
http://dx.doi.org/10.1016/j.ijmecsci.2012.06.009

In Eqs. (3) and (4), σ_i, $i=I$, II, III are the principal stresses ordered so that $\sigma_I \geq \sigma_{II} \geq \sigma_{III}$. The Rice–Tracey criterion is widely used in prediction of ductile fracture, see e.g., [3,13–14]. It is then common to assume that fracture (or void coalescence) initiates as the void growth ratio R/R_0 reaches a critical value $(R/R_0)_C$, where R_0 is the initial void radius. As discussed in [3], it is possible to combine the RT criterion for void growth with a void nucleation criterion, a void coalescence criterion accounting for both the void growth ratio and the void spacing, and the length scale introduced by the microstructure of the material.

A phenomenological approach to describe ductile fracture was presented by Cockcroft and Latham in [7]. The Cockcroft–Latham (CL) criterion states that fracture occurs when the tensile principal stress integrated over the strain path reaches a critical value

$$W = \int_0^{\bar{\varepsilon}^p} \langle \sigma_I \rangle d\bar{\varepsilon}^p \leq W_C, \quad \langle \sigma_I \rangle = \max(\sigma_I, 0) \tag{5}$$

where W_C is the critical value of W at which fracture occurs. This criterion has since its introduction been used in many studies to describe ductile fracture, e.g., [15–18]. Calibrated for a given material, both the RT and the CL fracture criteria implicitly express the equivalent plastic strain at fracture, $\bar{\varepsilon}_f^p$, henceforth called the fracture strain, as a decreasing function of the hydrostatic stress (assuming a constant value of the Lode parameter, see below). This is coherent with micromechanical theory, since increased hydrostatic pressure restrains the void growth [11,12].

Recent studies on an aluminium alloy conducted by Bao and Wierzbicki [19], two steel types examined by Barsoum and Faleskog [20] and a dual-phase steel investigated by Gruben et al. [21] indicate that the fracture strain does not decrease monotonically with increased hydrostatic stress for some ductile metals in the low range of stress triaxiality. Thus the deviatoric stress state should explicitly be taken into account when predicting the fracture strain for low triaxiality stress states. As a supplement to the hydrostatic stress-state parameter, σ^*, the deviatoric stress state can be represented by the Lode parameter, μ, defined by the principal stresses as [22]

$$\mu = \frac{2\sigma_{II} - \sigma_I - \sigma_{III}}{\sigma_I - \sigma_{III}} \tag{6}$$

Three special cases of the Lode parameter are identified, namely generalized tension ($\mu = -1$), generalized shear ($\mu = 0$) and generalized compression ($\mu = +1$) [20]. The Mohr–Coulomb criterion has been widely used as an uncoupled approach for materials like rock and soil, e.g., [23]. Recently, Bai and Wierzbicki [24] proposed a modified version of the Mohr–Coulomb criterion for use with ductile metals. The criterion was calibrated and validated for the aluminium alloy 2024-T351 and the TRIP RA-K40/70 steel sheet material. The criterion gave good prediction of the fracture strain as a function of stress triaxiality in plane stress, and captured well the variation in fracture strain in the low range of stress triaxiality.

In this study, three uncoupled ductile fracture criteria, all of which account explicitly for the stress triaxiality and the Lode dependence of the damage evolution, have been assessed. The considered fracture criteria was the modified Mohr–Coulomb (MMC) criterion proposed by Bai and Wierzbicki [24] and novel extensions of the Cockcroft–Latham (ECL) and Rice–Tracey (ERT) criteria. The data extracted from a hybrid experimental-numerical study of a 2 mm thick dual-phase steel sheet conducted by Gruben et al. [25] comprising results from uniaxial tension, plane-strain tension, in-plane shear and modified Arcan tests are used in evaluating the fracture criteria. The fracture strain collected from the through-thickness centre of the numerical models of the five tests in [25] displayed low variation as a function of stress state, while the fracture strain measured experimentally on the surface through optical measurements displayed more variation in ductility. It was argued [25] that for simulations with 3D solid elements, a calibration should be based on data from the through thickness centre, while a calibration for plane-stress elements could be based on data from the surface. A more recent study on material from the same batch carried out using Marciniak–Kuczynski and Nakajima set-ups [21] found that the material displays a significant drop in ductility in plane-strain tension compared to uniaxial tension and biaxial tension. In [21] the data were obtained from the surface of the specimens through optical measurements. A second calibration of the fracture criteria was carried out through an optimization of the data from the surface of the specimens in [21] and [25]. This gave an opportunity to assess the predicted equivalent strain at fracture by the criteria on two datasets; one from the surface and one from the centre of the specimens.

2. Experimental–numerical program

Gruben et al. [25] conducted experiments on specimens under five different stress states in the low range of stress triaxiality. The material used was a cold-rolled, dual-phase steel of type Docol 600DL delivered by Swedish Steel Ltd. (SSAB). The chemical composition of the material is given in Table 1 [26]. The specimens were cut from a 2 mm thick plate with the longitudinal axis along the rolling direction. Fig. 1 shows the geometry of the four different specimen types used (uniaxial tension, plane-strain tension, in-plane shear and modified Arcan). The test set-up for the modified Arcan tests is shown in Fig. 2, and the β value was set to, respectively 45° and 90° in these tests. All experiments were conducted at room temperature under quasi-static loading with pre-necking strain rates in the vicinity of $10^{-3}\,\mathrm{s}^{-1}$. The force and displacement were measured in each test by the hydraulic test machine. Digital image correlation was used to measure the displacement field and to calculate the strain field on the surface of the specimens. The point of fracture initiation was identified in each test, and a novel method for determining the stress triaxiality σ^*, the Lode parameter μ and the fracture strain $\bar{\varepsilon}_f$ from the optical measurements were presented and employed. In this approach a Levy–Mises material was assumed, i.e., $\bar{\varepsilon}_f^p = \bar{\varepsilon}_f$.

The stress state was determined from Finite Element (FE) simulations of the five tests. All numerical analyses were executed by the implicit solver of the non-linear finite element code LS-DYNA 971 [27]. For all the FE models 8-node trilinear brick elements with selective reduced integration were used. The FE models had nine elements over the thickness. The geometries and meshes of the FE models are shown in Fig. 3, while the characteristic in-plane element size at the spatial point of fracture initiation of each model is given in Table 2. The nominal elastic properties were described by a Young's modulus of 210 GPa and a Poisson's ratio of 0.33, while the plastic behaviour was described by the rate-dependent J_2 flow theory. The flow stress, $\bar{\sigma}$, was expressed by the extended Voce rule and a multiplicative viscosity-hardening law as

$$\bar{\sigma} = \left(\sigma_0 + \sum_{i=1}^{n} Q_i \left(1 - \exp(-C_i \bar{\varepsilon}^p)\right) \right) \left(1 + \frac{\dot{\bar{\varepsilon}}^p}{\dot{\varepsilon}_0} \right)^q \tag{7}$$

where σ_0 represents the yield stress, and Q_i and C_i ($i=1,2$) are material parameters governing in turn the primary and the

Table 1
Chemical composition of Docol 600DL (in wt%) [26].

C	Si	Mn	P	S	Al_{tot}
0.10	0.40	1.50	0.010	0.002	0.040

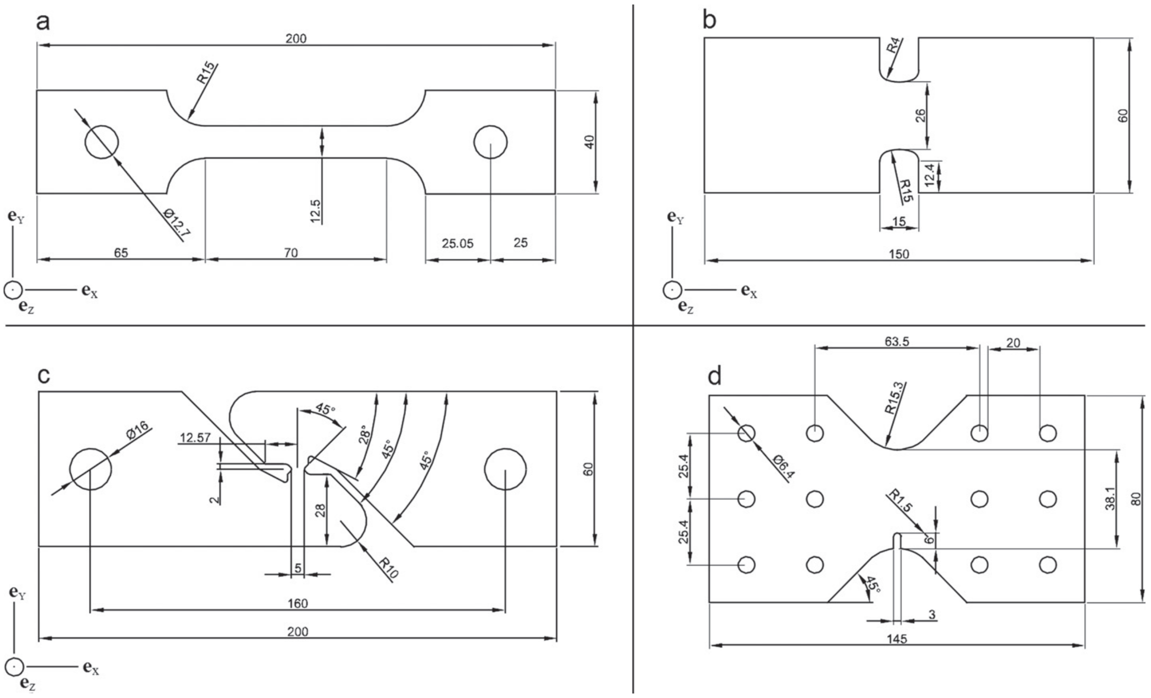

Fig. 1. Geometry of the test specimens (in mm): (a) uniaxial tension specimen, (b) plane-strain tension specimen, (c) in-plane shear specimen and (d) modified Arcan specimen [25].

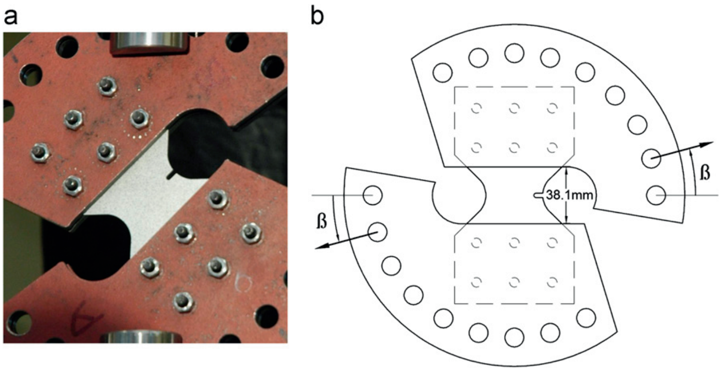

Fig. 2. (a) Modified Arcan test set-up with $\beta=45^\circ$ and (b) sketch of brackets with specimen defining the loading direction β [25].

secondary hardening. The parameters q and $\dot{\varepsilon}_0$ defines the strain-rate sensitivity of the steel. The hardening parameters were found by a fit of the pre-necking values of the Cauchy stress versus logarithmic plastic strain curve from the uniaxial tension test, and by inverse modelling for large strains using the uniaxial tension and the shear test. The post-processing of the FE simulations was stopped when the effective logarithmic strain at the (surface) point of fracture initiation in the FE models reached the optically measured value [25]. The FE simulations displayed that the equivalent plastic strain and the stress triaxiality in the centre of the specimens subjected to tensile loading were larger than at the surface, and so fracture is more likely to initiate here in these instances. Fig. 4(a) displays the trajectories of the equivalent plastic strain, $\overline{\varepsilon}^p(t)$, versus the stress triaxiality, $\sigma^*(t)$, from the centre element of the five simulations, where t is the time. The average stress triaxiality and Lode parameter were calculated over the strain path, i.e.,

$$\sigma^*_{\text{avg}} = \frac{1}{\overline{\varepsilon}^p_f}\int_0^{\overline{\varepsilon}^p_f} \sigma^*(\overline{\varepsilon}^p)d\overline{\varepsilon}^p, \quad \mu_{\text{avg}} = \frac{1}{\overline{\varepsilon}^p_f}\int_0^{\overline{\varepsilon}^p_f} \mu(\overline{\varepsilon}^p)d\overline{\varepsilon}^p \tag{8}$$

The fracture strain collected from the centre of the specimens is plotted versus the average values of the stress triaxiality in Fig. 4(b). The stress state in the form of the average Lode parameter and the average stress triaxiality collected from the centre of the specimens in the five simulations are shown in Fig. 5(a) together with the loci for generalized tension ($\mu=-1$), generalized shear ($\mu=0$), generalized compression ($\mu=+1$) and

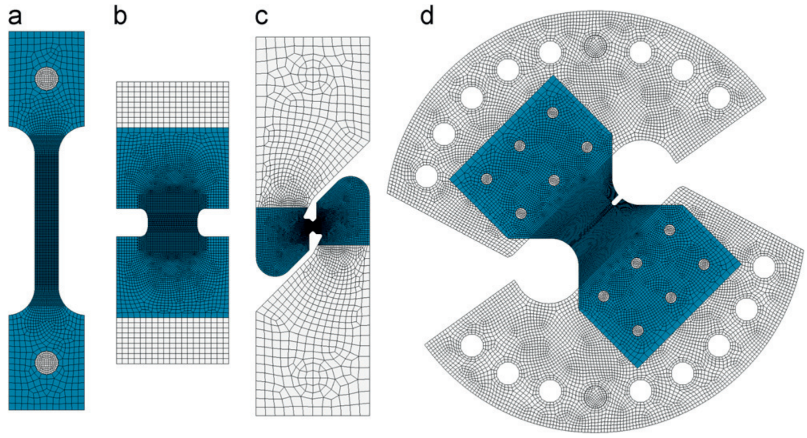

Fig. 3. Finite element meshes of the test specimens [25].

Table 2
Characteristic in-plane element size used in the FE models (in mm).

Tension	Plane strain	Shear	Arcan
0.50	0.46	0.10	0.36

plane stress. Assuming the von Mises yield criterion, the plane stress locus is defined by Eq. (12) below.

For reasons that will be explained in Section 5.1, new FE simulations of the tests were conducted in this study with an extra hardening term in the strain hardening function. That is, in Eq. (7), Q_i and C_i with ($i=1, 2, 3$) are used. The tertiary hardening term was added to include strain hardening for large strains ($\bar{\varepsilon}^p > 1.0$). The hardening parameters were found from curve fitting and inverse modelling like in the former analyses. Table 3 shows the calibrated parameters used in the constitutive equation. The simulated time at fracture, t_f, was found in a similar way as in [25], and the post-processing of the results was stopped at t_f. The same FE models as used in [25] were used in this study, but this time they were run with the explicit solver of LS-DYNA. A time scaling by a factor 10^5 was found necessary to reduce the simulation times. It was carefully checked that the kinetic energy was negligible compared to the internal energy of the specimens. The results from the new FE simulations in terms of the dimensionless parameters $\sigma^*_{\text{avg}}, \mu_{\text{avg}}$ and $\bar{\varepsilon}^p_f$ are within 0.01 of the values produced in [25]. Table 4 sums up the most important results from the combined experimental–numerical program where the new simulations have been used. Note that the use of time scaling was compensated by increasing the material constant $\dot{\varepsilon}_0$ in the multiplicative viscosity hardening law defined in Eq. (7) by a factor 10^5. The time scaling further led to a corresponding increase in the strain rate values summed up in Table 4. The calibration and validation of the various fracture criteria in this study are based on the new simulations.

As shown in Fig. 4, the material undergoes large straining before fracture. In the former study [25] it was therefore assumed that the fracture process for the material is governed by microporosity under the stress states investigated. However, as a part of this study an investigation of the fracture surface has been carried out. Fig. 6 shows fractographs taken in a scanning electron microscope (SEM) at the assumed location of fracture initiation in selected specimens from the uniaxial tension, plane-strain tension and in-plane shear tests. All specimens show ductile fracture with dimples. On the macroscopic level, the uniaxial tension test displays a less rough surface than the plane-strain tension test, while the in-plane shear test exhibits a smooth fracture surface. Further, most of the dimples seen in the uniaxial tension and plane-strain tension tests are small and less than 5 μm, which may indicate that fracture is dominated by nucleation of voids as the voids do not grow larger. Some inclusions are observed in the uniaxial tension and plane-strain tension tests, which are marked with an '*i*', while some shear dominated areas are marked with an '*s*'. In the shear test, elongated dimples typical for shear failure are observed.

The observation of small dimples in the fractographs is coherent with the observations from fractographs of the Marciniak–Kuczynski and Nakajima tests carried out on material specimens from the same batch and presented in [21]. The stress triaxiality σ^*, the Lode parameter μ, and the fracture strain $\bar{\varepsilon}_f$ at the surface of the Marciniak–Kuczynski and Nakajima specimens were collected using digital image correlation and the method introduced in [25]. The two studies [21] and [25] give together data from the surface of specimens in 16 tests. The fracture strain $\bar{\varepsilon}_f$ as function of average triaxiality σ^*_{avg} at the surface of the specimens in these tests are presented in Fig. 4(c), while Fig. 5(b) gives the average triaxiality σ^*_{avg} as a function of the average Lode parameter μ_{avg} as well as the loci for generalized tension ($\mu=-1$), generalized shear ($\mu=0$), generalized compression ($\mu=+1$) and plane stress. As pointed out in [25], the fracture strain as function of stress triaxiality in the uniaxial tension, plane-strain tension, in-plane shear and modified Arcan tests exhibits a larger variation on the surface of the specimens than in the centre, and this can be observed by comparing Fig. 4(b) and Fig. 4(c). Further, as pointed out in [21] and seen from Fig. 4(c), the material displays a significant drop in ductility in plane-strain tension compared to uniaxial tension and biaxial tension. This is coherent with the findings of Clausing [28], where the ductility for seven different steels are significantly reduced in plane-strain tension compared to uniaxial tension. More recent studies on plane-stress specimens, e.g., Mohr and Ebnoether [29] for a boron steel and Dunand and Mohr [30] for a TRIP steel, have observed a similar drop in ductility in plane-strain tension as well as an increase in biaxial tension. It is noted that contrary to the data collected from the surface, the data collected from the centre of the specimens in [25] are not exactly in plane stress. This can be seen from Fig. 5(a) and (b) where the data from the surface of the

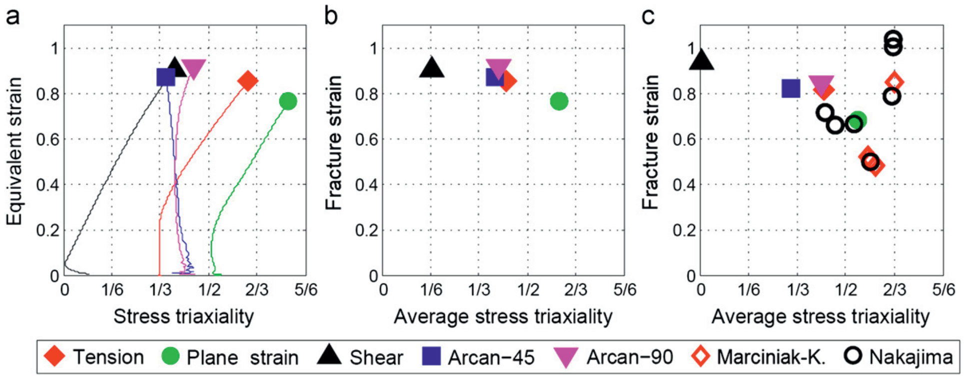

Fig. 4. (a) Trajectories of $\sigma^*(t)$–$\bar{\varepsilon}^p(t)$ from the centre of the specimens, (b) $\bar{\varepsilon}_f^p$ versus σ^*_{avg} from the centre of the specimens and (c) $\bar{\varepsilon}_f$ versus σ^*_{avg} from the surface of the specimens.

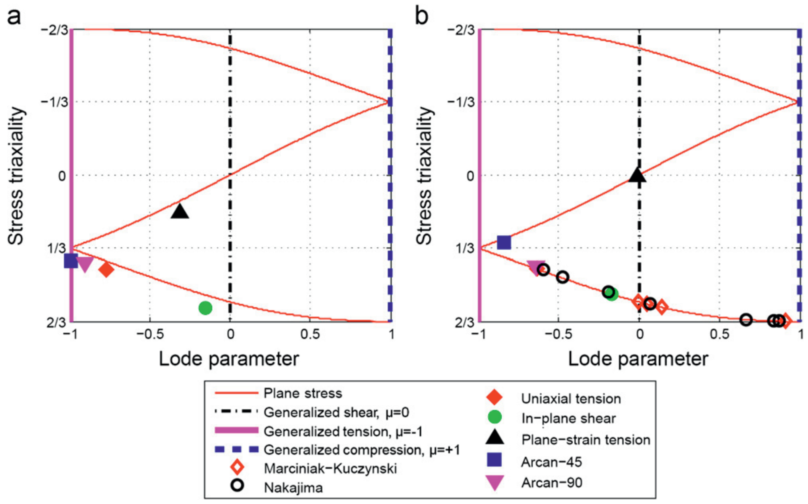

Fig. 5. The (σ^*,μ) space with loci representing states of plane stress, generalized shear, generalized tension and generalized compression: (a) $(\sigma^*_{\text{avg}},\mu_{\text{avg}})$ values from the centre of the specimens based on FE simulations and (b) $(\sigma^*_{\text{avg}},\mu_{\text{avg}})$ values from the surface of the specimens based on DIC measurements.

Table 3
Values used in the rate-dependent extended Voce hardening model. The large value for $\dot{\varepsilon}_0$ is due to the time scaling.

σ_0 [MPa]	Q_1 [MPa]	C_1	Q_2 [MPa]	C_2	Q_3 [MPa]	C_3	$\dot{\varepsilon}_0[s^{-1}]$	q
286.2	287.9	34.93	341.1	5	6000	0.01	100	0.005

Table 4
Resulting values from the experimental–numerical analyses on Docol 600DL. The large values on the strain rates are due to the time scaling.

	σ^*_{avg}	μ_{avg}	$\bar{\varepsilon}_f^p$	$\dot{\bar{\varepsilon}}_{\text{avg}}$ $[s^{-1}]$	$\dot{\bar{\varepsilon}}_f$ $[s^{-1}]$
Uniaxial tension	0.428	−0.771	0.855	915	1916
Plane strain	0.607	−0.152	0.765	479	840
In-plane shear	0.172	−0.313	0.909	185	298
Arcan-45	0.390	−0.991	0.876	353	511
Arcan-90	0.399	−0.901	0.916	833	800

specimens are closer to the plane-stress locus than the data from the centre of the specimens. The small deviation from the plane-stress locus in Fig. 5(b), most notably seen in the Arcan-45 test, stems from the averaging defined by Eq. (8).

3. Fracture criteria

3.1. The modified Mohr–Coulomb criterion

The Mohr–Coulomb criterion is expressed as

$$\tau + c_1\sigma_n = c_2 \tag{9}$$

where τ is the shear stress and σ_n is the normal stress at fracture on the critical plane of the material. c_1 is often referred to as the friction, while c_2 is the cohesion. The limits of the parameters are $c_1 \geq 0$ and $c_2 > 0$. The criterion can be expressed in terms of the maximum and minimum principal stresses at fracture as

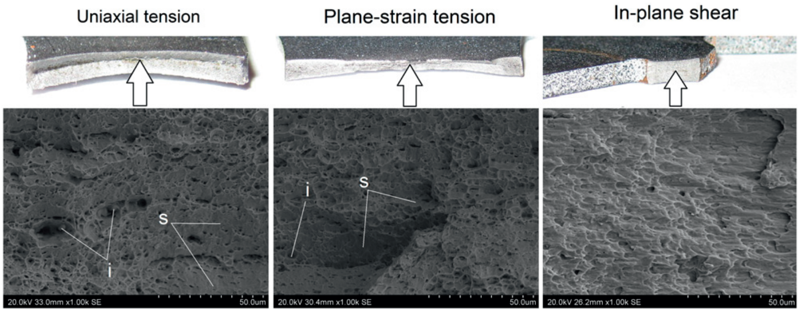

Fig. 6. SEM photographs taken at the centre of the fracture surface of representative uniaxial tension, plane-strain tension and in-plane shear specimens. Some inclusions are marked with an '*i*' and some zones failing in shear are marked with '*s*'.

(see, e.g., Bai and Wierzbicki [24])

$$\left(\sqrt{1+c_1^2}+c_1\right)\sigma_I-\left(\sqrt{1+c_1^2}-c_1\right)\sigma_{III}=2c_2 \tag{10}$$

Alternatively, the Mohr–Coulomb criterion can be expressed as

$$\phi\sigma_I+(1-\phi)(\sigma_I-\sigma_{III})=C \tag{11}$$

where

$$\phi=\frac{2c_1}{\sqrt{1+c_1^2}+c_1},\quad 0\le\phi\le1,\quad \text{and}\quad C=\frac{2c_2}{\sqrt{1+c_1^2}+c_1}>0$$

For an isotropic material the stress state can be expressed by three invariants. One possible combination is the von Mises equivalent stress, $\overline{\sigma}$, the stress triaxiality, σ^*, and the Lode parameter, μ. By solving the expressions in Eqs. (2), (4) and (6) with respect to the principal stresses, we have

$$\sigma_I=\left(\sigma^*+\frac{3-\mu}{3\sqrt{3+\mu^2}}\right)\overline{\sigma},\quad \sigma_{II}=\left(\sigma^*+\frac{2\mu}{3\sqrt{3+\mu^2}}\right)\overline{\sigma},$$
$$\sigma_{III}=\left(\sigma^*-\frac{3+\mu}{3\sqrt{3+\mu^2}}\right)\overline{\sigma} \tag{12}$$

The Mohr–Coulomb criterion can now be expressed in terms of the invariants $\overline{\sigma}$, σ^* and μ, by inserting $(\sigma_I,\ \sigma_{III})$ from Eq. (12) into Eq. (11), and the result reads as

$$\frac{\phi\left(3\sigma^*\sqrt{3+\mu^2}-3-\mu\right)+6}{3\sqrt{3+\mu^2}}\overline{\sigma}=C \tag{13}$$

Bai and Wierzbicki [24] presented a modified version of the Mohr–Coulomb criterion (the MMC criterion) which is expressed by an accumulative damage variable. To achieve this, an expression for the fracture strain is required. As the Docol 600DL material is described by the von Mises yield criterion, the fracture strain for proportional strain paths can be found by combining Eq. (13) with Eq. (7). The fracture strain, $\overline{\varepsilon}_f^p$, is then defined implicitly as a function of the fracture parameters (φ, C), the stress state (μ, σ^*), the constitutive parameters $(\sigma_0,Q_i,C_i,q,\dot{\varepsilon}_0)$, and the equivalent plastic strain rate $\dot{\overline{\varepsilon}}^p$. The MMC criterion is then expressed as

$$D(\overline{\varepsilon}^p)=\int_0^{\overline{\varepsilon}^p}\frac{d\overline{\varepsilon}^p}{\overline{\varepsilon}_f^p} \tag{14}$$

where $\overline{\varepsilon}_f^p$ for the Docol 600DL material is calculated from Eqs. (7) and (13), and fracture initiates when D equals unity. Even if $\overline{\varepsilon}_f^p$ in Eq. (14) is defined for proportional loading conditions, the MMC criterion is assumed valid for non-proportional loading owing to the damage accumulation rule.

3.2. The extended Cockcroft–Latham criterion

While the starting point for the MMC criterion was the stress-based Mohr–Coulomb criterion, the extended Cockcroft–Latham (ECL) criterion assumes that the damage evolution is driven by the plastic power per unit volume amplified by a factor representing the influence of the stress triaxiality and the Lode parameter. The ECL criterion is here defined as

$$D=\frac{1}{W_C}\int_0^{\overline{\varepsilon}^p}\left\langle\phi\frac{\sigma_I}{\overline{\sigma}}+(1-\phi)\left(\frac{\sigma_I-\sigma_{III}}{\overline{\sigma}}\right)\right\rangle^{\gamma}\overline{\sigma}d\overline{\varepsilon}^p \tag{15}$$

where $\langle\cdot\rangle$ is the Macaulay brackets and $W_C\ge0$, $\gamma\ge0$ and $0\le\varphi\le1$ are the fracture parameters. Here W_C defines the overall ductility of the material, φ controls the relative influence of the major principal stress and the maximum shear stress, and γ governs the strength of the stress-state dependence. As for the MMC criterion, it is assumed that fracture initiates as D equals unity. By examining the expression in Eq. (15), we find the following special cases of the ECL criterion

$$\phi=1,\quad\gamma=1\quad\Rightarrow\quad D=\tfrac{1}{W_C}\int\langle\sigma_I\rangle d\overline{\varepsilon}^p\qquad\text{(Cockcroft-Latham criterion)}$$
$$\phi=0,\quad\gamma=0\quad\Rightarrow\quad D=\tfrac{1}{W_C}\int\overline{\sigma}d\overline{\varepsilon}^p\qquad\text{(Freudenthal criterion)}$$
$$\phi=0,\quad\gamma=1\quad\Rightarrow\quad D=\tfrac{1}{W_C}\int(\sigma_I-\sigma_{III})d\overline{\varepsilon}^p\qquad\text{(Integral-based Tresca criterion)}$$

The Freudenthal criterion [6] implies that damage depends entirely on the plastic power per unit volume, while the integral-based Tresca criterion is independent of the hydrostatic stress state.

The ECL criterion can, in the same manner as the Mohr–Coulomb criterion, be expressed by the invariants $(\overline{\sigma},\sigma^*,\mu)$, by inserting the expressions for σ_I and σ_{III} from Eq. (12) into Eq. (15). Setting D equal to unity at fracture, the ECL criterion is formulated as

$$\int_0^{\overline{\varepsilon}_f^p}\left\langle\frac{\phi\left(3\sigma^*\sqrt{3+\mu^2}-3-\mu\right)+6}{3\sqrt{3+\mu^2}}\right\rangle^{\gamma}\overline{\sigma}d\overline{\varepsilon}^p=W_C \tag{16}$$

Under the assumption of proportional straining, combination of Eq. (16) with Eq. (7) for the constitutive relation gives an implicit equation for the fracture strain as function of stress state, i.e., $\overline{\varepsilon}_f^p=\overline{\varepsilon}_f^p(\sigma^*,\mu)$. Although it is not necessary to calculate this function in an FE implementation of the criterion, it can be helpful in evaluating its properties, see Section 5.1.

3.3. The extended Rice–Tracey criterion

As shown by, e.g., Rousselier [3], the Rice–Tracey criterion for void growth may be written as

$$\dot{f}=3\kappa_g f(1-f)\exp\left(\psi\sigma^*\right)\dot{\overline{\varepsilon}}^p \tag{17}$$

where f is the void volume fraction. It is assumed here that κ_g and ψ are parameters that may be fitted to experimental data, and the void growth relation is assumed to be valid also for hardening materials. The initial void volume fraction is f_0, whereas nucleation of voids is neglected. It should, however, be noted that void nucleation is readily included as explained in [3]. To account for damage growth in shear-dominated stress states at low stress triaxiality, and thereby introducing the Lode dependence, the original RT criterion has to be augmented. Following along the same lines as Nahshon and Hutchinson [31] in their modification of the Gurson model, Eq. (17) is extended to

$$\dot{f} = 3\kappa_g f(1-f)\exp(\psi\sigma^*)\dot{\bar{\varepsilon}}^p + \kappa_s f\omega(\mu)\dot{\bar{\varepsilon}}^p \tag{18}$$

here, κ_s is a constant, whereas $0 \le \omega(\mu) \le 1$ is a function of the Lode parameter, viz.

$$\omega(\mu) = 1 - \frac{(9\mu-\mu^3)^2}{(\mu^2+3)^3} \tag{19}$$

The parameter ω is zero for axisymmetric stress states ($\mu = \pm 1$) and unity for stress states given by a pure shear stress plus a hydrostatic pressure ($\mu=0$) (see [31] for details). As pointed out in [31], f should now be regarded as an effective void volume fraction or rather a damage variable, since it is no longer uniquely defined by the classical void growth relation. In the special case of axisymmetric stress states, ω is equal to zero, and then f can still be identified as the void volume fraction. As commonly assumed for the original RT fracture criterion, it is here assumed that fracture occurs as f reaches a critical value f_C. It is sometimes convenient to work with an alternative damage variable, $D=f/f_C$, which equals $D_0=f_0/f_C$ in the reference configuration and unity at fracture initiation.

Assuming proportional loading, the fracture strain can be obtained by integration of Eq. (18) as

$$\bar{\varepsilon}_f^p = \int_0^{\bar{\varepsilon}_f^p} d\bar{\varepsilon}^p = \int_{f_0}^{f_C} \frac{df}{3\kappa_g f(1-f)\exp(\psi\sigma^*) + \kappa_s f\omega(\mu)}$$

$$\bar{\varepsilon}_f^p = \frac{1}{3\kappa_g\exp(\psi\sigma^*) + \kappa_s\omega(\mu)} \ln\frac{f_C((1-f_0)3\kappa_g\exp(\psi\sigma^*) + \kappa_s\omega(\mu))}{f_0((1-f_C)3\kappa_g\exp(\psi\sigma^*) + \kappa_s\omega(\mu))} \tag{20}$$

This expression is useful in the calibration of the fracture parameters based on experimental data. If f_0 and f_C are assumed to be small compared with unity, Eq. (20) reduces to

$$\bar{\varepsilon}_f^p \approx \frac{\ln(f_C/f_0)}{3\kappa_g\exp(\psi\sigma^*) + \kappa_s\omega(\mu)} \tag{21}$$

In this case, the function $\bar{\varepsilon}_f^p = \bar{\varepsilon}_f^p(\sigma^*, \mu)$ depends on the parameter ψ and the two compound parameters $\kappa_g/\ln(f_C/f_0)$ and $\kappa_s/\ln(f_C/f_0)$.

4. Parameter identification

The three fracture criteria presented in Section 3 are calibrated from the experimental–numerical analyses of the uniaxial tension test and the in-plane shear test. The elements used for collecting the data are shown in Fig. 7. The post-processing of the FE models are stopped when the simulation time at fracture, t_f, is reached. Since a rate-dependent constitutive model is utilized, the strain rate at fracture, $\dot{\bar{\varepsilon}}_f^p$, is used in the calibration of the MMC criterion, while the average strain rate, $\dot{\bar{\varepsilon}}_{\text{avg}}^p$, is used in the calibration of the ECL criterion. These quantities are here defined as

$$\dot{\bar{\varepsilon}}_f^p = \dot{\bar{\varepsilon}}^p(t_f), \quad \dot{\bar{\varepsilon}}_{\text{avg}}^p = \frac{1}{\bar{\varepsilon}_f^p}\int_0^{\bar{\varepsilon}_f^p} \dot{\bar{\varepsilon}}^p(\bar{\varepsilon}^p)d\bar{\varepsilon}^p \tag{22}$$

It is noted that the effect of the strain rate on the calibration is small. The strain rates from the different simulations are summarized in Table 4. Since the ERT and RT criteria are independent of the constitutive relation, the strain-rate and the constitutive parameters are not needed to calibrate these fracture criteria.

The MMC criterion is calibrated by combining Eq. (13) with Eq. (7) and assuming that the loading is approximately proportional. The average parameters σ_{avg}^* and μ_{avg} together with $\bar{\varepsilon}_f^p$ and $\dot{\bar{\varepsilon}}_f^p$ from Table 4 are used in the calibration, and the two resulting algebraic equations yields $\varphi=0.208$ and $C=1037$ MPa.

For the ECL criterion the parameter γ is set to unity, due to the limited variation of the fracture strain with stress state, while the parameters φ and W_C are calculated directly from Eq. (15) utilizing the principal stress histories from the FE models. The resulting values are calculated from the two nonlinear equations by the secant method, and this gives $\varphi=0.383$ and $W_C=790$ MPa.

Calibrations have also been carried out for two of the three special cases of the ECL criterion. The Cockcroft–Latham criterion gives $W_C=722$ MPa, while the integral-based Tresca criterion gives $W_C=832$ MPa. Both these criteria are calculated directly from Eq. (15) utilizing the principal stress histories from the FE models. These two criteria only need one test to be calibrated, but the calibrated values given here are average values from the tension and shear test, i.e., $W_C = (W_C^{\text{tension}} + W_C^{\text{shear}})/2$.

In the ERT criterion, the ψ parameter is set to 1.5 as in the original RT criterion [12]. The initial and critical values of f were not measured experimentally for Docol 600DL. However, Avramovic-Cingara et al. [32] measured the evolution of the void area fraction in uniaxial tensile tests made from a 1.8 mm DP600 steel sheet. In their study, the approximate values of the initial and critical void area fractions were found to be 0.001 and 0.013, respectively. By invoking the principle of Delesse, these values are used here as f_0 and f_C in the calibration of the ERT criterion. Since these values are small compared with unity, their exact values will only influence the calibrated values of κ_g and κ_s. The average value of the function $\omega=\omega(\mu)$, denoted ω_{avg}, in the uniaxial

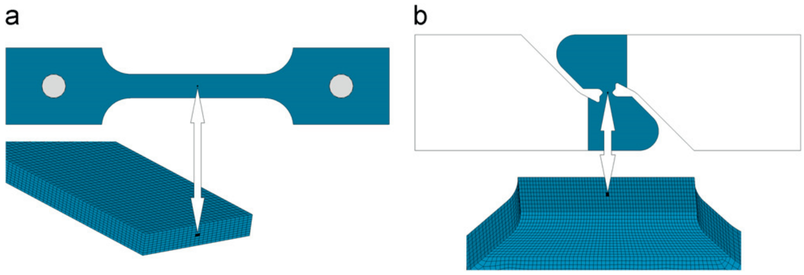

Fig. 7. Elements used for calibration of fracture criteria: (a) uniaxial tension test and (b) in-plane shear test [25].

tension and the in-plane shear tests, respectively, was found by inserting μ_{avg} from Table 4 into Eq. (19). The parameters ω_{avg} and σ^*_{avg} were then inserted into Eq. (20) together with f_0, f_C and ψ. The resulting two algebraic equations gave $\kappa_g=0.509$ and $\kappa_s=1.154$. The original RT criterion (i.e., $\kappa_s=0$) was calibrated based on the tension and shear tests. Using $\psi=1.5$, $\kappa_s=0$, $f_0=0.001$ and $f_C=0.013$, the optimal value of the void growth parameter was $\kappa_g=0.651$. Note also that Rousselier [3] stated that κ_g seems to depend on f_0, and should be in the vicinity of 0.5–0.7 for initial void volume fractions of the order $10^{-3}-10^{-4}$.

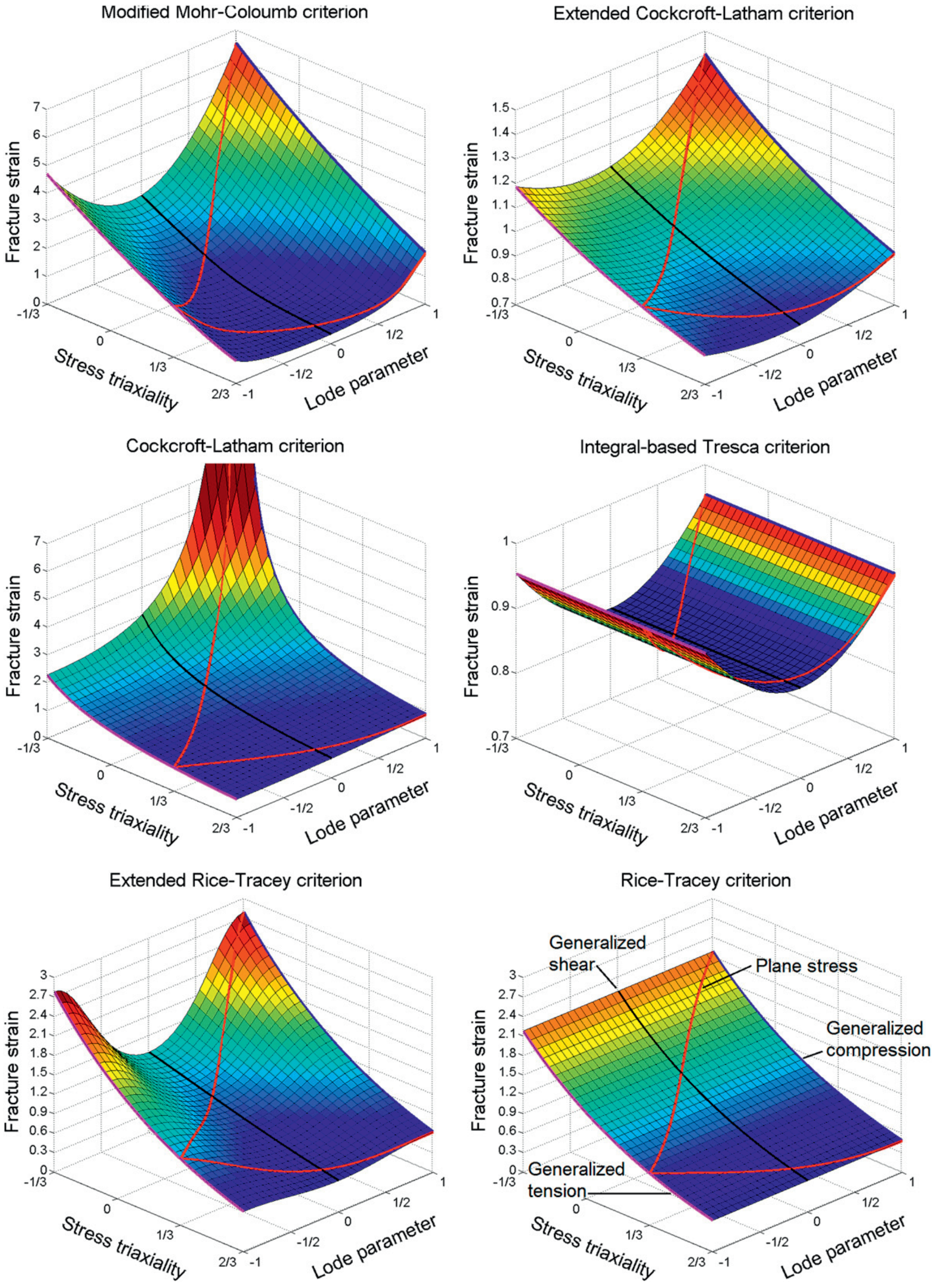

Fig. 8. Calibrated fracture surfaces in the $(\sigma^*,\mu,\bar{\varepsilon}_f^p)$ space assuming proportional loading. The plane stress, generalized shear ($\mu=0$), generalized tension ($\mu=-1$) and generalized compression ($\mu=+1$) loci are also plotted for comparison. Note that the range of the fracture strain differs significantly in the various plots.

5. Evaluation of the fracture criteria

5.1. Ductility as function of stress state

The predicted fracture surfaces as function of the stress state $\bar{\varepsilon}_f^p(\sigma^*,\mu)$ for the six calibrated criteria are displayed in Fig. 8. The figures also show the fracture loci for plane-stress, generalized shear ($\mu=0$), generalized tension ($\mu=-1$) and generalized compression ($\mu=+1$). The $\dot{\bar{\varepsilon}}_f^p$ and $\dot{\bar{\varepsilon}}_{\mathrm{avg}}^p$ values from the tension and the shear tests, see Table 4, were averaged and used in deriving the fracture surface of the MMC and ECL criteria, respectively. Even though Fig. 8 clearly displays the topology of the fracture surface obtained with the different fracture criteria, it is difficult to compare the experimental results to the predicted fracture strain using these surfaces. To compare the experimental data with the predicted fracture strains, 2D projections of the fracture loci shown in Fig. 8 are given in Fig. 9 together with the experimental values of the fracture strain $\bar{\varepsilon}_f^p$ versus average stress triaxiality

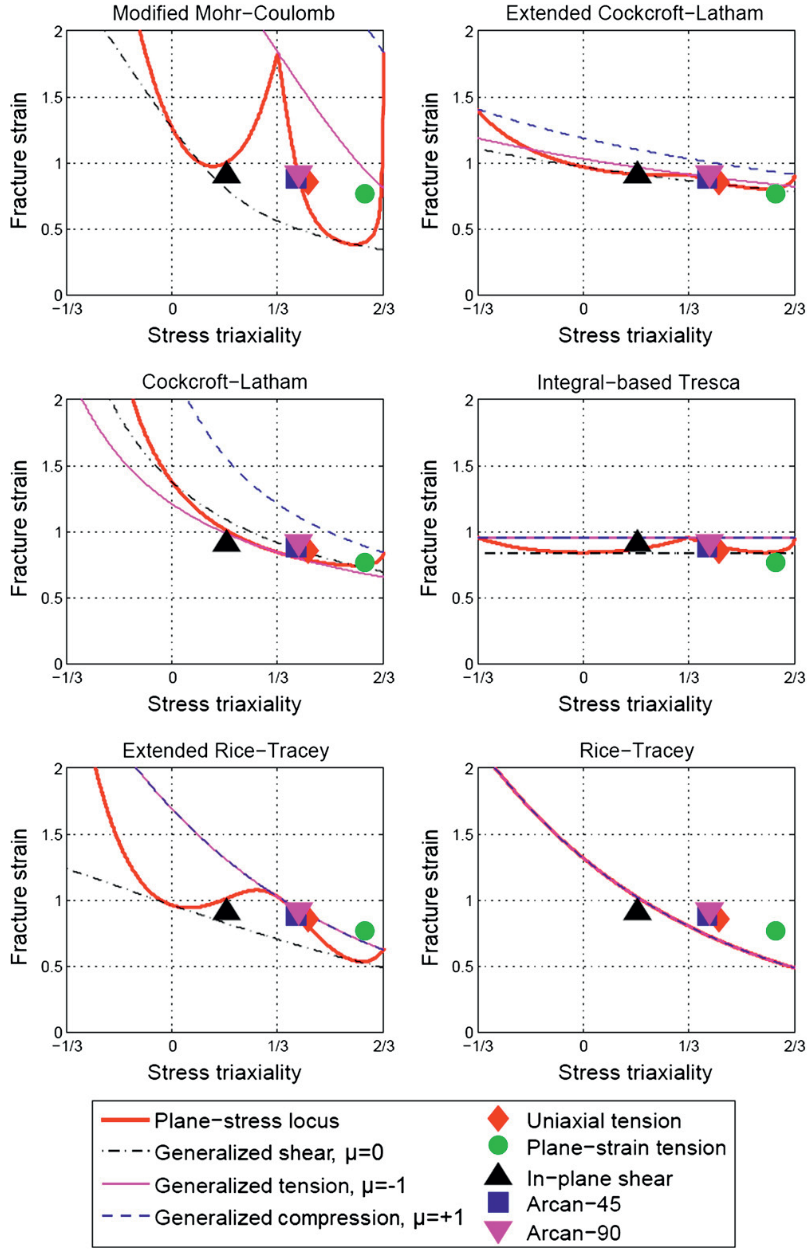

Fig. 9. Fracture loci in the $(\sigma^*,\bar{\varepsilon}^p)$ space for the different criteria plotted together with the experimental fracture strains.

σ^*_{avg} for the five tests. Since the stress states in the five test specimens are close to plane stress, cf. Fig. 5(a), the distance between the plane-stress fracture locus and the experimental fracture points gives an indication of the accuracy of the fracture criteria.

Figs. 8 and 9 show that the fracture surfaces of the MMC and the ECL criteria have similar shape, but $\bar{\varepsilon}^p_f$ spans over a considerably larger region for the MMC criterion. The reason is that a small change in the equivalent stress at fracture (as a function of σ^* and μ) results in a large change in fracture strain for the MMC criterion. On the other hand, for the ECL criterion a change in the plastic work per unit volume at fracture yields an almost proportional change in the fracture strain as long as the stress-state dependence parameter γ is close to unity. This is illustrated in Fig. 10(a) and (b). It is also shown in Fig. 10(a) that a certain work hardening is needed for large strains in the MMC criterion. If not, the predicted fracture strain will approach infinity as the hardening saturates. This is the reason for adding a tertiary term in the extended Voce rule. As can be seen from Figs. 8 and 9, the ERT criterion predicts a span in $\bar{\varepsilon}^p_f$ that lies between the MMC and the ECL criteria. The shape is not unlike the shape of the MMC and ECL criteria, but since the function $\omega(\mu)$ is symmetric around $\mu=0$, the ERT criterion does not, in contrast to the MMC and the ECL criteria, distinguish between generalized tension ($\mu=-1$) and generalized compression ($\mu=+1$).

The Cockcroft–Latham criterion yields a fracture surface that goes to infinity for a certain combination of (σ^*,μ), i.e., $3\sigma^*\sqrt{3+\mu^2}+3-\mu=0$. Two limiting cases are uniaxial compression $(\sigma^*,\mu)=(-\frac{1}{3},1)$, and biaxial compression $(\sigma^*,\mu)=(-\frac{2}{3},-1)$. This is seen from Eq. (16) with $\gamma=1$ and $\varphi=1$, and explains the higher values for $\bar{\varepsilon}^p_f$ compared to the ECL criterion in Fig. 8. The fracture surface obtained with the integral-based Tresca criterion is, on the other hand, not much affected by a variation of (σ^*,μ). This can be seen from Eq. (16) with $\gamma=1$ and $\varphi=0$, i.e., $\int\bar{\sigma}d\bar{\varepsilon}^p=W_C\sqrt{3+\mu^2}/2$. The fracture surface is only affected by the Lode parameter, and the minimum value of the plastic work per unit volume at fracture is 87% of the maximum value. From Fig. 10 it is seen that $\bar{\varepsilon}^p_f$ is approximately proportional to the plastic work per unit volume. It is noted that the integral-based Tresca criterion behaves very similar to the Freudenthal criterion which gives a constant value for the fracture strain. In contrast to the integral-based Tresca criterion, the Rice–Tracey criterion is Lode independent, as can be seen in Figs. 8 and 9. The criterion predicts a decreasing $\bar{\varepsilon}^p_f$ for increasing σ^*, as is evident from Fig. 9. The variation in $\bar{\varepsilon}^p_f$ is approximately in the same range as for the ERT criterion. In fact, the effect of the shear modification (κ_s) on the ERT fracture surface is lower values of $\bar{\varepsilon}^p_f$ in generalized shear ($\mu=0$) and higher values in axisymmetric stress states ($\mu=\pm1$). It can also be seen from Fig. 9 that the effect of the κ_s parameter is decreasing for increasing stress triaxiality.

5.2. *Damage accumulation*

The fracture loci depicted in Fig. 9 do not give information on the damage accumulation of the various criteria. In order to get information on the damage accumulation histories of the fracture criteria as well as an accurate measure of their predictions of fracture initiation, they were integrated in time using the actual stress and strain histories at the location of fracture in the different specimens. In the FE models, the element at the location of fracture initiation in the experimental tests was determined. The time histories of equivalent plastic strain $\bar{\varepsilon}^p(t)$ and the principal stresses, $\sigma_I(t)$,$\sigma_{II}(t)$,$\sigma_{III}(t)$, at the critical location were then used in the temporal integration of the damage evolution rule defined by the different fracture criteria. The time of fracture, t_f, was defined by the condition $D(t_f)=1$ and the corresponding fracture strain is determined as $\bar{\varepsilon}^p_f=\bar{\varepsilon}^p(t_f)$. The damage evolution as function of equivalent strain given by each fracture criterion is displayed in Fig. 11 for the uniaxial tension, plane-strain tension and in-plane shear tests, and in Fig. 12 for the modified Arcan tests. The fracture strain in each test found from the hybrid experimental–numerical procedure [25] is also displayed in Figs. 11 and 12. By inspecting the damage evolution curves in Figs. 11 and 12, it is clear that the MMC, ECL, CL and IT criteria gives an almost linear relation between damage and plastic strain. An exception is the MMC criterion when applied on the data from the uniaxial tension test. This anomaly is due to the fact that the MMC criterion initially predicts $\bar{\varepsilon}^p_f\approx1.8$, a value that decreases rapidly when σ^* increases after diffuse necking, thus changing the size in the damage increment, see Eq. (14). The RT and ERT criteria display an exponential increase in damage as function of equivalent strain in all the tests. This damage evolution is similar in shape as the evolution of the area void fraction in a DP600 steel investigated by Avramovic-Cingara et al. [32].

5.3. *Prediction of fracture initiation*

As seen from Fig. 11, all criteria give reasonable predictions of the fracture strain in the uniaxial tension and in-plane shear tests, while the MMC, ERT and RT criteria predicts a too low ductility in

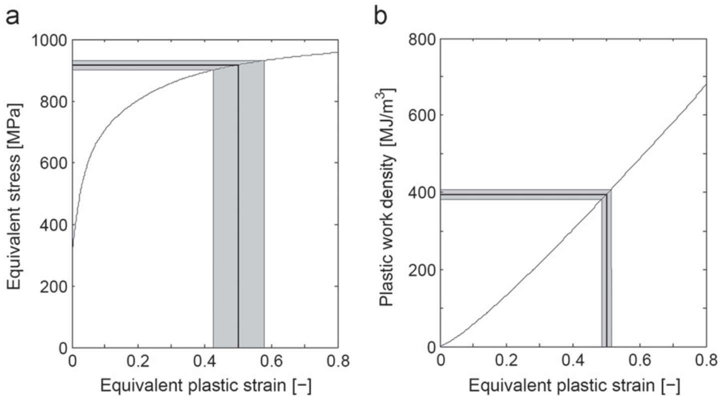

Fig. 10. (a) Flow stress versus equivalent plastic strain ($\bar{\sigma}-\bar{\varepsilon}^p$) and (b) plastic work per unit volume versus equivalent plastic strain, ($\int\bar{\sigma}d\bar{\varepsilon}^p-\bar{\varepsilon}^p$). The figure illustrates how small variations in the flow stress and plastic work density influence the equivalent plastic strain to different degrees.

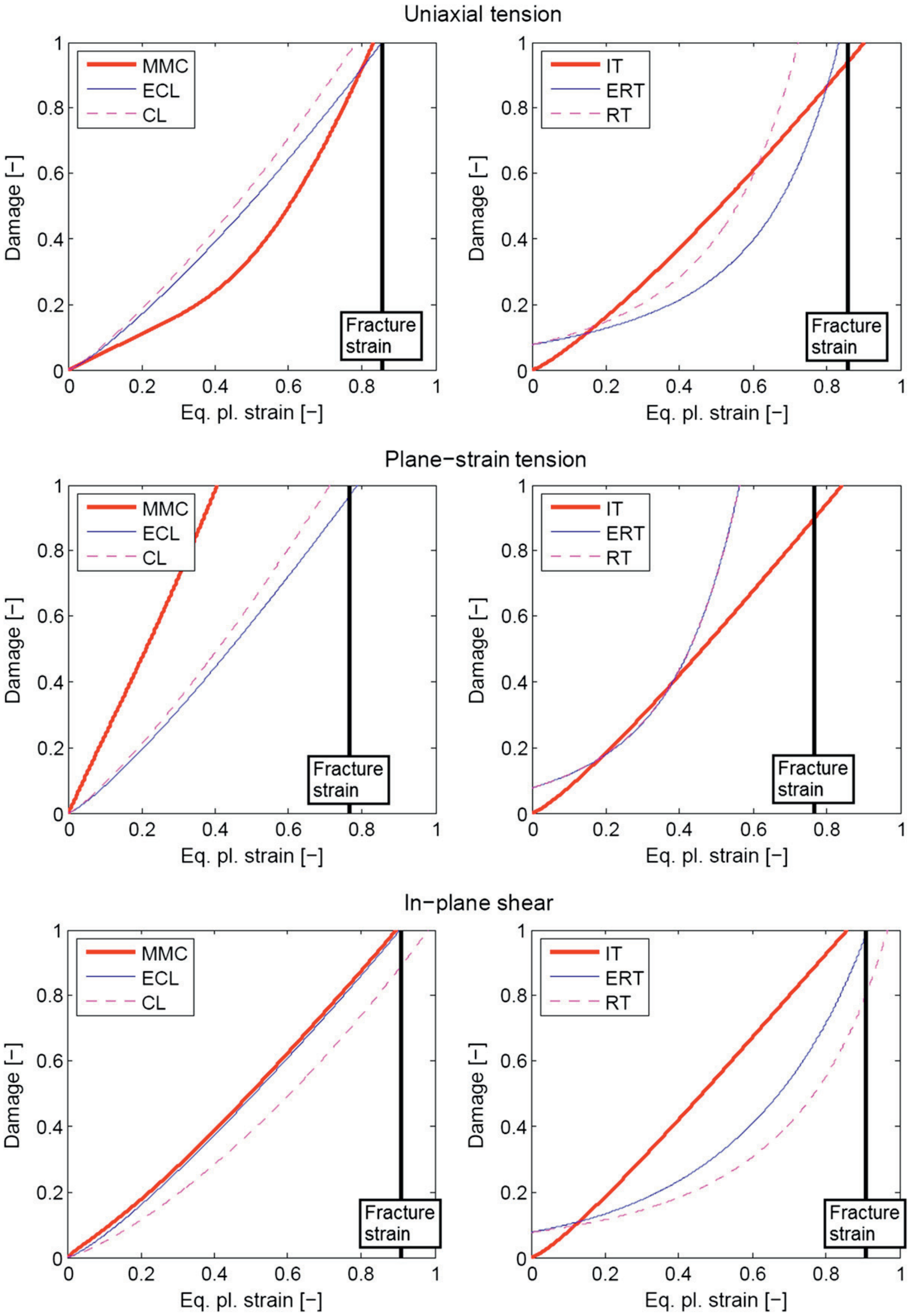

Fig. 11. Damage evolution as function of equivalent plastic strain for the various fracture criteria in the uniaxial tension, in-plane shear and plane-strain tension tests. The fracture strain determined for each test through the experimental–numerical analysis is also plotted.

the plane-strain tension test. This is coherent with the plane-stress fracture loci of the fracture criteria depicted in Fig. 9. As displayed in Fig. 12, the various fracture criteria predicts reasonable well the ductility in the Arcan-45 test, except the MMC criterion which predicts very high ductility. Fig. 5(a) shows that the Arcan-45 test lies exactly on the generalized tension

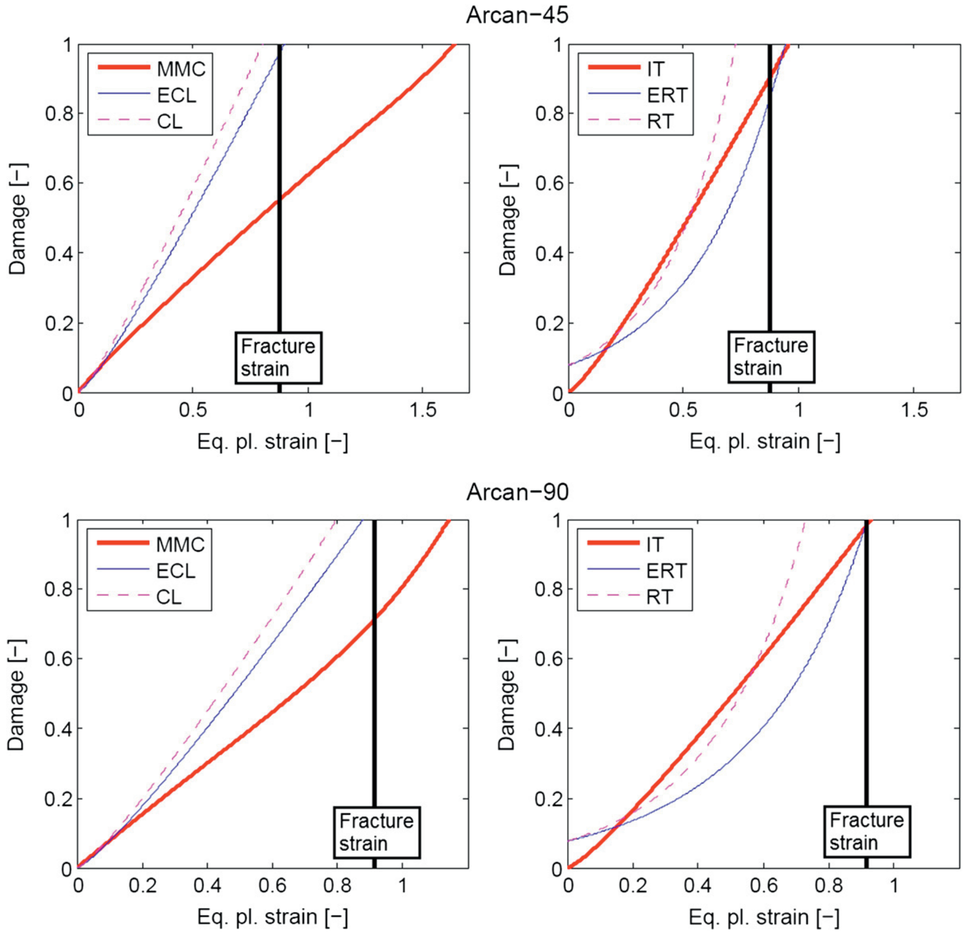

Fig. 12. Damage evolution as function of equivalent plastic strain for the various fracture criteria in the modified Arcan tests together with the fracture strains determined for both tests through the experimental–numerical analysis.

locus ($\mu = -1$), and close to the plane stress locus. By inspecting the generalized tension and plane stress fracture loci for the MMC criterion in Fig. 9, it is observed that these two loci predict significantly different ductility for the stress triaxiality value of the Arcan-45 test. This illustrates the difficulty of evaluating fracture initiation in the (σ^*,$\bar{\varepsilon}^p$) space unless the experimental tests are placed exactly on or at least very close to the plane-stress locus. In the Arcan-90 test, the MMC criterion predicts high ductility, the RT criterion predicts low ductility, and the other criteria give good predictions of the fracture initiation, as illustrated in Fig. 12. The root-mean-square error (RMSE) for the predicted fracture strain relative to the measured one was calculated for each of the criteria. This resulted in; $\text{RMSE}_{\text{MMC}}=0.393$, $\text{RMSE}_{\text{ECL}}=0.023$, $\text{RMSE}_{\text{CL}}=0.080$, $\text{RMSE}_{\text{IT}}=0.060$, $\text{RMSE}_{\text{ERT}}=0.096$ and $\text{RMSE}_{\text{RT}}=0.153$. The high RMSE for the MMC criterion mainly stems from the large deviation in the Arcan-45 test. It is further noted that the ECL, CL and IT criteria yields lower RMSEs than the ERT and RT criteria, and that the ECL criterion clearly gives the lowest RMSE of all criteria.

A second calibration of the fracture criteria were also carried out on the dataset extracted by DIC measurements from the surface of the 16 tests described in Section 2. The average values of stress triaxiality and Lode parameter, σ^*_{avg} and μ_{avg}, and the fracture strain, $\bar{\varepsilon}_f$, for the 16 tests are found in [21]. In the assessment of the criteria using this dataset, the strain-rate sensitivity of the material was not included in the MMC criterion and the various criteria in the ECL criterion. In the fitting process, an optimization procedure was applied where the RMSE for each criterion was minimized. Fig. 13 presents the plane-stress loci of the fracture criteria in the $\sigma^*-\bar{\varepsilon}^p$ space compared to the experimental data. Since the surface of the specimens is in a state of plane stress, the plane-stress locus gives a good estimation of the fracture strains obtained with the various criteria. As can be seen from Fig. 13, the ECL criterion once again captures the experimental results well, having a RMSE of 0.083 which is approximately half of the RMSEs for the CL, IT and ERT criteria and approximately one third of the RMSEs for the MMC and RT criteria.

6. Discussion

The fracture criteria adopted in this study are based on different assumptions. The MMC criterion starts from the stress-based MC criterion, which is used to find the fracture strain for a given stress state, and then a damage accumulation rule is used to

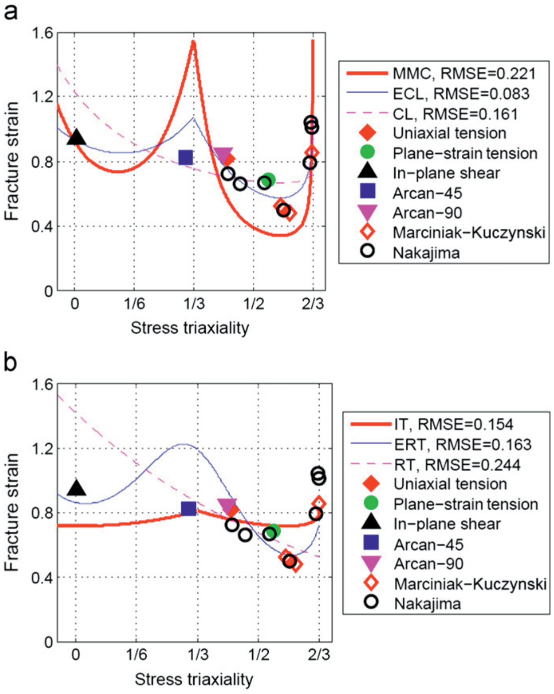

Fig. 13. $\bar{\varepsilon}_f$ versus σ^*_{avg} from all tests derived from optical measurements on the surface of the specimens compared with the fracture loci obtained with the (a) MMC, ECL and ERT criteria and (b) the IT, ERT and RT criteria. The root-mean-square error (RMSE) for each criterion is given in the legend.

calculate the damage evolution. Since the MC criterion is stress based, small changes in stress state may induce large changes in fracture strain as seen in Fig. 10(a). In the ECL criterion, damage is driven by the plastic power multiplied by an amplification factor accounting for the stress state. Depending on the amplification factor, the criterion may be made more or less sensitive to the stress state. The ERT criterion is based on a damage growth expression given by Eq. (18). In contrast to the MMC and ECL criteria, the constitutive parameters are not included in the expression of the predicted fracture strain, $\bar{\varepsilon}_f$.

When the fracture criteria were applied on the data obtained from the centre of the specimens [25], which displayed low variation in fracture strain, the intrinsic properties of the MMC, ERT and RT criteria forced the criteria to predict a large range in fracture strain. This is in contrast to the ECL, CL and IT criteria, which predicted a small variation in fracture strain within the stress range of the experiments. On the other hand, when the criteria were applied on the dataset obtained from the surface of the specimens [21,25], including the formability tests which had a significant variation in ductility, the ECL criterion displayed a large range in $\bar{\varepsilon}_f$, while the CL and IT criteria displayed low variation in $\bar{\varepsilon}_f$ as these criteria do not include the stress-state dependency parameter γ. The MMC criterion exaggerates the range of $\bar{\varepsilon}_f$ also when compared to the data from the formability tests, while the ERT criterion captured the trend from the experiments, but displayed too high ductility in uniaxial tension and too low ductility in biaxial tension. The RT criterion predicted a decreasing $\bar{\varepsilon}_f$ for increasing σ^* and did not capture the high ductility in the biaxial tension tests. Of the six criteria, the ECL criterion seems to be the only one that predicts a low range in fracture strain on the dataset with low variation in ductility and at the same time predicts a large variation in fracture strain on the dataset that displayed a large variation in ductility. It is noted that the ECL criterion is a function of three parameters while the other criteria are functions of two parameters (MMC and ERT) or one parameter (CL, IT and RT). Thus, the ECL criterion has more flexibility compared to the other criteria. It is further noted that the ERT criterion would fit better to the two datasets if the ψ parameter also was considered as a variable, and that the MMC criterion would predict a smaller range in fracture strain, thus fitting the fracture datasets better, if a larger work hardening for large strains was assumed.

While the MMC and ECL criteria predict an almost linear damage evolution as function of equivalent plastic strain, the exponential shape of the damage evolution in the ERT and RT criteria is similar to the evolution of the porosity as function of through-thickness strain of the DP600 steel investigated by Avramovic-Cingara et al. [32]. If the fracture criteria were to be used in numerical simulations in combination with e.g., the element erosion technique, the shape of the damage evolution is not important as long as the fracture criterion is not coupled to the constitutive equation. If the fracture criterion is coupled to the constitutive equation, the MMC, ECL, CL and IT criteria would introduce too much softening in the early stages of simulation due to the nearly linear relation between the damage and the equivalent strain, while the ERT and the RT criterion would give a more realistic softening. Xue and Wierzbicki [33] employed a damage evolution rule similar to Eq. (14) in simulations of three-point bending and compact tension specimens made of aluminium alloy 2024-T351. In that study an exponential weakening factor in the coupling with the stress tensor was introduced. The weakening factor made it possible to reduce the influence of damage on the constitutive relation for small and moderate strains.

7. Conclusions

Several ductile fracture criteria have been evaluated against the fracture characteristics of the dual-phase steel Docol 600DL. The fracture properties of the material were determined through a hybrid experimental-numerical procedure from the centre of specimens employed in uniaxial tension, plane-strain tension, in-plane shear and modified Arcan tests. In addition, a dataset from the surface of the specimens based on DIC measurements were applied, and in this dataset the fracture parameters from Marciniak–Kuczynski and Nakajima formability tests were included. The experimental–numerical dataset from the centre of the specimens, which is suitable for calibration of numerical models with 3D solid elements, showed moderate variation of the fracture strain as a function of the stress triaxiality. On the other hand, the dataset from the surface of the specimens, which is suitable for calibration of numerical models with plane-stress elements, displayed a significant drop in fracture strain in the formability tests exposed to plane-strain tension loading. All the tests displayed macroscopically ductile behaviour with large strains before fracture, $\bar{\varepsilon}_f \gg 0.1$, and by inspection of the fracture surfaces of selected specimens in a scanning electron microscope, it was found that all specimens displayed ductile fracture with dimples.

The modified Mohr–Coulomb (MMC) fracture criterion and novel extended versions of the Cockcroft–Latham (ECL) and Rice–Tracey (ERT) fracture criteria, all of which explicitly accounts for the stress triaxiality and the Lode dependence on the damage evolution, were evaluated for the material. The predicted fracture strain as function of stress-state for each criterion was evaluated, and it was found that the MMC fracture criterion predicts a large variation in the fracture strain as function of stress-state due to the coupling with the flow stress. The ECL criterion displays the same shape as the MMC criterion in the $(\sigma^*,\mu,\bar{\varepsilon}^p)$ space, but can adjust the range of predicted fracture strain through a fitting parameter. Both the MMC and ECL criteria predicts a larger fracture strain in generalized compression than in generalized tension for the same stress triaxiality, while the ERT criterion predicts the same fracture strain for the two axisymmetric stress states. The range of the fracture strain obtained with the ERT criterion is less than the range found by the MMC criterion. The damage accumulation for the MMC and ECL criterion is almost linear with the equivalent plastic strain, while it is exponential for the ERT criterion. The shape of the exponential damage evolution is similar to the evolution of void area fraction in a comparable steel. For each criterion, the predicted and experimental equivalent strains at fracture initiation were compared for the two datasets, respectively from the centre and surface of the specimens. Due to its flexibility, the ECL criterion proved to give a good representation of both datasets, while somewhat larger deviations were observed using the ERT and the MMC criteria.

Acknowledgements

The financial support of this work from the Structural Impact Laboratory (SIMLab), Centre for Research-based Innovation (CRI) at the Norwegian University of Science and Technology (NTNU), is gratefully acknowledged. Thanks are also given to Dr Ida Westermann for providing the SEM investigations.

References

[1] Shima S, Oyane M. Plasticity theory for porous metals. Int J Mech Sci 1976;18(6):285–91.
[2] Gurson AL. Continuum theory of ductile rupture by void nucleation and growth, 1. Yield criteria and flow rules for porous ductile media. J Eng Mater Technol 1977:2–15.
[3] Rousselier G. Ductile fracture models and their potential in local approach of fracture. Nucl Eng Des 1987;105(1):97–111.
[4] Lemaitre J, Chaboche J-L. Mechanics of solid materials. Cambridge University Press; 1990.
[5] Lemaitre J. A course on damage mechanics. Springer-Verlag; 1992.
[6] Freudenthal AM. The inelastic behaviour of solids. New York: Wiley; 1950.
[7] Cockcroft MG, Latham DJ. Ductility and the workability of metals. J Inst Met 1968;96:33–9.
[8] Wilkins ML, Streit RD, Reaugh JE. Cumulative-strain-damage model of ductile fracture: simulation and prediction of engineering fracture tests. in: technical report UCRL-53058, Lawrence Livermore National Laboratory, 1980.
[9] Johnson GR, Cook WH. Fracture characteristics of three metals subjected to various strains, strain rates, temperatures and pressures. Eng Frac Mech 1985;21(1):31–48.
[10] Wierzbicki T, Bao Y, Lee Y-W, Bai Y. Calibration and evaluation of seven fracture models. Int J Mech Sci 2005;47(4–5):719–43.
[11] McClintock FA. Criterion for ductile fracture by growth of holes. J Appl Mech 1968;35:363–71.
[12] Rice JR, Tracey DM. On the ductile enlargement of voids in triaxial stress fields. J Mech Phys Solids 1969;17:201–17.
[13] Imad A, Wilsius J, Abdelaziz MN, Mesmacque G. Experiments and numerical approaches to ductile tearing in an 2024-T351 aluminium alloy. Int J Mech Sci 2003;45(11):1849–61.
[14] Besson J, Madi Y, Motarjemi A, Koçak M, Martin G, Hornet P. Crack initiation and propagation close to the interface in a ferrite–austenite joint. Mater Sci Eng, A 2005;397(1–2):84–91.
[15] Ko D-C, Kim B-M, Choi J-C. Prediction of surface-fracture initiation in the axisymmetric extrusion and simple upsetting of an aluminum alloy. J Mat Proc Technol 1996;62(1–3):166–74.
[16] Dørum C, Laukli HI, Hopperstad OS. Through-process numerical simulations of the structural behaviour of Al–Si die-castings. Comput Mater Sci 2009;46(1):100–11.
[17] Lee HC, Choi JS, Jung KH, Im YT. Application of element deletion method for numerical analyses of cracking. J Achi Mater Manuf Eng 2009;35(2):154–61.
[18] Kane A, Børvik T, Berstad T, Benallal A, Hopperstad OS. Failure criteria with unilateral conditions for simulation of plate perforation. Eur J Mech A Solids 2011;30(4):468–76.
[19] Bao Y, Wierzbicki T. On fracture locus in the equivalent strain and stress triaxiality space. Int J Mech Sci 2004;46:81–98.
[20] Barsoum I, Faleskog J. Rupture mechanisms in combined tension and shear—experiments. Int J Solids Struct 2007;44(6):1768–86.
[21] Gruben, G, Vysochinskiy, D, Coudert, T, Reyes, A, Lademo, O-G Determination of ductile fracture parameters of a dual-phase steel by optical measurements. Submitted for possible publication 2012.
[22] Lode W. Versuche fiber den Einfluß der mittleren Hauptspannung auf das Fließen der Metalle Eisen, Kupfer und Nickel. Z Phys: A 1926;36:913–39.
[23] Wylllie DC. Foundations on rock. Second ed. London: E & FN Spon; 1999.
[24] Bai Y, Wierzbicki T. Application of extended Mohr–Coulomb criterion to ductile fracture. Int J Fract 2010;161(1):1–20.
[25] Gruben G, Fagerholt E, Hopperstad OS, Børvik T. Fracture characteristics of a cold-rolled dual-phase steel. Eur J Mech A Solids 2011;30:204–18.
[26] SSAB (2009) Docol DP/DL cold reduced dual-phase steels. Swedish steel AB. (accessed: 27.04.2012). 〈http://www.ssab.com/Global/DOCOL/datasheets_docol/en/201_Docol%20DP%20DL.pdf〉.
[27] LSTC, LS-DYNA keyword user's manual, version 971, Livermore Software Technology Corporation, 2007.
[28] Clausing DP. Effect of plastic strain state on ductility and toughness. Int J Fract 1970;6(1):71–85.
[29] Mohr D, Ebnoether F. Plasticity and fracture of martensitic boron steel under plane stress conditions. Int J Solids Struct 2009;46(20):3535–47.
[30] Dunand M, Mohr D. Hybrid experimental–numerical analysis of basic ductile fracture experiments for sheet metals. Int J Solids Struct 2010;47(9): 1130–43.
[31] Nahshon K, Hutchinson JW. Modification of the Gurson Model for shear failure. Eur J Mech A Solids 2007;27(1):1–17.
[32] Avramovic-Cingara G, Saleh CAR, Jain MK, Wilkinson DS. Void nucleation and growth in dual-phase steel 600 during uniaxial tensile testing. Metall Mater Trans: A 2009;40(13):3117–27.
[33] Xue L, Wierzbicki T. Ductile fracture initiation and propagation modeling using damage plasticity theory. Eng Fract Mech 2008;75(11):3276–93.

Part IV

G. Gruben, O.S. Hopperstad and T. Børvik

Simulation of ductile crack propagation in dual-phase steel

Submitted for possible journal publication

Simulation of ductile crack propagation in dual-phase steel

G. Gruben[*], O.S. Hopperstad and T. Børvik

Structural Impact Laboratory (SIMLab), Centre for Research-based Innovation (CRI) and Department of Structural Engineering, Norwegian University of Science and Technology, Rich. Birkelands vei 1A, NO-7491 Trondheim, Norway

---

Abstract

The modified Mohr-Coulomb and the extended Cockcroft-Latham fracture criteria are used in explicit finite-element simulations of ductile crack propagation in a dual-phase steel sheet. The sheet is discretized using tri-linear solid elements and the element erosion technique is used to model the crack propagation. The numerical results are compared to quasi-static experiments conducted with five types of specimens (uniaxial tension, plane-strain tension, shear, 45° and 90° modified Arcan) made from a 2 mm thick sheet of the dual-phase steel Docol 600DL. The rate-dependent J_2 flow theory with isotropic hardening was used in the simulations. The predicted crack paths and the force-displacement curves were quite similar in the simulations with the different fracture criteria. Except for the 45° modified Arcan test, the predicted crack paths were in good agreement with the experimental findings. The effect of using a high-exponent yield function in the prediction of the crack path was also investigated, and it was found that this improved the crack path prediction for the 45° modified Arcan test. In simulations carried out on finite element models with a denser spatial discretization, the prediction of localized necking and crack propagation was in better accordance with the experimental observations. In four out of five specimen geometries, a through-thickness shear fracture was observed in the experiments. By introducing strain softening in the material model and applying a dense spatial discretization, the slant fracture mode was captured in the numerical models. This did not give a significant change in the global behaviour as represented by the force-displacement curves.

Keywords: Crack propagation; Dual phase steel; Ductile fracture; Finite element method; Material instability

---

[*] Corresponding author. Tel.: + 47-73-59-46-87; fax: + 47-73-59-47-01

E-mail address: gaute.gruben@ntnu.no (G. Gruben).

1 Introduction

Various approaches exist for predicting fracture initiation and crack propagation numerically. In problems involving ductile materials, the failure criteria typically express the deterioration of the material by an accumulative damage variable. The damage variable can be coupled with the constitutive relation of the material as in porous plasticity models e.g. Shima and Oyane (1976), Gurson (1977) and Rousselier (1987), or continuum damage mechanics models Lemaitre and Chaboche (1990) and Lemaitre (1992). Another approach is utilized in the uncoupled models e.g. Cockcroft and Latham (1968), Wilkins (1980) and Johnson and Cook (1985), where the damage has no effect on the constitutive behaviour. As most ductile failure criteria depend on the deformation history of the material, it is crucial that the numerical model is capable of describing the deformation processes taking place before fracture in order to make good predictions of fracture initiation and crack propagation. Stochastic variations of the material characteristics may also influence the results to various degrees depending on the problem at hand see e.g. Fyllingen et al. (2007) and Dørum et al. (2009). A range of techniques exists for simulating crack propagation with the Finite Element (FE) method, such as node splitting (Kazutake, 1999; Komori, 2005), cohesive elements (Needleman, 1990; Tvergaard and Hutchinson, 1996; Tvergaard, 2001), remeshing adaptivity (Bouchard et al., 2000; Mediavilla et al., 2006) and the extended finite element method (Areias, 2006; Fagerström and Larsson, 2006). A method that is relatively simple, robust and has proven to work well in problems involving large deformations is the element erosion technique (Xue and Wierzbicki, 2008; Fagerholt et al., 2010; Kane et al., 2011). In this technique, the load-carrying capacity of the element is set to zero when the fracture criterion is met at one or more integration points.

In this study, the modified Mohr-Coulomb criterion presented by Bai and Wierzbicki (2010) and the extended Cockcroft-Latham criterion presented by Gruben et al. (2012a) are used in explicit finite-element simulations of ductile crack propagation in a low-strength, high-hardening dual-phase steel, and the results are compared to experimental data reported by Gruben et al. (2011). The fracture criteria have been calibrated and assessed with respect to fracture initiation for this material by

Gruben et al. (2012a), under assumption of J_2 flow theory. In this study, the fracture criteria are evaluated with respect to fracture propagation by use of FE analyses in combination with the element erosion technique. It is shown that the fracture criteria neither give large variations in the predicted crack paths nor in the force-displacement curves. Additionally, the effect of the shape of the yield surface on the fracture propagation is studied. It is shown that for moderate changes in the yield surface, the effects on the crack paths and the force-displacement curves are small in the single-mode fracture tests. In the mixed-mode fracture test, a higher exponent of the yield surface gives a better prediction compared to the experiment. The effects of mesh refinement and coupled damage have also been studied. Mesh refinement leads to more rapid strain localization, followed by a more rapid global failure. By including strain softening on the dense-mesh FE models, it is possible to numerically predict slant fracture, but this has virtually no influence on the global response in terms of force-displacement curves.

2 Experiments

Gruben et al. (2011) carried out experiments on specimens in the low range of stress triaxiality. A description of the material and test set-ups is briefly repeated here, together with supplementary information on the material from more recent studies. Finally, a detailed discussion of the crack propagation in the various test specimens is given.

The material used was a low-strength, high-hardening, steel of type Docol 600DL. This is a dual-phase steel where the ferrite gives the formability and the martensite gives the strength. The chemical composition of the material is given in Table 1. Fig. 1 displays the geometry of the four different specimen types used (uniaxial tension, plane-strain tension, in-plane shear and modified Arcan) in the rectangular coordinate system defined by the base vectors $(\mathbf{e}_X, \mathbf{e}_Y, \mathbf{e}_Z)$. Fig. 2 displays the test set-up for the modified Arcan tests. Here the angle β was set to respectively $45°$ and $90°$. All specimens were cut from a 2 mm thick steel sheet with the longitudinal axis in the rolling direction, except the uniaxial tension tests, which also were cut 45° and 90° to the rolling direction in order to determine the anisotropy of the material. The experiments were conducted under displacement control at room temperature with pre-necking strain rates in the vicinity of 10^{-3} s^{-1}. The force and displacement were measured in each test by the hydraulic test machine. In addition, an in-house digital image correlation (DIC) code (Fagerholt, 2012) was used to measure the displacement fields and to calculate the strain fields. The force-displacement $(F-u)$ curves from typical tests in the five set-ups are given in Fig. 3. The fracture characteristics of the material were determined at the through-thickness centre of the specimens by a hybrid experimental-numerical procedure, and at the surface of the specimens by utilizing an experimental procedure based on optical measurements. It was found that the variation in ductility as function of stress state was rather small for the stress states investigated and that the range in ductility was somewhat larger on the surface than in the centre. It was further argued that for calibration of 3D solid elements the data from the through-thickness centre should be used, while for plane-stress elements the data from the surface are relevant. A more recent study of the fracture surfaces of the specimens by scanning electron microscopy (Gruben et al., 2012a) showed that the governing fracture mechanism in the tests was nucleation, growth and coalescence of microvoids. This observation is supported by a study comprising formability tests on material from the same batch (Gruben et al., 2012b). The formability tests revealed that the material displays a significantly lower ductility in plane-strain tension than in uniaxial tension and biaxial tension.

Table 1 Chemical composition of Docol 600DL (in wt. %),(SSAB, 2009).

C	Si	Mn	P	S	Al_{tot}
0.10	0.40	1.50	0.010	0.002	0.040

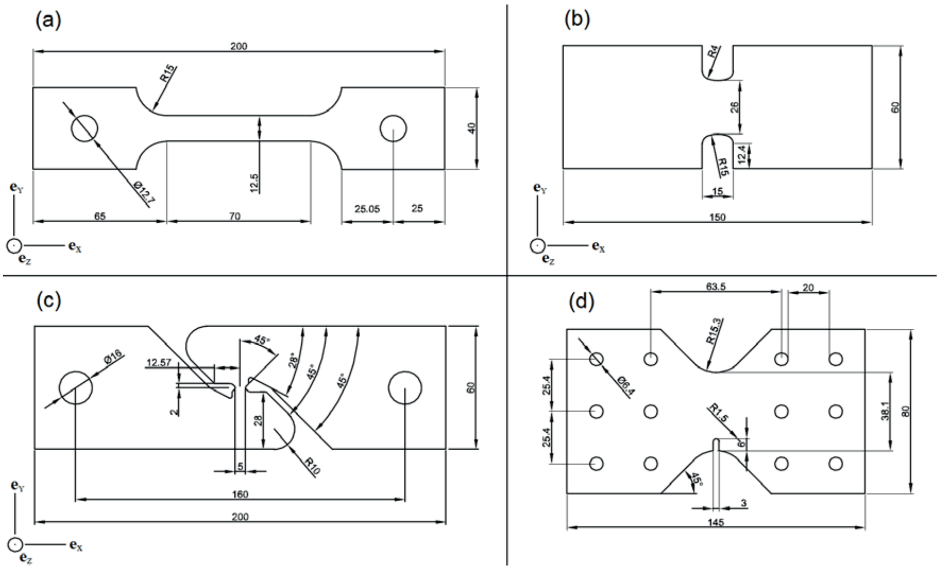

Fig. 1 Geometry of the test specimens (in mm): (a) uniaxial tension, (b) plane-strain tension, (c) in-plane shear, and (d) modified Arcan (Gruben et al., 2011).

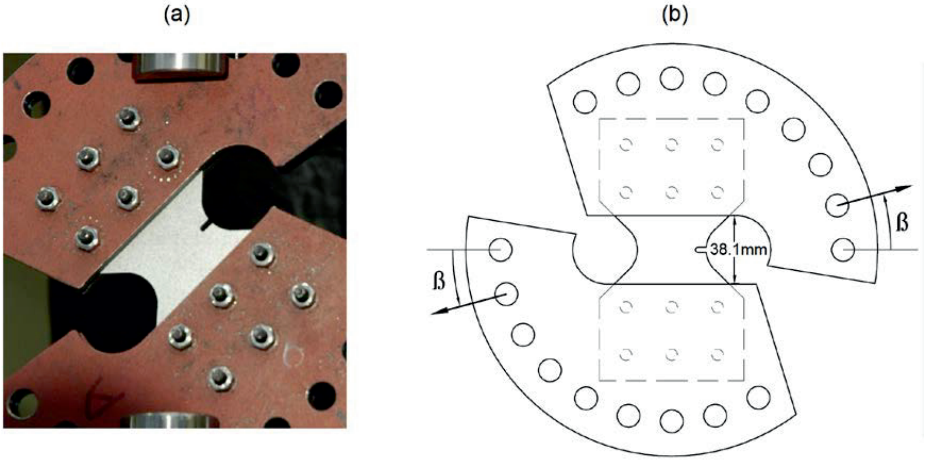

Fig. 2 (a) Modified Arcan test set-up with $\beta = 45°$, and (b) sketch of brackets with specimen defining the loading direction β (Gruben et al., 2011).

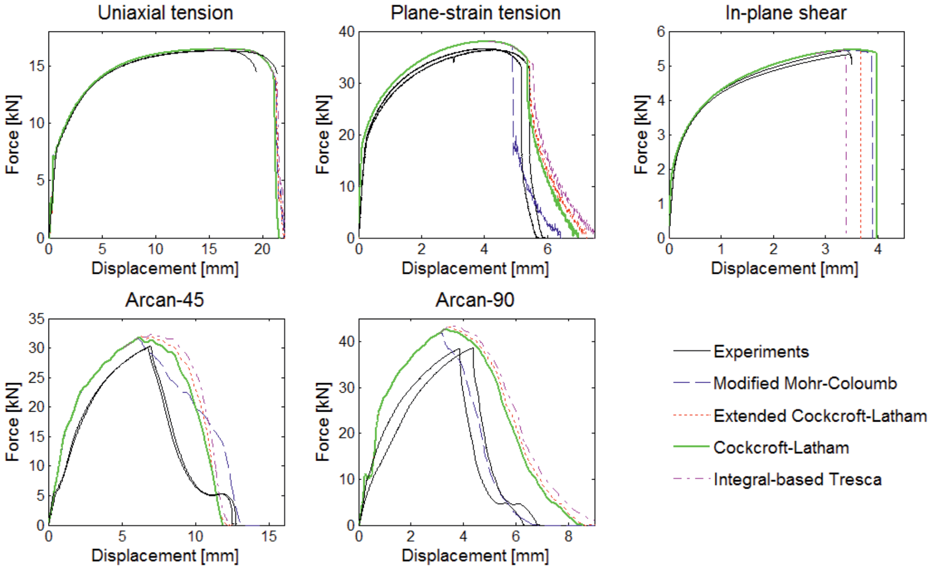

Fig. 3 Force-displacement curves from experiments and simulations with J_2 flow theory and the four fracture criteria.

Three parallels of the uniaxial tension test were performed on specimens cut 0°, 45° and 90° to the rolling direction (a total of nine tests). Only small variations could be observed in the force-displacement curves, and the plastic flow was assumed to be nearly isotropic (Gruben et al., 2011). The force-displacement curves from two typical tests in the rolling direction are displayed in Fig. 3. From the hardening law fitted to one of the tests in the rolling direction, see Equation (1) below, the Considère criterion estimates diffuse necking to take place at an equivalent plastic strain of 0.18 (ignoring strain rate effects). By using Hill's criterion, localized necking is predicted at an equivalent plastic strain of 0.31. The equivalent strain at fracture, henceforth called the fracture strain, was calculated from DIC measurements and found to be 0.82. The characteristic element size used in the DIC analysis was 0.9 mm. This value of the fracture strain refers to fracture initiation and is valid for the surface of the specimen. The fracture strain has also been determined by calculating the logarithmic strain from the area reduction at fracture, i.e. $\varepsilon_f = \ln(A_0 / A_f)$, (Johnsen, 2009). Here A_0 is the initial cross-section area, and A_f is the projection of the cross-section area in the $\mathbf{e}_X$

plane at global failure. This approach resulted in a fracture strain $\varepsilon_f = 0.80$ for the same specimen. For the nine tests an average fracture strain $\varepsilon_f = 0.81$ with a standard deviation of 0.03 was found from the area reduction measurement. This indicates that the material is isotropic also with respect to fracture. From the finite element analysis conducted by Gruben et al. (2011), it was found that the equivalent plastic strain at fracture is larger at the centre of the specimen. Here it is estimated to 0.85 by a finite element analysis using 3D solid elements with a characteristic size of 0.38 mm. This simulation did however not capture the through-thickness shear bands observed in the specimens during testing. Experimentally the crack appeared within these shear bands in all nine tests, but three different modes were observed, see Fig. 4(a-c). The first mode is a slant fracture where the fracture plane is approximately $43°$ to $\mathbf{e}_Z$, see Fig. 4(b), with in-plane direction parallel to $\mathbf{e}_Y$, as illustrated in Fig. 4(c). Only one of the nine tests exhibited this mode. The second mode is a double through-thickness shear mode, or a V-mode; see Fig. 4(b). The V-mode displayed in-plane localization inclined approximately $22°$ in all three tests where it appeared; cf. specimen 2 in Fig. 4(c). The third mode is a combination of the two first modes, and was observed in five tests. In all the tests fracture initiated at the in-plane centre of the neck and propagated to the edges in less than 0.5 s corresponding to a actuator displacement increment $\Delta u = 0.017$ mm.

In the plane-strain tension tests, fracture initiated in the in-plane centre of the specimens and propagated roughly perpendicular to the loading direction; see Fig. 4(d). At the centre of the specimen, a rough surface was observed, but shear-lips were present also in this area as illustrated in Fig. 4(d). A slant fracture mode occurred as the crack propagated towards the edges, as displayed in Fig. 4(d). As seen in Fig. 3, global failure occurred approximately $\Delta u \approx 0.47$ mm after fracture initiation.

The in-plane shear tests displayed a flat crack surface through the sheet thickness as illustrated in Fig. 4(e). Due to rotation of the material during the test, the crack surface was rotated approximately 22° with respect to $\mathbf{e}_X$, as displayed in Fig. 4(f). The fracture mode was the same in both tests, and global failure occurred in the instant that fracture initiated. From the force-displacement curves in Fig. 3, a small drop in force is observed in the last part of the curve. This may be due to a combination of material softening and a small reduction of the shear area.

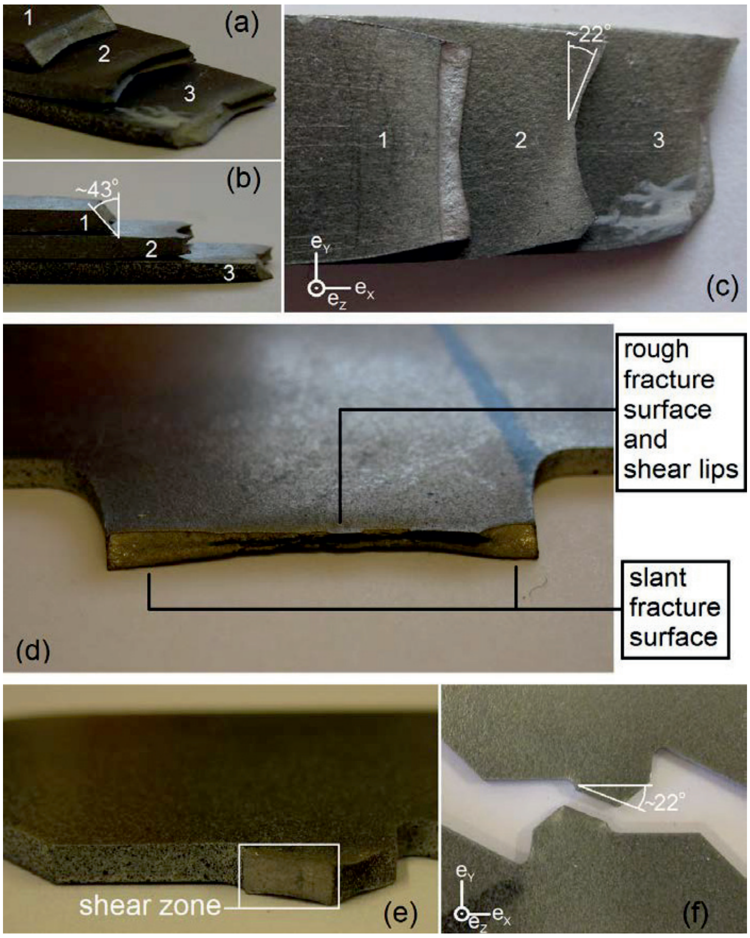

Fig. 4 Pictures (a), (b) and (c) display the three different modes of fracture in the uniaxial tension tests, where "1" is the slant fracture, "2" is the V-mode and "3" is a combination of "1" and "2". Picture (d) shows fracture in the plane-strain tension test, while picture (e) and (f) illustrate fracture in the in-plane shear test.

The two Arcan-45 tests were exposed to a mixed-mode loading resulting in a curved crack path as displayed in Fig. 5(a). Fracture initiated in the notch root in a V-mode at a displacement $u \approx 7$ mm, but after less than 1 mm propagation it turned into a slant fracture mode, see Fig. 5(b). In both tests the crack then propagated uniformly in this mode until $u \approx 11.5$ mm. Here the crack got arrested and did not propagate further until the specimen failed completely at $u \approx 12.5$ mm. In this last $1/10$ of the crack path, in-plane shear localization occurred and produced a flat-fracture mode similar to the one observed in the in-plane shear tests, see Fig. 5(a) and Fig. 5(b). The point of fracture initiation can be seen in the force-displacement curve in Fig. 3 as a sudden drop in the force level when $u \approx 7$ mm, while the in-plane shear failure can be seen as the drop in force at $u \approx 12.5$ mm. At $u \approx 10$ mm, the force curve flattens out. This may be due to a kinematic artefact stemming from the rotation of the specimens and the brackets.

For the Arcan-90 tests, fracture initiated in the centre of the notch and propagated in a direction nearly parallel to $\mathbf{e}_Y$ as displayed in Fig. 5(c). In both tests, the crack was in a V-mode at first. The tests exhibited this mode as the crack propagated approximately 2 mm and 5 mm, respectively, as displayed in Fig. 5(d). The crack then switched to a slant fracture mode. In one of the tests, the crack propagated in the same slant fracture mode until global failure, while in the other test the crack switched to the other shear band halfway through the specimen, see Fig. 5(d). As can be seen from the force-displacement curves in Fig. 3, the force level flattens out in a similar way as in the Arcan-45 tests in the last part of the curve before global failure. From the DIC analysis it was observed that the crack propagation velocity decreased in the final stages of the test. The reduction of the crack propagation velocity might be due to the rotation of the specimens and brackets.

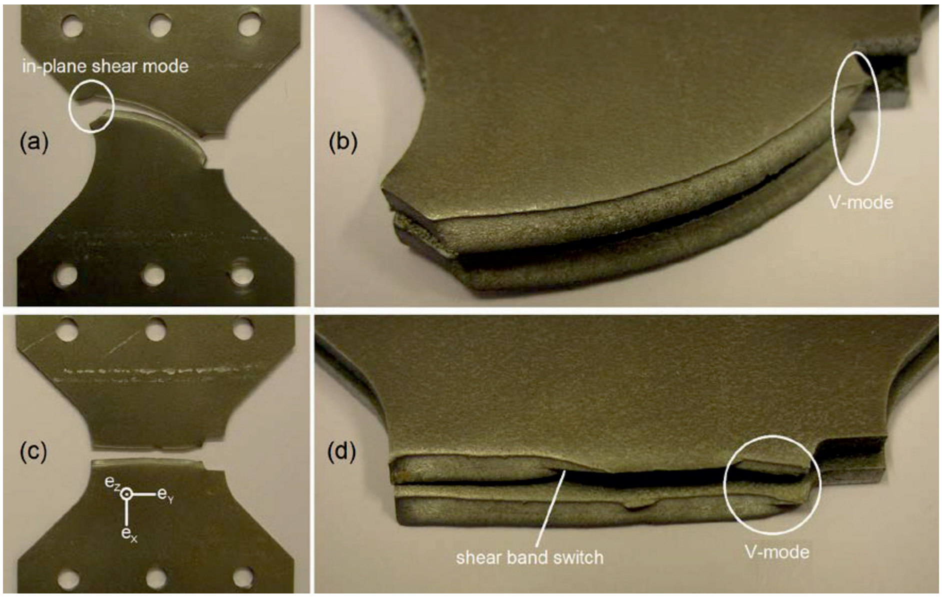

Fig. 5 Pictures (a) and (b) display fracture of the Arcan-45 tests. Fracture started in a V-mode and then propagated in a slant fracture mode before the crack got arrested and finally ended in a flat shear mode. Pictures (c) and (d) display fracture of the Arcan-90 tests, where fracture initiated in a V-mode and continued in a slant fracture mode to global failure.

3 Numerical modelling

The spatial discretizations and boundary conditions of the FE models in this study are based on the models described by Gruben et al. (2011). In this study the simulations were run with the explicit solver of LS-DYNA version 971 (LSTC, 2007) with the constitutive model and fracture criteria described below implemented as a user-defined material model. The modified Arcan specimens were discretized with a random element distribution in the $\mathbf{e}_Z$ plane, while the other models had a structured mesh. The discretizations are displayed in Fig. 6. In all these models nine elements were used over the thickness, giving an initial element height of 0.22 mm. Table 2 gives the in-plane element size in the different models. In addition, models of the uniaxial tension, plane-strain tension and in-plane shear tests with finer discretizations were made. Fig. 7 illustrates the discretization of the uniaxial tension specimen with finer mesh. A small geometric trigger was used in this model to obtain diffuse necking in the centre of the zone with finer mesh. Since the elements undergo large deformations before fracture, the initial aspect ratio of the elements in the fracture zone of the uniaxial tension and plane-strain tension dense-mesh models were made so that the elements had a nearly cubic shape at the point of failure. The final density of the mesh in the dense-mesh models was found at the point where a denser mesh did not produce a significant change in the fracture mode. The FE models with the fine discretization have 18 elements in the thickness direction, corresponding to an initial height of 0.11 mm. The characteristic in-plane element sizes of the dense-mesh FE models are summed up in Table 2. The modified Arcan tests were not simulated with denser mesh, since the computational time was too long. The elements used in the coarse-mesh FE models in Sections 5.1 and 5.2 below were eight-node, trilinear solids with selectively reduced integration (Type 2 in LS-DYNA). Due to computational costs, eight-node, trilinear solid elements with reduced integration (Type 1 in LS-DYNA) were utilized in the FE models in Section 5.3 below. The simulation time was reduced by a factor 10^5 to maintain a reasonable computational time. Control with the kinetic energy and comparisons with simulations using implicit time-integration showed that this time scaling is admissible. The reference strain rate $\dot{\varepsilon}_0$ in Equation (1) was increased by a factor 10^5 to maintain the correct proportions due to the time scaling.

Table 2 Characteristic initial in-plane element size used in the FE models with coarse and fine discretization (in mm).

Uniaxial tension	Plane-strain tension	In-plane shear	Modified Arcan
0.50	0.46	0.10	0.36
0.077	0.065	0.064	—

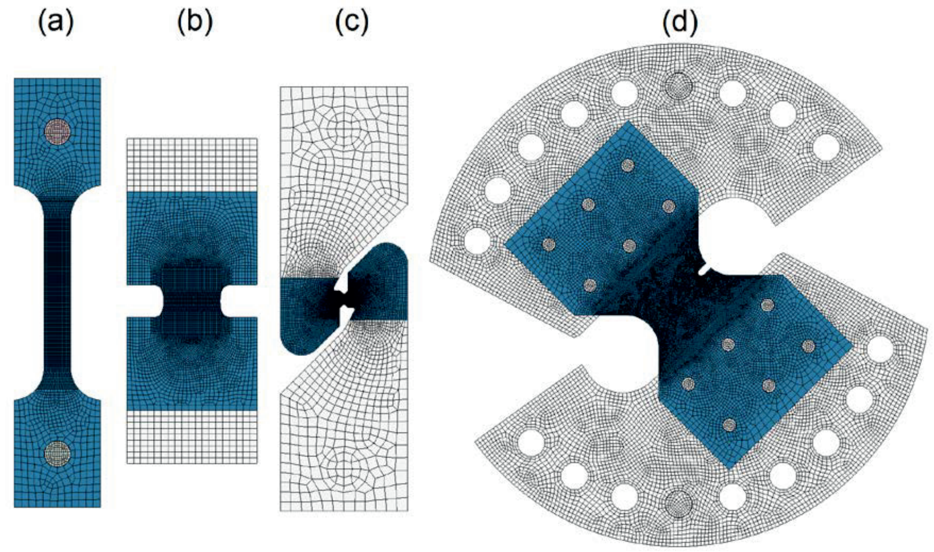

Fig. 6 Finite element meshes of the test specimens: (a) uniaxial tension, (b) plane-strain tension, (c) in-plane shear and (d) modified Arcan.

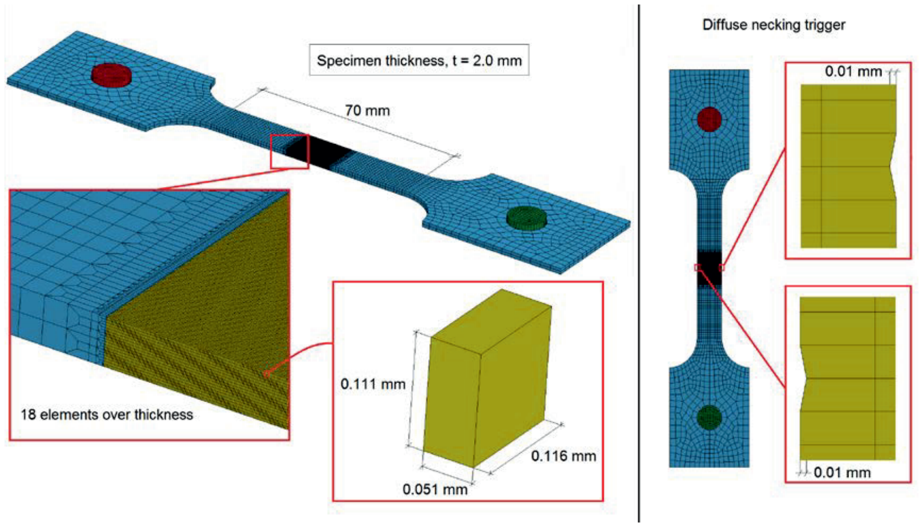

Fig. 7 Discretization of uniaxial tension specimen with dense mesh.

3.1 Constitutive relation

3.1.1 Work hardening

The work hardening of the material was fitted to the extended Voce rule with a multiplicative viscosity-hardening law as (Gruben et al., 2012a)

$$\bar{\sigma} = \left(\sigma_0 + \sum_{i=1}^{3} Q_i \left(1 - \exp(-C_i \bar{\varepsilon}^p)\right) \right) \cdot \left(1 + \frac{\dot{\bar{\varepsilon}}^p}{\dot{\varepsilon}_0} \right)^q \tag{1}$$

where $\bar{\sigma}$ is the equivalent stress defined by the yield criterion, σ_0 is a material parameter representing the yield stress, and Q_i and C_i $(i = 1, 2, 3)$ are material parameters governing in turn the primary, secondary and tertiary hardening of the material. The parameters q and $\dot{\varepsilon}_0$ are material constants defining the strain-rate sensitivity of the material. The strain-rate sensitivity was not investigated experimentally for this material, but reasonable values for dual-phase steels (Tarigopula et al., 2006; Curtze, 2009) were used. The hardening parameters were found by a fit of the Cauchy stress – logarithmic plastic strain curve from the uniaxial tension test up to diffuse necking, and by inverse modelling for large strains using the uniaxial tension and in-plane shear tests. Table 3 gives the work-hardening parameters for the material.

Table 3 Parameters in the rate-dependent extended Voce hardening model in the uncoupled (top row) and coupled (bottom row) damage model. The high value of $\dot{\varepsilon}_0$ is due to time-scaling.

σ_0 [MPa]	Q_1 [MPa]	C_1	Q_2 [MPa]	C_2	Q_3 [MPa]	C_3	$\dot{\varepsilon}_0$ [s^{-1}]	q
286.2	287.9	34.93	341.1	5.00	6000	0.01	100	0.005
287.1	297.1	33.72	339.4	4.63	6000	0.01	100	0.005

3.1.2 Yield function

The plastic flow of the material was found to be virtually isotropic, and the modelling in the previous studies (Gruben et al., 2011; Gruben et al., 2012a) was done by the J_2 flow theory. It was discussed by Gruben et al. (2011) that a high exponent yield function might give a better description of the material's yield surface. As part of this study, a high-exponent, isotropic yield function, as proposed by Hershey (1954), was used to investigate the effect of the shape of the yield surface. The equivalent stress is expressed as

$$\bar{\sigma} = \sqrt[2k]{\frac{1}{2}\left((\sigma_I - \sigma_{II})^{2k} + (\sigma_{II} - \sigma_{III})^{2k} + (\sigma_{III} - \sigma_I)^{2k}\right)} \tag{2}$$

where σ_i, $i = I, II, III$ are the principal stresses ordered so that $\sigma_I \geq \sigma_{II} \geq \sigma_{III}$, and the integer k controls the curvature of the yield surface. The von Mises yield surface is obtained with $k = 1$, while $k \to \infty$ gives the Tresca yield surface. Previous studies (Hutchinson, 1964a, b) have indicated that the yield surface of BCC materials is closer to the von Mises yield surface, while for FCC materials it is closer to the Tresca yield surface. The Docol 600DL material mainly consists of ferrite (BCC) and martensite (BCT).

3.1.3 Damage coupling

In general, material softening is the macroscopic effect of adiabatic heating or micro-porosity during plastic deformation. Xue and Wierzbicki (2008) presented a phenomenological model introducing material softening due to micro-porosity as

$$\boldsymbol{\sigma} = \tilde{\boldsymbol{\sigma}}(1 - D^{\beta}) \tag{3}$$

where $\tilde{\boldsymbol{\sigma}}$ is the effective Cauchy stress assumed to act on the un-deteriorated matrix material, $0 \leq D \leq D_C$ is the damage parameter and $\beta > 0$ is the weakening factor controlling the influence of the accumulated damage on the Cauchy stress tensor $\boldsymbol{\sigma}$. If D is larger than the critical value, D_C, the element loses its load-carrying capacity and is deleted. In this study, it was chosen that the element is deleted if D_C is reached in one integration point, even if the element have several integration points. Further, the D_C value was set to 0.995 to ensure that the equivalent stress of the damaged material always stayed positive in the beginning of the next time increment. Note that the limiting value $\beta \to \infty$ leads to no coupling between the damage and the Cauchy stress tensor. The damage coupling procedure used is similar to the methodology described by de Borst (2004), i.e. $\tilde{\boldsymbol{\sigma}}$ is substituted in all constitutive relations.

3.2 Fracture criteria

3.2.1 The modified Mohr-Coulomb criterion

The Mohr-Coulomb fracture criterion is expressed in the stress space as

$$\tau + c_1\sigma_n = c_2 \tag{4}$$

where τ is the shear stress and σ_n is the normal stress at fracture on the critical plane of the material. The material constant c_1 is often referred to as the friction, while c_2 is the cohesion. An alternative formulation of the Mohr-Coulomb criterion is

$$\frac{\phi\left(3\sigma^*\sqrt{3+\mu^2}-3-\mu\right)+6}{3\sqrt{3+\mu^2}}\bar{\sigma}_{VM} = C \tag{5}$$

where

$$\phi = \frac{2c_1}{\sqrt{1+c_1^2}+c_1},\ 0 \le \phi \le 1, \quad \text{and} \quad C = \frac{2c_2}{\sqrt{1+c_1^2}+c_1} > 0$$

Here $\bar{\sigma}_{VM}$ is the von Mises equivalent stress, i.e. $k=1$ in Equation (2), while σ^* is the stress triaxiality and μ is the Lode parameter (Lode, 1926), defined as

$$\sigma^* = \frac{\sigma_I + \sigma_{II} + \sigma_{III}}{3\bar{\sigma}_{VM}}, \quad \mu = \frac{2\sigma_{II} - \sigma_I - \sigma_{III}}{\sigma_I - \sigma_{III}} \tag{6}$$

A modified version of the Mohr-Coulomb criterion for ductile fracture was introduced by Bai and Wierzbicki (2010). This modified version utilizes a calculated fracture strain that depends on the stress state, $\bar{\varepsilon}_f^p = \bar{\varepsilon}_f^p(\boldsymbol{\sigma})$. Gruben et al. (2012a) estimated the fracture strain $\bar{\varepsilon}_f^p$ by replacing $\bar{\sigma}_{VM}$ in Equation (5) with the expression for the work hardening, Equation (1). In the case of a Hershey yield function, a modification is needed to have consistency between the constitutive relation and the fracture criterion. It can be shown that the relation between the von Mises equivalent stress and the Hershey effective stress from Equation (2) is expressed by the Lode parameter, μ, and the integer k as

$$\bar{\sigma}_{VM} = \frac{\sqrt{3+\mu^2}}{\sqrt[2k]{\frac{(1+\mu)^{2k}+(1-\mu)^{2k}+2^{2k}}{2}}}\bar{\sigma} \tag{7}$$

In order to estimate the fracture strain, $\bar{\varepsilon}_f^p$, the equivalent stress, $\bar{\sigma}$, in Equation (7) is replaced with the expression from Equation (1), and the resulting expression for $\bar{\sigma}_{VM}$ is inserted into Equation (5). The modified Mohr-Coulomb criterion (MMC) may then be expressed as a damage parameter

$$D = \int_0^{\bar{\varepsilon}^p} \frac{d\bar{\varepsilon}^p}{\bar{\varepsilon}_f^p} \tag{8}$$

where fracture initiates when D equals unity.

3.2.2 The extended Cockcroft-Latham criterion

The extended Cockcroft-Latham (ECL) criterion was introduced by Gruben et al. (2012a), and is expressed as

$$D = \frac{1}{W_C}\int_0^{\bar{\varepsilon}^p} \left\langle \phi\frac{\sigma_I}{\bar{\sigma}} + (1-\phi)\left(\frac{\sigma_I - \sigma_{III}}{\bar{\sigma}}\right)\right\rangle^{\gamma} \bar{\sigma}\, d\bar{\varepsilon}^p \tag{9}$$

where $\langle\cdot\rangle$ is the Macaulay brackets and $W_C \geq 0$, $0 \leq \phi \leq 1$ and $\gamma \geq 0$ are the fracture parameters. The overall ductility of the material is defined through W_C, while ϕ weights the influence of the major principal stress and the maximum shear stress, and γ controls the strength of the stress-state dependence. As for the MMC criterion, fracture is assumed to initiate when D equals unity. The ECL criterion is a generalization of several other fracture criteria. By setting $\gamma = 1$ an integral-based representation of the Mohr-Coulomb criterion is obtained, where the special case $\gamma = 1,\ \phi = 0$ gives the Integral-based Tresca (IT) criterion (Gruben et al., 2012a). The combination $\gamma = 1,\ \phi = 1$ gives the Cockcroft-Latham (CL) criterion (Cockcroft and Latham, 1968), while $\gamma = 0$ gives the Freudenthal criterion (Freudenthal, 1950).

4 Calibration of fracture criteria

The fracture models presented in Section 3.2 were calibrated by Gruben et al. (2012a) under the assumption of J_2 flow utilizing the data from the centre of the specimens obtained by the hybrid experimental-numerical procedure conducted by Gruben et al. (2011). These calibrations were based on FE models with coarse mesh similar to the ones described in the beginning of Section 3, see Table 2. More calibrations based on the coarse-mesh FE models have been carried out with the Hershey yield function, using the same procedures as Gruben and co-workers (2011; 2012a). The in-plane shear test and the uniaxial tension test were used to calibrate the MMC, CL and IT criteria. For the ECL criterion, additional data from the plane-strain tension test were used, and the criterion was calibrated for yield functions with $k = 1,3,4$. Table 4 gives the results from the calibrations. The fracture strain loci in the $(\sigma^*, \bar{\varepsilon}_f^p)$ space defined by the various fracture criteria, assuming proportional loading and plane-stress, are displayed in Fig. 8 for $k = 1$ (J_2 flow theory) and $k = 4$. The exponent k in the yield function does affect the predicted fracture strain, especially for the MMC and the ECL criteria. For the MMC criterion, the $k = 4$ calibration led to a lower value of ϕ, which again led to lower dependency of the stress triaxiality, cf. Equation (5). In the ECL calibrations, it is seen from Table 4 that a higher value of k leads to a higher value of the stress-state dependency parameter, γ, which is followed by a larger range in the predicted fracture strain as function of stress state.

Table 4 Calibrated fracture parameters for Docol 600DL.

Fracture criterion	C / W_C	ϕ	γ
Modified Mohr-Coulomb ($k = 1$)	1037	0.208	—
Modified Mohr-Coulomb ($k = 4$)	1033	0.078	—
Extended Cockcroft-Latham ($k = 1$)	815	0.335	1.55
Extended Cockcroft-Latham ($k = 3$)	886	0.192	3.02
Extended Cockcroft-Latham ($k = 4$)	1035	0.0884	5.75
Cockcroft-Latham ($k = 1$)	725	1.000	1.00
Cockcroft-Latham ($k = 4$)	722	1.000	1.00
Integral-based Tresca ($k = 1$)	834	0.000	1.00
Integral-based Tresca ($k = 4$)	801	0.000	1.00
ECL, dense mesh ($k = 1$, $\beta = \infty$)	888	0.335	1.55
ECL, dense mesh ($k = 1$, $\beta = 6$)	1033	0.335	1.55

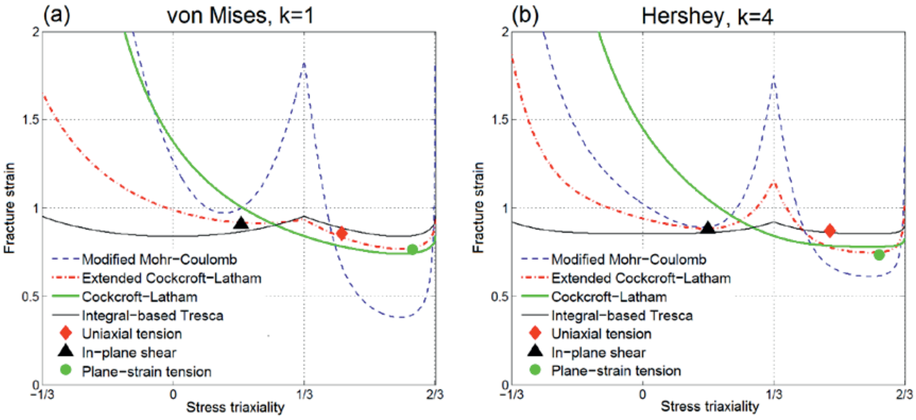

Fig. 8 Calibrated fracture locus $(\sigma^*, \bar{\varepsilon}_f^p)$ for the various fracture criteria under the assumption of proportional loading and plane stress. (a) J_2 flow theory $(k = 1)$, and (b) Hershey yield surface $(k = 4)$. The $(\sigma^*_{\text{avg}}, \bar{\varepsilon}_f^p)$ values for the three tests used in calibration of the ECL criterion are also plotted.

The dense-mesh FE simulations, with and without damage softening, displayed increased strain gradients compared to the coarse-mesh FE simulations. Accordingly, the fracture strain in the dense-mesh FE simulations increased, and it was found that the increase in ductility was approximately 7 % in the case without softening. To account for this, a new set of input parameters had to be determined for the dense-mesh FE models. Simulations of the uniaxial tension test were used to scale the parameters in the material model with the ECL criterion and the von Mises yield surface. It was assumed that the weighting between the major principal stress and the maximum shear stress, ϕ, as well as the stress-state dependence, γ, was unaffected by mesh refinement and damage softening. Thus, the only fracture parameter to be adjusted was the ductility parameter, W_C. It was found that the relation between D and $\bar{\varepsilon}^p$ in the uniaxial tension test simulation with uncoupled damage was given a good approximation by $D(\bar{\varepsilon}^p) = (\bar{\varepsilon}^p / \bar{\varepsilon}_f^p)^{1.25}$. Since W_C is used in normalizing D, cf. Equation (9), the W_C value was scaled by a factor $1.07^{1.25}$ to account for the increased fracture strain due to mesh refinement. For the case with dense mesh and coupled damage the calibration was more involved. Here it was postulated that the plastic work per volume up to fracture, $\int_0^{\bar{\varepsilon}_f^p} \bar{\sigma} d\bar{\varepsilon}^p$, is invariant to material softening. In order to ensure this, the work hardening parameters, σ_0, Q_i and C_i, had to be adjusted in addition to the ductility parameter, W_C, for a given weakening factor, β. This can be done by inverse modelling. However, a good estimate can be made based on the $D(\bar{\varepsilon}^p)$ relation in the uncoupled case. By using the latter approach, the work hardening curve for the damage softening material was readily produced by trial and error in MATLAB (2009). The resulting work-hardening curve for $\beta = 6$ is compared with the work-hardening curve of the material without damage softening in Fig. 9(a). The material with damage softening exhibits an increase in fracture strain of 13 % compared to the case with dense-mesh and uncoupled damage. Accordingly, the ductility parameter, W_C, was increased by a factor $1.13^{1.25}$. The weakening factor, β, was found by trial and error from simulations of the uniaxial tension and in-plane shear tests, and $\beta = 6$ was found to give reasonable results for both tests. The work-hardening parameters for $\beta = 6$ are summed up in Table 3, while the fracture parameters for the dense-mesh calibrations with and without damage softening are given in Table 4.

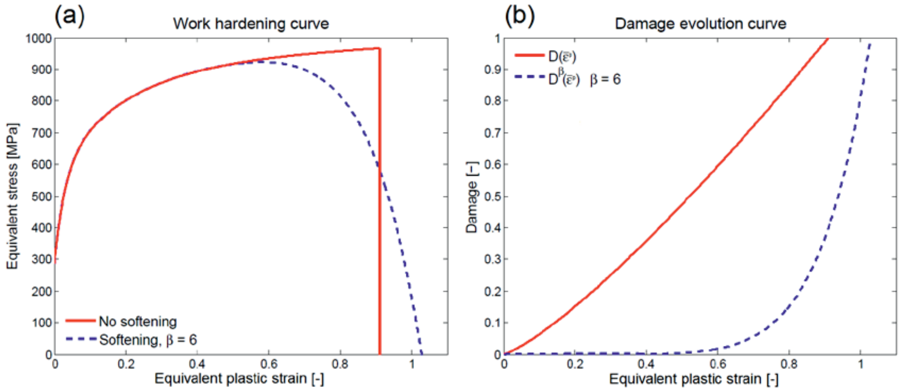

Fig. 9 (a) Work-hardening curves for uncoupled and coupled damage. The plastic work (area under the curves) is the same. (b) Damage evolution as function of equivalent strain without weakening factor, $D(\bar{\varepsilon}^p)$, and width weakening factor $D^\beta(\bar{\varepsilon}^p)$.

The damage evolution of the Docol 600DL material has not been studied experimentally. However, Avramovic-Cingara et al. (2009) determined the area void fraction as function of thickness strain for uniaxial tensile tests cut from a comparable DP600 steel-sheet. They found that the evolution of the area void fraction had an exponential shape with initial value 0.001 and final value 0.013. The near linear shape of $D(\bar{\varepsilon}^p)$ shown in Fig. 9(b) is not coherent with the evolution of the area void fraction in the comparable DP600 steel. On the other hand, the $D^\beta(\bar{\varepsilon}^p)$ curve from the damage softening calibration displays an exponential shape more similar to the evolution of the void area fraction. Another aspect of the damage-softening modelling in this study is the value of D_C. This value should represent the total damage on the material from microvoids, accumulation of micro-stresses at defects, and breaking of bonds. The study of Avramovic-Cingara et al. (2009) indicated that the microvoids contribution to D_C is very small, and in this perspective $D_C = 0.995$ is a very large value. This value is however used here, since the objective is to show how damage softening influences the numerical simulations. For other studies, a lower value of D_C should be considered. In this perspective it is noted that the critical void volume fraction in the Gurson model (Gurson, 1977) is often set in the vicinity of 0.15 for carbon steels (Anderson, 2005).

5 Simulation of crack propagation

5.1 Effect of fracture criterion

The effect of the fracture criterion on the crack propagation is presented in the following for the case of the coarse-mesh models, J_2 flow theory and uncoupled damage. The influence of the fracture criterion on the crack path in the five different tests is displayed in Fig. 10, which shows plots from the final stage of the simulation for each case. The displacement, u, corresponding to each plot is given in the figure. In the simulations of the uniaxial tension, plane-strain tension and modified Arcan tests, the elements in the thickness direction were deleted in a tunnelling mode; an example from the Arcan-45 test is given in Fig. 11(a). In the in-plane shear test all the elements through the thickness were deleted almost simultaneously.

The location of fracture initiation in the in-plane centre of the specimen was captured in the uniaxial and plane-strain tension tests by all fracture criteria, and the in-plane crack paths were similar to the experimental ones. Fracture initiates at the displacement where a significant drop in force level occurs in the $F-u$ curves in Fig. 3. In the simulations of the uniaxial tension test this drop occurred at almost the same displacement for all fracture criteria and fits well with the experimental values. This is in accordance with the fracture initiation prediction of the criteria found by Gruben et al. (2012a). In the simulations of the plane-strain tension test, the MMC criterion gave an early drop in force level, while the IT criterion predicted a somewhat late drop. The fracture initiation was predicted well by the ECL and CL criteria compared to the experimental results. This is also in accordance with the results from Gruben et al. (2012a). However, the crack propagation velocities were somewhat low in all simulations of the uniaxial tension, plane-strain tension and modified Arcan tests compared to the experiments.

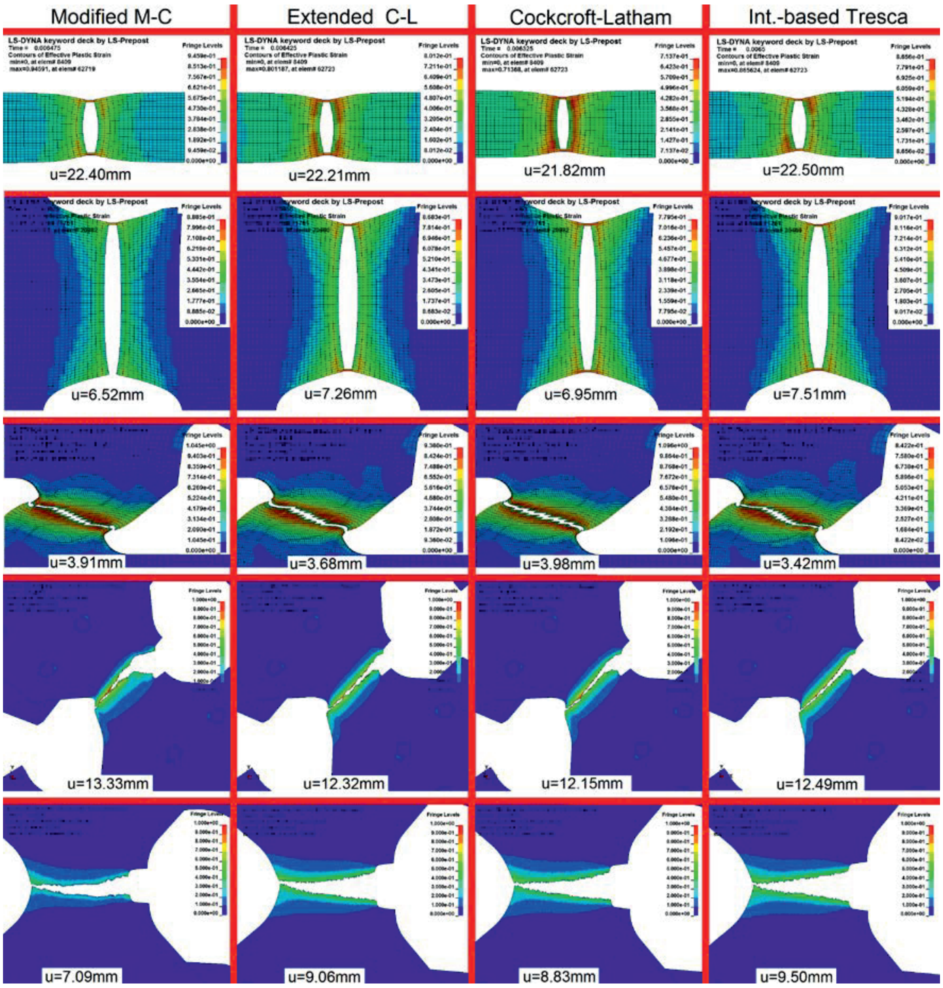

Fig. 10 Crack paths in simulations of different specimens with the four fracture criteria using J_2 flow theory. From top: uniaxial tension, plane-strain tension, in-plane shear, Arcan-45 and Arcan-90. The contours are equivalent plastic strain, and the displacement u corresponding to the given plot is marked in each case.

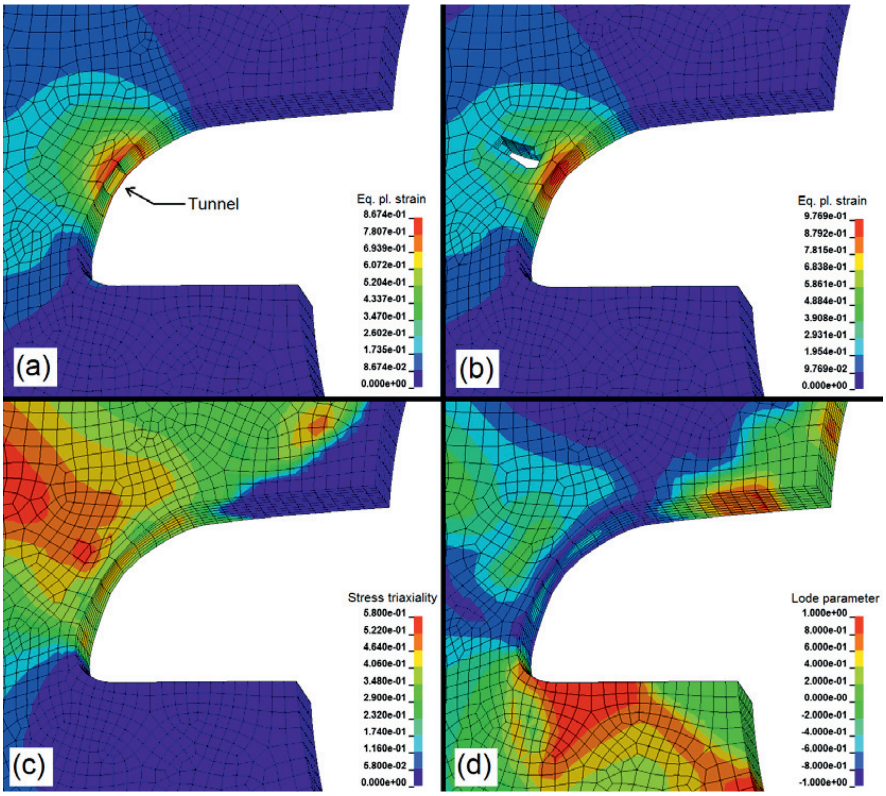

Fig. 11 Fracture initiation in Arcan-45 simulations: (a) Tunnelling effect observed in simulation with the ECL criterion and (b) elements eroded at a certain distance away from the expected fracture initiation point with the MMC criterion, (c) and (d) give the contour plots of respectively the stress triaxiality and the Lode parameter just before the first element is eroded in the simulation with the MMC criterion.

In the shear test, the global failure in the simulations occurred just after fracture initiation as observed in the tests. This can be seen in Fig. 3 where there is a sudden drop in the force level and no "tail" of $F-u$ curves. The displacement at global failure was slightly overestimated in the simulations with the MMC and CL criteria. As shown in Fig. 3, the experimental values are between the results from the simulations with the ECL and IT criteria. The angle between the crack path and $\mathbf{e}_X$ was approximately $21°$ in the simulations with the ECL and CL criteria and approximately $18°$ in those with the MMC and IT criteria. As illustrated in Fig. 4(f), this angle is approximately $22°$ in the experiment.

The displacement at final failure in the simulations of the Arcan-45 test was close to the experimental values, but the numerically obtained $F-u$ curves were not in agreement with the experimental curves after fracture initiation, as displayed in Fig. 3. Further, the simulation with the MMC criterion yielded an earlier drop in force level and a larger displacement at global failure than the simulations with the other criteria. Gruben et al. (2012a) showed that the fracture strain predicted by the MMC criterion at the assumed location of fracture initiation was larger than the experimentally determined value. In the present study, the drop in force level, which is related to fracture initiation, occurred significantly earlier in the simulation with the MMC criterion than in the experiments. This apparent paradox is explained by the fact that elements away from the root of the notch were eroded before the elements in the notch root when using the MMC criterion; see Fig. 11(b). This is in contrast to the experiments and simulations with the other fracture criteria where the crack initiated in the notch root, as displayed in Fig. 11(a). The MMC criterion predicted a very high ductility for uniaxial tension and low ductility for plane-strain tension, as illustrated in Fig. 8(a). The elements first eroded by the MMC criterion were practically in a plane-strain tension stress state with stress triaxiality $\sigma^* \approx 0.58$ and Lode parameter $\mu \approx 0$. This is illustrated in Fig. 11(c-d) where contours of the stress triaxiality and the Lode parameter are plotted just before the first elements are eroded. In the simulations of the Arcan-45 tests, the MMC criterion gave an $F-u$ curve with qualitatively better shape than those from simulations using the other fracture criteria, as displayed in Fig. 3. This may be due to the bilinear crack trajectory predicted by the MMC criterion which is more similar to the experimental crack path than the crack paths predicted by the other criteria, cf. Fig. 5(a) and Fig. 10. The bilinear crack path in the MMC simulation stems from the low ductility predicted by the criterion in plane-strain tension, which in the early stages of crack propagation drives the crack in a different direction than the direction with the largest equivalent strain.

In the simulations of the Arcan-90 test, the predicted crack paths using the various fracture criteria were very similar, as illustrated in Fig. 10. The fracture initiated in the root of the notch in all simulations, except in the simulation with the MMC criterion. Here elements with a certain distance away from the notch root were eroded first, as in the simulation of the Arcan-45 test; see Fig. 11(b). This premature erosion of elements led to an earlier drop in force level compared to the simulations with the other fracture criteria, as evident in Fig. 3. The simulation with the MMC criterion gave, however, a good prediction of the displacement at global failure, while the simulations with the other fracture criteria tended to overestimate this value.

5.2 Effect of exponent in yield function

Simulations were also carried out using the Hershey yield function given by Equation (2). Fig. 12 illustrates how the yield loci for $k = 3$ and $k = 4$ are placed between the von Mises yield locus $(k = 1)$ and the Tresca yield locus $(k \to \infty)$. The cases $k = 3, 4$ were chosen since BCC materials have proven to be closer to the von Mises than the Tresca yield surface (Hutchinson, 1964a). Results from the coarse-mesh FE models with the ECL criterion are presented in this section. Fig. 13 gives the results in terms of force-displacement curves. As can be seen, there is no notable difference when using a Hershey yield function in the simulations of the uniaxial tension test. In the simulations of the plane-strain tension test, a higher exponent tended to decrease the peak force and the displacement at fracture initiation and global failure. The opposite trend was observed in the simulations of the in-plane shear test where a higher exponent slightly increased the peak force and gave a significant increase in the displacement at global failure. Further, in the simulations of the Arcan-45 test, the force-displacement curves up to fracture initiation were not altered for increasing k values, but the displacement at global failure was increased. The simulations of the Arcan-90 test gave a trend in the force-displacement curves similar to the one observed for the plane-strain tension test; an increase in k gave a decrease in peak force and displacement at global failure.

In all but the simulations of the Arcan-45 test, the J_2 flow theory gave good predictions of the in-plane crack paths. With the Arcan-45 test as an important exception, the in-plane crack trajectory was not changed in the simulations with a Hershey yield function. However, for the Arcan-45 test, the simulation with $k = 4$ gave a curved crack path that to a higher extent resembles the experimental result. The crack trajectory in the simulation with $k=3$ ended between the crack paths obtained with $k=4$ and J_2 flow theory, but closer to the latter as displayed in Fig. 14(a-c). The change in the crack path may explain the larger displacement at global failure for higher k values in these simulations.

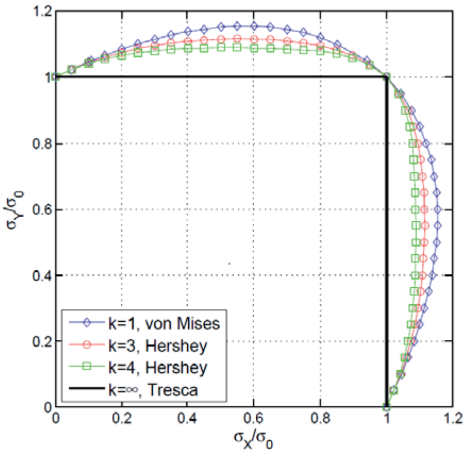

Fig. 12 First quadrant of normalized yield surfaces obtained with the Hershey yield function.

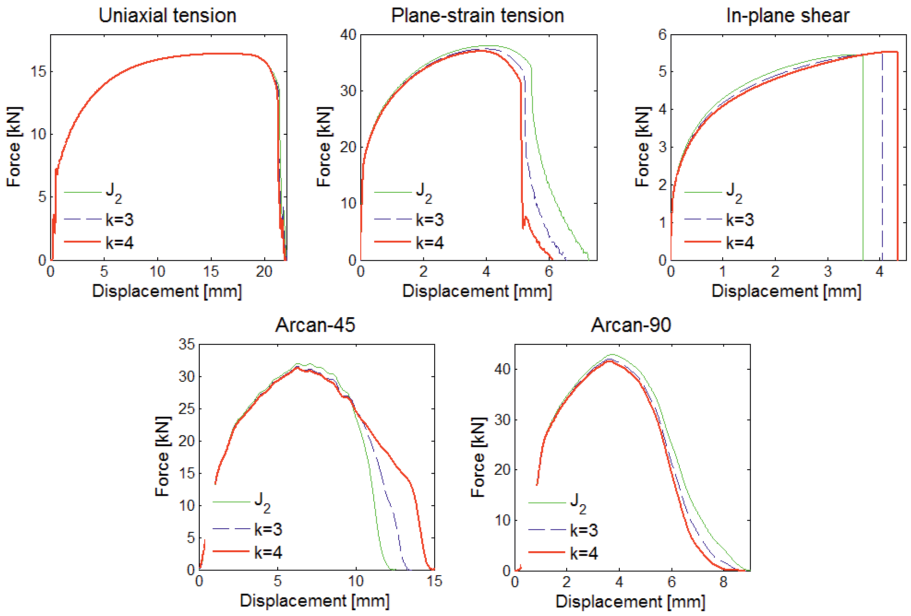

Fig. 13 Force-displacement curves from experiments and simulations using the extended Cockcroft-Latham criterion and yield functions with different k values.

In Fig. 14(d-f), a plot of the early stages of fracture is shown from the simulation with J_2 flow theory and the ECL criterion. The contours are equivalent plastic strain, stress triaxiality and Lode parameter. The elements that will be eroded later in the simulation are marked. From Fig. 14(e-f) it is evident that the stress triaxiality is higher and the absolute value of the Lode parameter is lower on the upper left-hand side of the crack path. Since the ECL criterion predicts lower ductility for higher hydrostatic stress and for low absolute values of the Lode parameter, this indicates that both the hydrostatic and the deviatoric stress state drive the crack to the upper left side in this simulation. However, as seen in Fig. 14(d), the equivalent plastic strain is largest in the direction of the crack path. From this we may conjure that the direction of the crack path is governed by the equivalent plastic strain in the simulation with J_2 flow theory. In the case with high exponent ($k = 4$) shown in Fig. 14(g-i), it is clear that the stress triaxiality and the Lode parameter drive the crack path in a different direction than the equivalent plastic strain, in the same manner as in the simulations using J_2 flow theory. In this case, however, it is seen that the crack path is governed by the stress state approximately the first $^{3}\!/_{5}$ of the total trajectory before it bends into the direction having the maximum equivalent plastic strain in the last part.

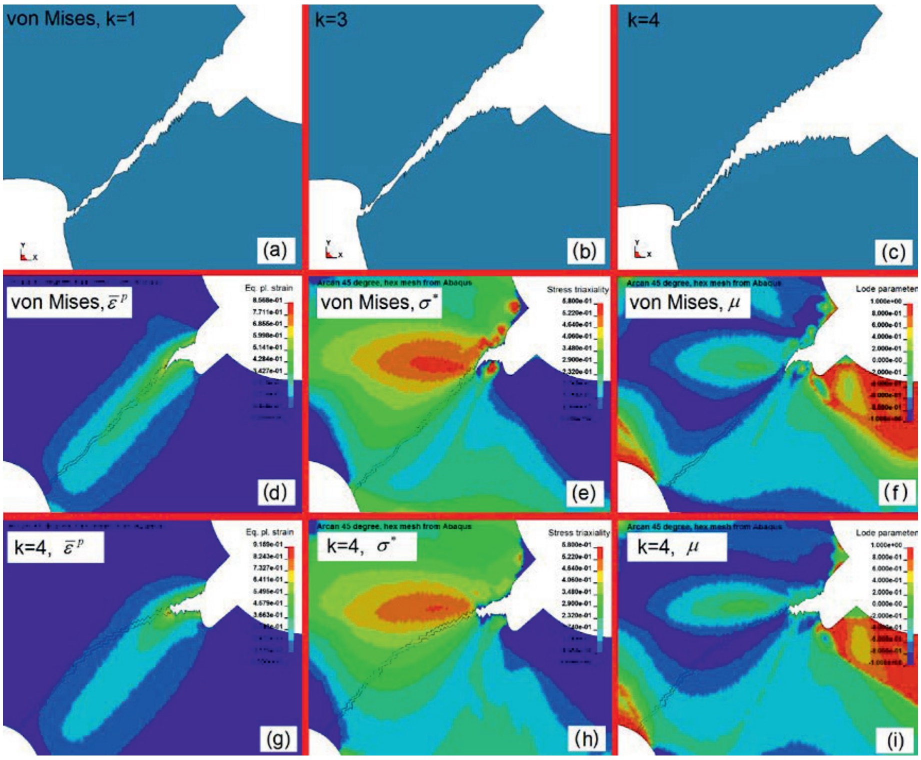

Fig. 14 Plots (a)−(c) display the effect of the yield function on the crack path in the Arcan-45 simulations. Plots (d)−(i) present contours of $\bar{\varepsilon}^p$, σ^* and μ in the early stages of fracture in the Arcan-45 simulations with: (d)−(f) J_2 flow theory and (g)−(i) Hershey yield function $(k = 4)$. The subsequent crack path is marked in plots (d)−(i).

5.3 Effect of mesh refinement and slant shear fracture

The slant shear fracture seen in most of the experiments was not captured in the finite element simulations in the previous sections. The reason for this is bipartite; firstly the spatial discretizations used in the models are too coarse to capture this phenomenon. Secondly the classical elastic-plastic solid with a smooth yield surface does not predict shear-band localization at realistic levels of straining unless the material displays a very low work hardening (Hutchinson and Tvergaard, 1981; Needleman and Tvergaard, 1992). However, by introducing a yield surface vertex, non-normality or material softening, the critical strain to capture shear band localization is considerably lowered (Hutchinson and Tvergaard, 1981).

In order to investigate the effect of mesh refinement and slant shear fracture in the numerical analysis, additional simulations were carried out on models with finer discretization, J_2 flow theory and the ECL fracture criterion with and without coupled damage. As pointed out by Needleman (1988), the size of the shear band in the simulation is restricted by the element size. The shear-band width was not measured for the Docol 600DL material under the quasi-static, isothermal loading, and the authors could not find data in the literature for a similar material deformed under similar loading. However, the final element size of the dense-mesh FE models $(\approx 80\ \mu\text{m})$ may be in the vicinity of the experimental shear-band width, based on the experience from the study conducted by Solberg et al. (2007). In that study it was found that the width of adiabatic shear bands in three different types of Weldox steels were in the vicinity of $10-100\ \mu\text{m}$, somewhat depending on the material. The $F-u$ curves and the crack surfaces from the dense-mesh simulations of the uniaxial tension, plane-strain tension and in-plane shear tests are given in Fig. 15. Here the $F-u$ curves are compared with results from coarse-mesh FE analyses utilizing the ECL criterion, J_2 plasticity and reduced integrated elements. In the FE simulations of the uniaxial tension and plane-strain tension tests, the strain softening gave a pronounced through-thickness slant fracture. However, the $F-u$ curves were nearly identical to the curves from the dense-mesh, uncoupled damage FE simulations where no slant fracture was predicted. This is in accordance with the findings of Li et al. (2011). The crack in the uniaxial tension simulation with coupled damage displayed an in-plane angle not unlike what is observed in the experiments, while the V-mode was not as pronounced as in the experimental tests. The simulation of the plane-strain tension test with coupled damage, on the other hand, displayed a more distinct slant fracture in the centre of the specimen than in the experiments. It is noted that the symmetry and anti-symmetry of the fracture surfaces observed in the uniaxial tension and plane-strain tension simulations disappear if e.g. material inhomogeneity is introduced. However, since the slant fracture surfaces in the experiments had a stochastic nature, an exact match between the experimental and simulated fracture surface cannot be expected. The mesh refinement led to a lower displacement at fracture initiation. This can be explained by the increased strain gradient in the dense-mesh FE models which advances the through-thickness localization. The effect of strain softening was more pronounced on the $F-u$ curves of the shear test simulation than in the simulations of the other two tests. This is because the shear tests do not exhibit necking instability before fracture. The displacement at fracture in the experimental shear tests is $u_f \approx 3.5\text{ mm}$, which is between the displacement at fracture predicted by the simulations with a denser mesh using coupled and uncoupled damage, respectively. The fracture surface in the shear simulations was not influenced by mesh refinement or damage softening as can be seen in Fig. 15, and is similar to the fracture surface observed in the experiments.

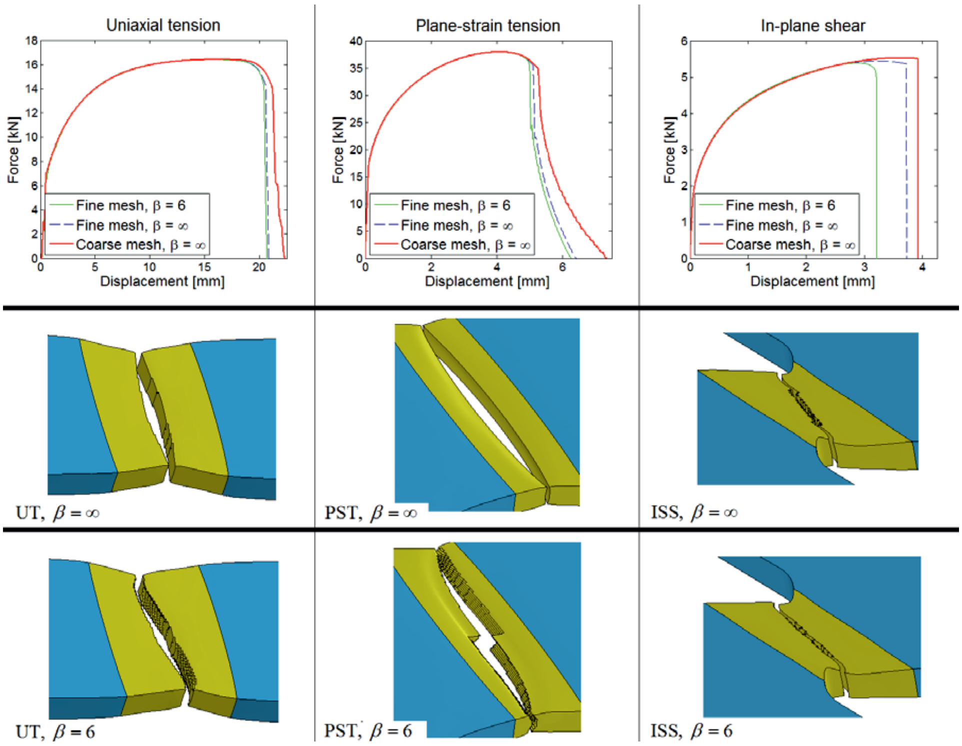

Fig. 15 Force-displacement curves in FE analyses with coarse and dense mesh without softening and dense mesh with softening. The crack surfaces are from simulations with dense mesh, with and without softening.

6 Discussion

The crack trajectories in the simulations of the material tests with coarse mesh, i.e. uniaxial tension, in-plane shear and plane-strain tension were similar, independent of fracture criterion and yield function. The same yields for the simulations of the Arcan-90 test. The crack paths in all these tests are controlled by the geometry of the specimens and the test set-ups, so only small variations in the predicted crack paths were observed. The crack paths in the simulations of the mixed-mode Arcan-45 test, however, differed to a certain degree when the fracture criterion and yield function were changed. The combination of J_2 flow theory and the MMC fracture criterion gave a crack path initially governed by the stress state before it abruptly changed to the direction of the largest equivalent plastic strain, leaving a bilinear crack trajectory. The simulation in which the Hershey yield function with $k = 4$ and the ECL criterion were used, gave a crack path that was a result of a competition between the stress and equivalent plastic strain fields in the specimen during the first part of the crack trajectory. This led to a curved shape on the crack path in this region that resembled the experimental results. In the last part, the crack path propagated in the direction of the largest equivalent plastic strain, and formed a linear trajectory. All the other simulations of the Arcan-45 test gave a nearly linear crack path in the direction of largest equivalent plastic strain. These results show that the Arcan-45 test is more challenging than the other tests for evaluating fracture criteria with respect to crack propagation.

In the simulations of the uniaxial tension, plane-strain tension and modified Arcan tests, the displacement increment from fracture initiation to global failure, Δu, was large compared to the experiments. In the simulations of the plane-strain tension test, it can be seen from Fig. 3 and Fig. 15 that the displacement increment from fracture initiation to global failure is $\Delta u \approx 1.5\ \text{mm}$ and $\Delta u \approx 2.1\ \text{mm}$ in the simulations with coarse mesh in combination with selectively reduced (Section 5.1) and reduced integration (Section 5.3), respectively. The dense-mesh simulations gave $\Delta u \approx 1.3\ \text{mm}$ for both uncoupled and coupled damage, while the experiments had $\Delta u \approx 0.5\ \text{mm}$. In the simulations of the uniaxial tension test, the same trend is observed in Fig. 3 and Fig. 15. Here the simulations with coarse mesh gave $\Delta u \approx 0.6\ \text{mm}$ and $\Delta u \approx 1.0\ \text{mm}$ for selective-reduced and reduced integration, respectively, $\Delta u \approx 0.3\ \text{mm}$ for the simulations with finer mesh, while $\Delta u < 0.02$ mm in the experiments. Since the damage is driven by plastic strain and the crack propagation is a sequence of fracture initiation in the eroded elements, the observations suggest that a large number of degrees of freedom should be used in the FE models to capture the crack propagation speed found experimentally. There was a significant effect when increasing the number of elements as well as when going from elements with selectively-reduced integration to reduced integration, whereas damage softening and prediction of slant fracture did not significantly influence the speed of the crack propagation in the simulations. The displacement at global failure, u_f, in the uniaxial tension, plane-strain tension and in-plane shear simulations was reduced when selective-reduced integration or a denser mesh was employed in the FE models, due to a more realistic prediction of the local necking process and crack propagation. It is noted that the prediction of slant fracture in the uniaxial tension and plane-strain tensions simulations had virtually no effect on the global force-displacement curves in Fig. 15. This suggests that the energy dissipated after the onset of shear-band localization in the FE simulations is very small compared to the energy dissipated in local necking, as also discussed by Nielsen and Hutchinson (2011). It is further noted that the uniaxial tension simulation with refined mesh and no softening given in Fig. 15, displays a tendency to slant fracture surface. Indeed, in a simulation where the ductility parameter W_C was increased to 1400 MPa, slant fracture was predicted, even though no damage softening was included. This increase in W_C did, however, lead to unrealistically large local deformations.

Tensile tests on Docol 600DL specimens with 0.7 mm thickness, but apart from this the same geometry as displayed in Fig. 1, were presented in Rakvåg et al. (2012). They showed that the material behaviour of the 0.7 mm and 2.0 mm thick Docol 600DL sheets was similar. The 0.7 mm thick uniaxial tensile specimens displayed no shear lips and fractured in the through-thickness neck as illustrated in Fig. 16(a) and (c). To see whether the FE models of the uniaxial tension test used in Section 5.3 could predict this behaviour, the models were scaled in the $\mathbf{e}_Z$ direction to obtain 0.7 mm thickness, and run in LS-DYNA. As can be seen from Fig. 16(b), through-thickness slant fracture was not predicted in the model with damage softening. Fig. 16(c) displays that the in-plane angle between the fracture surface and the $\mathbf{e}_X$ direction in the simulations with dense mesh is in excellent agreement with the experimental data, while the simulation with a coarse mesh does not capture this instability and the corresponding fracture mode. From this study it is evident that a rather fine mesh is required to capture local necking and the correct fracture mode for the thin-sheet specimens and that damage softening is not necessary to predict this fracture mode.

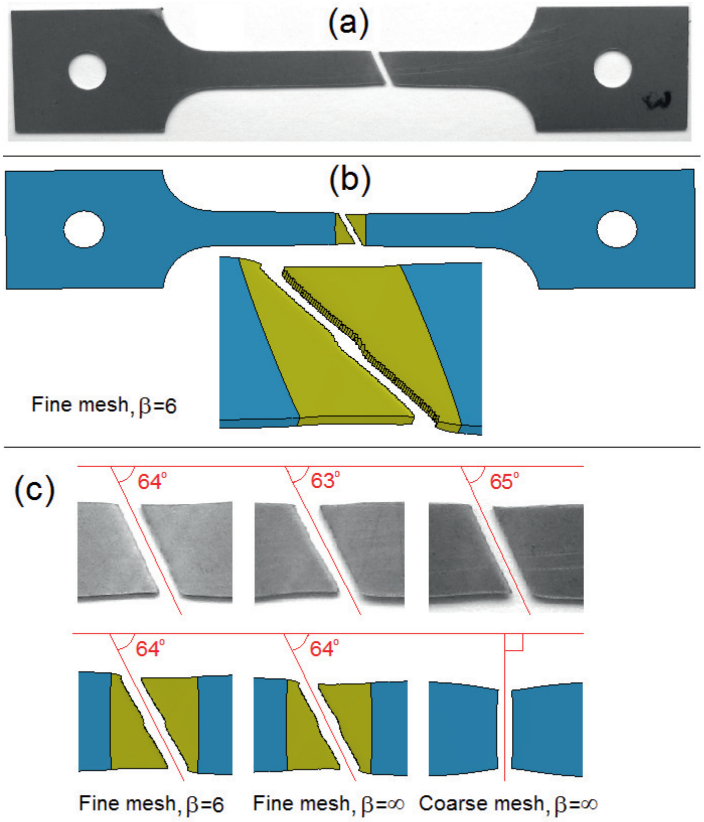

Fig. 16 Experiments and FE simulations of tensile tests on 0.7 mm thick specimens. (a) Failed specimen in experiment, (b) failed specimen and fracture surface in FE simulation with coupled damage. (c) In-plane angles of fracture surface in parallel tests Nos. 1, 2 and 3 and in FE simulations with different mesh density and coupled/uncoupled damage.

7 Conclusions

The modified Mohr-Coulomb and the extended Cockcroft-Latham fracture criteria have been used in explicit finite-element simulations of ductile crack propagation in a dual-phase steel sheet. The sheet was discretized with solid elements and the crack propagation was simulated by element erosion. The simulation results were compared to experiments conducted on five different types of specimens (uniaxial tension, plane-strain tension, shear, 45° and 90° modified Arcan) made from a 2 mm thick Docol 600DL steel sheet. The main conclusion is that the predicted force-displacement curves and crack paths were only to a small degree influenced by the fracture criterion, and it is hard to select one fracture criterion that out-performs the others. It was further found that only small changes in the predicted force-displacement curves and crack paths were obtained when changing from the von Mises to the Hershey yield criterion with a high exponent. However, an improvement of the in-plane crack path in the simulation of the mixed-mode 45° modified Arcan test was achieved by using the Hershey yield function. The use of selective-reduced integration rather than reduced integration for the eight-node, tri-linear solid elements, or use of a denser mesh in the FE models gave an improved resolution of the large strain gradients in the simulations. This led to predictions of the localized necking instability at a lower actuator displacement as well as higher crack propagation speed, both of which are in better accordance with the experiments. Slant fracture as observed in the experimental uniaxial tension and plane-strain tension tests was captured in the numerical simulations if material softening was accounted for and a sufficiently fine mesh was used. The prediction of slant fracture did, however, not have any significant effect on the global response as represented by the force-displacement curves.

Acknowledgement

The financial support of this work from the Structural Impact Laboratory (SIMLab), Centre for Research-based Innovation (CRI) at the Norwegian University of Science and Technology (NTNU), is gratefully acknowledged.

References

Anderson, T.L., 2005. Fracture Mechanics; Fundamentals and Applications, Third ed. Taylor & Francis Group, LLC, Boca Raton.

Areias, P.M., 2006. Analysis of Finite Strain Anisotropic Elastoplastic Fracture in Thin Plates and Shells. Journal of Aerospace Engineering 19, 259.

Avramovic-Cingara, G., Saleh, C.A.R., Jain, M.K., Wilkinson, D.S., 2009. Void Nucleation and Growth in Dual-Phase Steel 600 during Uniaxial Tensile Testing. Metallurgical and Materials Transactions A 40, 3117-3127.

Bai, Y., Wierzbicki, T., 2010. Application of extended Mohr–Coulomb criterion to ductile fracture. International Journal of Fracture 161, 1-20.

Bouchard, P.O., Bay, F., Chastel, Y., Tovena, I., 2000. Crack propagation modelling using an advanced remeshing technique. Computer Methods in Applied Mechanics and Engineering 189, 723-742.

Cockcroft, M.G., Latham, D.J., 1968. Ductility and the workability of metals. Journal of the Institute of Metals 96, 33-39.

Curtze, S., 2009. Deformation behavior of TRIP and DP steels in tension at different temperatures over a wide range of strain rates. Materials science & engineering. A, Structural materials 507, 124-131.

de Borst, R., 2004. Damage, Material Instabilities, and Failure. Encyclopedia of Computational Mechanics. Wiley.

Dørum, C., Hopperstad, O.S., Berstad, T., Dispinar, D., 2009. Numerical modelling of magnesium die-castings using stochastic fracture parameters. Engineering Fracture Mechanics 76, 2232-2248.

Fagerholt, E., 2012. Field measurements in mechanical testing using close-range photogrammetry and digital image analysis, 2012:95. PhD thesis, Norwegian University of Science and Technology.

Fagerholt, E., Dørum, C., Børvik, T., Laukli, H.I., Hopperstad, O.S., 2010. Experimental and numerical investigation of fracture in a cast aluminium alloy. International Journal of Solids and Structures 47, 3352-3365.

Fagerström, M., Larsson, R., 2006. Theory and numerics for finite deformation fracture modelling using strong discontinuities. International Journal for Numerical Methods in Engineering 66, 911-948.

Freudenthal, A.M., 1950. The Inelastic Behaviour of Solids. Wiley, New York.

Fyllingen, Ø., Hopperstad, O.S., Langseth, M., 2007. Stochastic simulations of square aluminium tubes subjected to axial loading. International Journal of Impact Engineering 34, 1619-1636.

Gruben, G., Fagerholt, E., Hopperstad, O.S., Børvik, T., 2011. Fracture characteristics of a cold-rolled dual-phase steel European Journal of Mechanics - A/Solids 30, 204-218.

Gruben, G., Hopperstad, O.S., Børvik, T., 2012a. Evaluation of uncoupled ductile fracture criteria for the dual-phase steel Docol 600DL. International Journal of Mechanical Sciences Accepted for publication.

Gruben, G., Vysochinskiy, D., Coudert, T., Reyes, A., Lademo, O.-G., 2012b. Determination of ductile fracture parameters of a dual-phase steel by optical measurements. submitted for possible publication.

Gurson, A.L., 1977. Continuum theory of ductile rupture by void nucleation and growth, 1. Yield criteria and flow rules for porous ductile media. Journal of Engineering Materials and Technology-Transactions of the ASME 99(1), 2-15.

Hershey, A.V., 1954. The Plasticity of an Isotropic Aggregate of Anisotropic Face-Centered Cubic Crystals. Journal Applied Mechanics 76, 241-249.

Hutchinson, J.W., 1964a. Plastic deformation of b.c.c. polycrystals. Journal of the Mechanics and Physics of Solids 12, 25-33.

Hutchinson, J.W., 1964b. Plastic stress-strain relations of F.C.C polycrystalline metals hardening according to Taylor's rule. Journal of the Mechanics and Physics of Solids 12, 11-24.

Hutchinson, J.W., Tvergaard, V., 1981. Shear band formation in plane strain. International Journal of Solids and Structures 17, 451-470.

Johnsen, T.K., 2009. Fracture of ductile materials: Experiments and simulation. Master thesis, Norwegian University of Science and Technology.

Johnson, G.R., Cook, W.H., 1985. Fracture characteristics of three metals subjected to various strains, strain rates, temperatures and pressures. Engineering Fracture Mechanics 21, 31-48.

Kane, A., Børvik, T., Berstad, T., Benallal, A., Hopperstad, O.S., 2011. Failure criteria with unilateral conditions for simulation of plate perforation. European Journal of Mechanics - A/Solids 30, 468-476.

Kazutake, K., 1999. Simulation of chevron crack formation and evolution in drawing. International Journal of Mechanical Sciences 41, 1499-1513.

Komori, K., 2005. Ductile fracture criteria for simulating shear by node separation method. Theoretical and Applied Fracture Mechanics 43, 101-114.

Lemaitre, J., 1992. A course on Damage Mechanics. Springer-Verlag.

Lemaitre, J., Chaboche, J.-L., 1990. Mechanics of solid materials. Cambridge University Press.

Li, Y., Wierzbicki, T., Sutton, M., Yan, J., Deng, X., 2011. Mixed mode stable tearing of thin sheet AI 6061-T6 specimens: experimental measurements and finite element simulations using a modified Mohr-Coulomb fracture criterion. International Journal of Fracture 168, 53-71.

Lode, W., 1926. Versuche fiber den Einfluß der mittleren Hauptspannung auf das Fließen der Metalle Eisen, Kupfer und Nickel. Zeitschrift für Physik A Hadrons and Nuclei 36, 913-939.

LSTC, 2007. LS-DYNA keyword user's manual, version 971. Livermore Software Technology Corporation.

MATLAB, 2009. version 7.9 (R2009b). The MathWorks Inc.

Mediavilla, J., Peerlings, R.H.J., Geers, M.G.D., 2006. A robust and consistent remeshing-transfer operator for ductile fracture simulations. Computers and Structures 84, 604-623.

Needleman, A., 1988. Material rate dependence and mesh sensitivity in localization problems. Computer Methods in Applied Mechanics and Engineering 67, 69-85.

Needleman, A., 1990. An analysis of decohesion along an imperfect interface. International Journal of Fracture 42, 21-40.

Needleman, A., Tvergaard, V., 1992. Analyses of Plastic Flow Localization in Metals. Applied Mechanics Reviews 45, S3-S18.

Nielsen, K.L., Hutchinson, J.W., 2011. Cohesive traction–separation laws for tearing of ductile metal plates. International Journal of Impact Engineering In press.

Rakvåg, K.G., Underwood, N., Schleyerb, G.K., Børvik, T., Hopperstad, O.S., 2012. Transient pressure loading of plates with pre-formed holes. International Journal of Impact Engineering Submitted for possible publication.

Rousselier, G., 1987. Ductile fracture models and their potential in local approach of fracture. Nuclear Engineering and Design 105, 97-111.

Shima, S., Oyane, M., 1976. Plasticity theory for porous metals. International Journal of Mechanical Sciences 18, 285-291.

Solberg, J.K., Leinum, J.R., Embury, J.D., Dey, S., Børvik, T., Hopperstad, O.S., 2007. Localised shear banding in Weldox steel plates impacted by projectiles. Mechanics of Materials 39, 865-880.

SSAB, 2009. Docol DP/DL Cold reduced dual phase steels. http://www.ssab.com/Global/DOCOL/datasheets_docol/en/201_Docol%20DP%20DL.pdf (Accessed: 27.04.2012)

Tarigopula, V., Langseth, M., Hopperstad, O.S., Clausen, A.H., 2006. Axial crushing of thin-walled high-strength steel sections. International Journal of Impact Engineering 32, 847-882.

Tvergaard, V., 2001. Crack growth predictions by cohesive zone model for ductile fracture. Journal of the Mechanics and Physics of Solids 49, 2191-2207.

Tvergaard, V., Hutchinson, J.W., 1996. Effect of strain-dependent cohesive zone model on predictions of crack growth resistance. International Journal of Solids and Structures 33, 3297-3308.

Wilkins, M.L., Streit, R.D., Reaugh, J.E., 1980. Cumulative-strain-damage model of ductile fracture: simulation and prediction of engineering fracture tests, Technical Report UCRL-53058. Lawrence Livermore National Laboratory.

Xue, L., Wierzbicki, T., 2008. Ductile fracture initiation and propagation modeling using damage plasticity theory. Engineering Fracture Mechanics 75, 3276-3293.

"Reliability Analysis of Structural Systems using Nonlinear Finite Element Methods",
C. A. Holm, 1990:23, ISBN 82-7119-178-0.

"Uniform Stratified Flow Interaction with a Submerged Horizontal Cylinder",
Ø. Arntsen, 1990:32, ISBN 82-7119-188-8.

"Large Displacement Analysis of Flexible and Rigid Systems Considering
Displacement-Dependent Loads and Nonlinear Constraints",
K. M. Mathisen, 1990:33, ISBN 82-7119-189-6.

"Solid Mechanics and Material Models including Large Deformations",
E. Levold, 1990:56, ISBN 82-7119-214-0, ISSN 0802-3271.

"Inelastic Deformation Capacity of Flexurally-Loaded Aluminium Alloy Structures",
T. Welo, 1990:62, ISBN 82-7119-220-5, ISSN 0802-3271.

"Visualization of Results from Mechanical Engineering Analysis",
K. Aamnes, 1990:63, ISBN 82-7119-221-3, ISSN 0802-3271.

"Object-Oriented Product Modeling for Structural Design",
S. I. Dale, 1991:6, ISBN 82-7119-258-2, ISSN 0802-3271.

"Parallel Techniques for Solving Finite Element Problems on Transputer Networks",
T. H. Hansen, 1991:19, ISBN 82-7119-273-6, ISSN 0802-3271.

"Statistical Description and Estimation of Ocean Drift Ice Environments",
R. Korsnes, 1991:24, ISBN 82-7119-278-7, ISSN 0802-3271.

“Properties of concrete related to fatigue damage: with emphasis on high strength concrete”,
G. Petkovic, 1991:35, ISBN 82-7119-290-6, ISSN 0802-3271.

"Turbidity Current Modelling",
B. Brørs, 1991:38, ISBN 82-7119-293-0, ISSN 0802-3271.

"Zero-Slump Concrete: Rheology, Degree of Compaction and Strength. Effects of Fillers as Part Cement-Replacement",
C. Sørensen, 1992:8, ISBN 82-7119-357-0, ISSN 0802-3271.

"Nonlinear Analysis of Reinforced Concrete Structures Exposed to Transient Loading",
K. V. Høiseth, 1992:15, ISBN 82-7119-364-3, ISSN 0802-3271.

"Finite Element Formulations and Solution Algorithms for Buckling and Collapse Analysis of Thin Shells",
R. O. Bjærum, 1992:30, ISBN 82-7119-380-5, ISSN 0802-3271.

"Response Statistics of Nonlinear Dynamic Systems",
J. M. Johnsen, 1992:42, ISBN 82-7119-393-7, ISSN 0802-3271.

"Digital Models in Engineering. A Study on why and how engineers build and operate digital models for decisison support",
J. Høyte, 1992:75, ISBN 82-7119-429-1, ISSN 0802-3271.

"Sparse Solution of Finite Element Equations",
A. C. Damhaug, 1992:76, ISBN 82-7119-430-5, ISSN 0802-3271.

"Some Aspects of Floating Ice Related to Sea Surface Operations in the Barents Sea",
S. Løset, 1992:95, ISBN 82-7119-452-6, ISSN 0802-3271.

"Modelling of Cyclic Plasticity with Application to Steel and Aluminium Structures",
O. S. Hopperstad, 1993:7, ISBN 82-7119-461-5, ISSN 0802-3271.

"The Free Formulation: Linear Theory and Extensions with Applications to Tetrahedral Elements
with Rotational Freedoms",
G. Skeie, 1993:17, ISBN 82-7119-472-0, ISSN 0802-3271.

"Høyfast betongs motstand mot piggdekkslitasje. Analyse av resultater fra prøving i Veisliter'n",
T. Tveter, 1993:62, ISBN 82-7119-522-0, ISSN 0802-3271.

"A Nonlinear Finite Element Based on Free Formulation Theory for Analysis of Sandwich Structures",
O. Aamlid, 1993:72, ISBN 82-7119-534-4, ISSN 0802-3271.

"The Effect of Curing Temperature and Silica Fume on Chloride Migration and Pore Structure of High Strength Concrete",
C. J. Hauck, 1993:90, ISBN 82-7119-553-0, ISSN 0802-3271.

"Failure of Concrete under Compressive Strain Gradients",
G. Markeset, 1993:110, ISBN 82-7119-575-1, ISSN 0802-3271.

"An experimental study of internal tidal amphidromes in Vestfjorden",
J. H. Nilsen, 1994:39, ISBN 82-7119-640-5, ISSN 0802-3271.

"Structural analysis of oil wells with emphasis on conductor design",
H. Larsen, 1994:46, ISBN 82-7119-648-0, ISSN 0802-3271.

"Adaptive methods for non-linear finite element analysis of shell structures",
K. M. Okstad, 1994:66, ISBN 82-7119-670-7, ISSN 0802-3271.

"On constitutive modelling in nonlinear analysis of concrete structures",
O. Fyrileiv, 1994:115, ISBN 82-7119-725-8, ISSN 0802-3271.

"Fluctuating wind load and response of a line-like engineering structure with emphasis on motion-induced wind forces",
J. Bogunovic Jakobsen, 1995:62, ISBN 82-7119-809-2, ISSN 0802-3271.

"An experimental study of beam-columns subjected to combined torsion, bending and axial actions",
A. Aalberg, 1995:66, ISBN 82-7119-813-0, ISSN 0802-3271.

"Scaling and cracking in unsealed freeze/thaw testing of Portland cement and silica fume concretes",
S. Jacobsen, 1995:101, ISBN 82-7119-851-3, ISSN 0802-3271.

"Damping of water waves by submerged vegetation. A case study of laminaria hyperborea",
A. M. Dubi, 1995:108, ISBN 82-7119-859-9, ISSN 0802-3271.

"The dynamics of a slope current in the Barents Sea",
Sheng Li, 1995:109, ISBN 82-7119-860-2, ISSN 0802-3271.

"Modellering av delmaterialenes betydning for betongens konsistens",
Ernst Mørtsell, 1996:12, ISBN 82-7119-894-7, ISSN 0802-3271.

"Bending of thin-walled aluminium extrusions",
Birgit Søvik Opheim, 1996:60, ISBN 82-7119-947-1, ISSN 0802-3271.

"Material modelling of aluminium for crashworthiness analysis",
Torodd Berstad, 1996:89, ISBN 82-7119-980-3, ISSN 0802-3271.

"Estimation of structural parameters from response measurements on submerged floating tunnels",
Rolf Magne Larssen, 1996:119, ISBN 82-471-0014-2, ISSN 0802-3271.

“Numerical modelling of plain and reinforced concrete by damage mechanics”,
Mario A. Polanco-Loria, 1997:20, ISBN 82-471-0049-5, ISSN 0802-3271.

“Nonlinear random vibrations - numerical analysis by path integration methods”,
Vibeke Moe, 1997:26, ISBN 82-471-0056-8, ISSN 0802-3271.

“Numerical prediction of vortex-induced vibration by the finite element method”,
Joar Martin Dalheim, 1997:63, ISBN 82-471-0096-7, ISSN 0802-3271.

“Time domain calculations of buffeting response for wind sensitive structures”,
Ketil Aas-Jakobsen, 1997:148, ISBN 82-471-0189-0, ISSN 0802-3271.

"A numerical study of flow about fixed and flexibly mounted circular cylinders",
Trond Stokka Meling, 1998:48, ISBN 82-471-0244-7, ISSN 0802-3271.

“Estimation of chloride penetration into concrete bridges in coastal areas”,
Per Egil Steen, 1998:89, ISBN 82-471-0290-0, ISSN 0802-3271.

“Stress-resultant material models for reinforced concrete plates and shells”,
Jan Arve Øverli, 1998:95, ISBN 82-471-0297-8, ISSN 0802-3271.

“Chloride binding in concrete. Effect of surrounding environment and concrete composition”,
Claus Kenneth Larsen, 1998:101, ISBN 82-471-0337-0, ISSN 0802-3271.

“Rotational capacity of aluminium alloy beams”,
Lars A. Moen, 1999:1, ISBN 82-471-0365-6, ISSN 0802-3271.

“Stretch Bending of Aluminium Extrusions”,
Arild H. Clausen, 1999:29, ISBN 82-471-0396-6, ISSN 0802-3271.

“Aluminium and Steel Beams under Concentrated Loading”,
Tore Tryland, 1999:30, ISBN 82-471-0397-4, ISSN 0802-3271.

"Engineering Models of Elastoplasticity and Fracture for Aluminium Alloys",
Odd-Geir Lademo, 1999:39, ISBN 82-471-0406-7, ISSN 0802-3271.

"Kapasitet og duktilitet av dybelforbindelser i trekonstruksjoner",
Jan Siem, 1999:46, ISBN 82-471-0414-8, ISSN 0802-3271.

“Etablering av distribuert ingeniørarbeid; Teknologiske og organisatoriske erfaringer fra en norsk ingeniørbedrift”,
Lars Line, 1999:52, ISBN 82-471-0420-2, ISSN 0802-3271.

“Estimation of Earthquake-Induced Response”,
Símon Ólafsson, 1999:73, ISBN 82-471-0443-1, ISSN 0802-3271.

“Coastal Concrete Bridges: Moisture State, Chloride Permeability and Aging Effects”
Ragnhild Holen Relling, 1999:74, ISBN 82-471-0445-8, ISSN 0802-3271.

”Capacity Assessment of Titanium Pipes Subjected to Bending and External Pressure”,
Arve Bjørset, 1999:100, ISBN 82-471-0473-3, ISSN 0802-3271.

“Validation of Numerical Collapse Behaviour of Thin-Walled Corrugated Panels”,
Håvar Ilstad, 1999:101, ISBN 82-471-0474-1, ISSN 0802-3271.

“Strength and Ductility of Welded Structures in Aluminium Alloys”,
Miroslaw Matusiak, 1999:113, ISBN 82-471-0487-3, ISSN 0802-3271.

“Thermal Dilation and Autogenous Deformation as Driving Forces to Self-Induced Stresses in High Performance Concrete”,
Øyvind Bjøntegaard, 1999:121, ISBN 82-7984-002-8, ISSN 0802-3271.

“Some Aspects of Ski Base Sliding Friction and Ski Base Structure”,
Dag Anders Moldestad, 1999:137, ISBN 82-7984-019-2, ISSN 0802-3271.

"Electrode reactions and corrosion resistance for steel in mortar and concrete",
Roy Antonsen, 2000:10, ISBN 82-7984-030-3, ISSN 0802-3271.

"Hydro-Physical Conditions in Kelp Forests and the Effect on Wave Damping and Dune Erosion. A case study on Laminaria Hyperborea",
Stig Magnar Løvås, 2000:28, ISBN 82-7984-050-8, ISSN 0802-3271.

"Random Vibration and the Path Integral Method",
Christian Skaug, 2000:39, ISBN 82-7984-061-3, ISSN 0802-3271.

"Buckling and geometrical nonlinear beam-type analyses of timber structures",
Trond Even Eggen, 2000:56, ISBN 82-7984-081-8, ISSN 0802-3271.

”Structural Crashworthiness of Aluminium Foam-Based Components”,
Arve Grønsund Hanssen, 2000:76, ISBN 82-7984-102-4, ISSN 0809-103X.

“Measurements and simulations of the consolidation in first-year sea ice ridges, and some aspects of mechanical behaviour”,
Knut V. Høyland, 2000:94, ISBN 82-7984-121-0, ISSN 0809-103X.

”Kinematics in Regular and Irregular Waves based on a Lagrangian Formulation”,
Svein Helge Gjøsund, 2000-86, ISBN 82-7984-112-1, ISSN 0809-103X.

”Self-Induced Cracking Problems in Hardening Concrete Structures”,
Daniela Bosnjak, 2000-121, ISBN 82-7984-151-2, ISSN 0809-103X.

"Ballistic Penetration and Perforation of Steel Plates",
Tore Børvik, 2000:124, ISBN 82-7984-154-7, ISSN 0809-103X.

"Freeze-Thaw resistance of Concrete. Effect of: Curing Conditions, Moisture Exchange and Materials",
Terje Finnerup Rønning, 2001:14, ISBN 82-7984-165-2, ISSN 0809-103X

"Structural behaviour of post tensioned concrete structures. Flat slab. Slabs on ground",
Steinar Trygstad, 2001:52, ISBN 82-471-5314-9, ISSN 0809-103X.

"Slipforming of Vertical Concrete Structures. Friction between concrete and slipform panel",
Kjell Tore Fosså, 2001:61, ISBN 82-471-5325-4, ISSN 0809-103X.

"Some numerical methods for the simulation of laminar and turbulent incompressible flows",
Jens Holmen, 2002:6, ISBN 82-471-5396-3, ISSN 0809-103X.

“Improved Fatigue Performance of Threaded Drillstring Connections by Cold Rolling”,
Steinar Kristoffersen, 2002:11, ISBN: 82-421-5402-1, ISSN 0809-103X.

"Deformations in Concrete Cantilever Bridges: Observations and Theoretical Modelling",
Peter F. Takâcs, 2002:23, ISBN 82-471-5415-3, ISSN 0809-103X.

"Stiffened aluminium plates subjected to impact loading",
Hilde Giæver Hildrum, 2002:69, ISBN 82-471-5467-6, ISSN 0809-103X.

"Full- and model scale study of wind effects on a medium-rise building in a built up area",
Jónas Thór Snæbjørnsson, 2002:95, ISBN82-471-5495-1, ISSN 0809-103X.

“Evaluation of Concepts for Loading of Hydrocarbons in Ice-infested water”,
Arnor Jensen, 2002:114, ISBN 82-417-5506-0, ISSN 0809-103X.

”Numerical and Physical Modelling of Oil Spreading in Broken Ice”,
Janne K. Økland Gjøsteen, 2002:130, ISBN 82-471-5523-0, ISSN 0809-103X.

”Diagnosis and protection of corroding steel in concrete”,
Franz Pruckner, 20002:140, ISBN 82-471-5555-4, ISSN 0809-103X.

“Tensile and Compressive Creep of Young Concrete: Testing and Modelling”,
Dawood Atrushi, 2003:17, ISBN 82-471-5565-6, ISSN 0809-103X.

“Rheology of Particle Suspensions. Fresh Concrete, Mortar and Cement Paste with Various Types of Lignosulfonates”,
Jon Elvar Wallevik, 2003:18, ISBN 82-471-5566-4, ISSN 0809-103X.

“Oblique Loading of Aluminium Crash Components”,
Aase Reyes, 2003:15, ISBN 82-471-5562-1, ISSN 0809-103X.

“Utilization of Ethiopian Natural Pozzolans”,
Surafel Ketema Desta, 2003:26, ISSN 82-471-5574-5, ISSN:0809-103X.

“Behaviour and strength prediction of reinforced concrete structures with discontinuity regions”, Helge Brå, 2004:11, ISBN 82-471-6222-9, ISSN 1503-8181.

“High-strength steel plates subjected to projectile impact. An experimental and numerical study”, Sumita Dey, 2004:38, ISBN 82-471-6282-2 (printed version), ISBN 82-471-6281-4 (electronic version), ISSN 1503-8181.

“Alkali-reactive and inert fillers in concrete. Rheology of fresh mixtures and expansive reactions.”
Bård M. Pedersen, 2004:92, ISBN 82-471-6401-9 (printed version), ISBN 82-471-6400-0 (electronic version), ISSN 1503-8181.

“On the Shear Capacity of Steel Girders with Large Web Openings”.
Nils Christian Hagen, 2005:9 ISBN 82-471-6878-2 (printed version), ISBN 82-471-6877-4 (electronic version), ISSN 1503-8181.

”Behaviour of aluminium extrusions subjected to axial loading”.
Østen Jensen, 2005:7, ISBN 82-471-6873-1 (printed version), ISBN 82-471-6872-3 (electronic version), ISSN 1503-8181.

”Thermal Aspects of corrosion of Steel in Concrete”.
Jan-Magnus Østvik, 2005:5, ISBN 82-471-6869-3 (printed version), ISBN 82-471-6868 (electronic version), ISSN 1503-8181.

”Mechanical and adaptive behaviour of bone in relation to hip replacement.” A study of bone remodelling and bone grafting.
Sébastien Muller, 2005:34, ISBN 82-471-6933-9 (printed version), ISBN 82-471-6932-0 (electronic version), ISSN 1503-8181.

“Analysis of geometrical nonlinearities with applications to timber structures”.
Lars Wollebæk, 2005:74, ISBN 82-471-7050-5 (printed version), ISBN 82-471-7019-1 (electronic version), ISSN 1503-8181.

“Pedestrian induced lateral vibrations of slender footbridges”,
Anders Rönnquist, 2005:102, ISBN 82-471-7082-5 (printed version), ISBN 82-471-7081-7 (electronic version), ISSN 1503-8181.

“Initial Strength Development of Fly Ash and Limestone Blended Cements at Various Temperatures Predicted by Ultrasonic Pulse Velocity”,
Tom Ivar Fredvik, 2005:112, ISBN 82-471-7105-8 (printed version), ISBN 82-471-7103-1 (electronic version), ISSN 1503-8181.

“Behaviour and modelling of thin-walled cast components”,
Cato Dørum, 2005:128, ISBN 82-471-7140-6 (printed version), ISBN 82-471-7139-2 (electronic version), ISSN 1503-8181.

“Behaviour and modelling of selfpiercing riveted connections”,
Raffaele Porcaro, 2005:165, ISBN 82-471-7219-4 (printed version), ISBN 82-471-7218-6 (electronic version), ISSN 1503-8181.

”Behaviour and Modelling og Aluminium Plates subjected to Compressive Load”,
Lars Rønning, 2005:154, ISBN 82-471-7169-1 (printed version), ISBN 82-471-7195-3 (electronic version), ISSN 1503-8181.

”Bumper beam-longitudinal system subjected to offset impact loading”,
Satyanarayana Kokkula, 2005:193, ISBN 82-471-7280-1 (printed version), ISBN 82-471-7279-8 (electronic version), ISSN 1503-8181.

“Control of Chloride Penetration into Concrete Structures at Early Age”,
Guofei Liu, 2006:46, ISBN 82-471-7838-9 (printed version), ISBN 82-471-7837-0 (electronic version), ISSN 1503-8181.

“Modelling of Welded Thin-Walled Aluminium Structures”,
Ting Wang, 2006:78, ISBN 82-471-7907-5 (printed version), ISBN 82-471-7906-7 (electronic version), ISSN 1503-8181.

”Time-variant reliability of dynamic systems by importance sampling and probabilistic analysis of ice loads”,
Anna Ivanova Olsen, 2006:139, ISBN 82-471-8041-3 (printed version), ISBN 82-471-8040-5 (electronic version), ISSN 1503-8181.

“Fatigue life prediction of an aluminium alloy automotive component using finite element analysis of surface topography”.
Sigmund Kyrre Ås, 2006:25, ISBN 82-471-7791-9 (printed version), ISBN 82-471-7791-9 (electronic version), ISSN 1503-8181.

”Constitutive models of elastoplasticity and fracture for aluminium alloys under strain path change”,
Dasharatha Achani, 2006:76, ISBN 82-471-7903-2 (printed version), ISBN 82-471-7902-4 (electronic version), ISSN 1503-8181.

“Simulations of 2D dynamic brittle fracture by the Element-free Galerkin method and linear fracture mechanics”,
Tommy Karlsson, 2006:125, ISBN 82-471-8011-1 (printed version), ISBN 82-471-8010-3 (electronic version), ISSN 1503-8181.

“Penetration and Perforation of Granite Targets by Hard Projectiles”,
Chong Chiang Seah, 2006:188, ISBN 82-471-8150-9 (printed version), ISBN 82-471-8149-5 (electronic version), ISSN 1503-8181.

“Deformations, strain capacity and cracking of concrete in plastic and early hardening phases”,
Tor Arne Hammer, 2007:234, ISBN 978-82-471-5191-4 (printed version), ISBN 978-82-471-5207-2 (electronic version), ISSN 1503-8181.

“Crashworthiness of dual-phase high-strength steel: Material and Component behaviour”, Venkatapathi Tarigopula, 2007:230, ISBN 82-471-5076-4 (printed version), ISBN 82-471-5093-1 (electronic version), ISSN 1503-8181.

“Fibre reinforcement in load carrying concrete structures”,
Åse Lyslo Døssland, 2008:50, ISBN 978-82-471-6910-0 (printed version), ISBN 978-82-471-6924-7 (electronic version), ISSN 1503-8181.

“Low-velocity penetration of aluminium plates”,
Frode Grytten, 2008:46, ISBN 978-82-471-6826-4 (printed version), ISBN 978-82-471-6843-1 (electronic version), ISSN 1503-8181.

“Robustness studies of structures subjected to large deformations”,
Ørjan Fyllingen, 2008:24, ISBN 978-82-471-6339-9 (printed version), ISBN 978-82-471-6342-9 (electronic version), ISSN 1503-8181.

“Constitutive modelling of morsellised bone”,
Knut Birger Lunde, 2008:92, ISBN 978-82-471-7829-4 (printed version), ISBN 978-82-471-7832-4 (electronic version), ISSN 1503-8181.

“Experimental Investigations of Wind Loading on a Suspension Bridge Girder”,
Bjørn Isaksen, 2008:131, ISBN 978-82-471-8656-5 (printed version), ISBN 978-82-471-8673-2 (electronic version), ISSN 1503-8181.

“Cracking Risk of Concrete Structures in The Hardening Phase”,
Guomin Ji, 2008:198, ISBN 978-82-471-1079-9 (printed version), ISBN 978-82-471-1080-5 (electronic version), ISSN 1503-8181.

“Modelling and numerical analysis of the porcine and human mitral apparatus”,
Victorien Emile Prot, 2008:249, ISBN 978-82-471-1192-5 (printed version), ISBN 978-82-471-1193-2 (electronic version), ISSN 1503-8181.

“Strength analysis of net structures”,
Heidi Moe, 2009:48, ISBN 978-82-471-1468-1 (printed version), ISBN 978-82-471-1469-8 (electronic version), ISSN1503-8181.

“Numerical analysis of ductile fracture in surface cracked shells”,
Espen Berg, 2009:80, ISBN 978-82-471-1537-4 (printed version), ISBN 978-82-471-1538-1 (electronic version), ISSN 1503-8181.

“Subject specific finite element analysis of bone – for evaluation of the healing of a leg lengthening and evaluation of femoral stem design”,
Sune Hansborg Pettersen, 2009:99, ISBN 978-82-471-1579-4 (printed version), ISBN 978-82-471-1580-0 (electronic version), ISSN 1503-8181.

“Evaluation of fracture parameters for notched multi-layered structures”,
Lingyun Shang, 2009:137, ISBN 978-82-471-1662-3 (printed version), ISBN 978-82-471-1663-0 (electronic version), ISSN 1503-8181.

“Modelling of Dynamic Material Behaviour and Fracture of Aluminium Alloys for Structural Applications”
Yan Chen, 2009:69, ISBN 978-82-471-1515-2 (printed version), ISBN 978-82 471-1516-9 (electronic version), ISSN 1503-8181.

“Nanomechanics of polymer and composite particles”
Jianying He 2009:213, ISBN 978-82-471-1828-3 (printed version), ISBN 978-82-471-1829-0 (electronic version), ISSN 1503-8181.

“Mechanical properties of clear wood from Norway spruce”
Kristian Berbom Dahl 2009:250, ISBN 978-82-471-1911-2 (printed version) ISBN 978-82-471-1912-9 (electronic version), ISSN 1503-8181.

“Modeling of the degradation of TiB_2 mechanical properties by residual stresses and liquid Al penetration along grain boundaries”
Micol Pezzotta 2009:254, ISBN 978-82-471-1923-5 (printed version) ISBN 978-82-471-1924-2 (electronic version) ISSN 1503-8181.

“Effect of welding residual stress on fracture”
Xiabo Ren 2010:77, ISBN 978-82-471-2115-3 (printed version) ISBN 978-82-471-2116-0 (electronic version), ISSN 1503-8181.

“Pan-based carbon fiber as anode material in cathodic protection system for concrete structures”
Mahdi Chini 2010:122, ISBN 978-82-471-2210-5 (printed version) ISBN 978-82-471-2213-6 (electronic version), ISSN 1503-8181.

“Structural Behaviour of deteriorated and retrofitted concrete structures”
Irina Vasililjeva Sæther 2010:171, ISBN 978-82-471-2315-7 (printed version) ISBN 978-82-471-2316-4 (electronic version) ISSN 1503-8181.

“Prediction of local snow loads on roofs”
Vivian Meløysund 2010:247, ISBN 978-82-471-2490-1 (printed version) ISBN 978-82-471-2491-8 (electronic version) ISSN 1503-8181.

“Behaviour and modelling of polymers for crash applications”
Virgile Delhaye 2010:251, ISBN 978-82-471-2501-4 (printed version) ISBN 978-82-471-2502-1 (electronic version) ISSN 1503-8181.

“Blended cement with reducted CO_2 emission – Utilizing the Fly Ash-Limestone Synergy”,
Klaartje De Weerdt 2011:32, ISBN 978-82-471-2584-7 (printed version) ISBN 978-82-471-2584-4 (electronic version) ISSN 1503-8181.

“Chloride induced reinforcement corrosion in concrete” Concept of critical chloride content – methods and mechanisms.
Ueli Angst 2011:113, ISBN 978-82-471-2769-9 (printed version) ISBN 978-82-471-2763-6 (electronic version) ISSN 1503-8181.

“A thermo-electric-Mechanical study of the carbon anode and contact interface for Energy savings in the production of aluminium”.
Dag Herman Andersen 2011:157, ISBN 978-82-471-2859-6 (printed version) ISBN 978-82-471-2860-2 (electronic version) ISSN 1503-8181.

“Structural Capacity of Anchorage Ties in Masonry Veneer Walls Subjected to Earthquake”. The implications of Eurocode 8 and Eurocode 6 on a typical Norwegain veneer wall.
Ahmed Mohamed Yousry Hamed 2011:181, ISBN 978-82-471-2911-1 (printed version) ISBN 978-82-471-2912-8 (electronic ver.) ISSN 1503-8181.

“Work-hardening behaviour in age-hardenable Al-Zn-Mg(-Cu) alloys”.
Ida Westermann , 2011:247, ISBN 978-82-471-3056-8 (printed ver.) ISBN 978-82-471-3057-5 (electronic ver.) ISSN 1503-8181.

“Behaviour and modelling of selfpiercing riveted connections using aluminium rivets”.
Nguyen-Hieu Hoang, 2011:266, ISBN 978-82-471-3097-1 (printed ver.) ISBN 978-82-471-3099-5 (electronic ver.) ISSN 1503-8181.

“Fibre reinforced concrete”.
Sindre Sandbakk, 2011:297, ISBN 978-82-471-3167-1 (printed ver.) ISBN 978-82-471-3168-8 (electronic ver) ISSN 1503:8181.

“Dynamic behaviour of cablesupported bridges subjected to strong natural wind”.
Ole Andre Øiseth, 2011:315, ISBN 978-82-471-3209-8 (printed ver.) ISBN 978-82-471-3210-4 (electronic ver.) ISSN 1503-8181.

“Constitutive modeling of solargrade silicon materials”
Julien Cochard, 2011:307, ISBN 978-82-471-3189-3 (printed ver). ISBN 978-82-471-3190-9 (electronic ver.) ISSN 1503-8181.

“Constitutive behavior and fracture of shape memory alloys”
Jim Stian Olsen, 2012:57, ISBN 978-82-471-3382-8 (printed ver.) ISBN 978-82-471-3383-5 (electronic ver.) ISSN 1503-8181.

“Field measurements in mechanical testing using close-range photogrammetry and digital image analysis”
Egil Fagerholt, 2012:95, ISBN 978-82-471-3466-5 (printed ver.) ISBN 978-82-471-3467-2 (electronic ver.) ISSN 1503-8181.

“Towards a better under standing of the ultimate behaviour of lightweight aggregate concrete in compression and bending”,
Håvard Nedrelid, 2012:123, ISBN 978-82-471-3527-3 (printed ver.) ISBN 978-82-471-3528-0 (electronic ver.) ISSN 1503-8181.

“Numerical simulations of blood flow in the left side of the heart”
Sigrid Kaarstad Dahl, 2012:135, ISBN 978-82-471-3553-2 (printed ver.) ISBN 978-82-471-3555-6 (electronic ver.) ISSN 1503-8181.

“Biomechanical aspects of distraction osteogensis”
Valentina La Russa, 2012:250, ISBN 978-82-471-3807-6 (printed ver.) ISBN 978-82-471-3808-3 (electronic ver.) ISSN 1503-8181.